UNIVERSITÀ DEGLI STUDI DI UDINE

DIPARTIMENTO POLITECNICO DI INGEGNERIA E ARCHITETTURA

PH.D. PROGRAM, XXIX CYCLE

ENVIRONMENTAL AND ENERGY ENGINEERING SCIENCE

# An experimental investigation on the aerodynamic behavior of cooling channels for the leading edge of gas turbine blades

*Supervisor:*
Prof. Luca CASARSA

*Author:*
Dott. Ing. Luca FURLANI

ACADEMIC YEAR - 2017

**Abstract**

The purpose of this dissertation is to provide a strong background knowledge about the flow field behavior inside leading edge internal cooling systems while addressing the importance of aerodynamic data for cooling channels design.
This research is mainly focused on the characterization of rotation effects inside a triangular channel since, in the open literature, the only channel geometry exhaustively studied had been the rectangular one. In fact, in recent years, the interest of the scientific community had been shifted to the direct analysis of the thermal field, which is indeed the final figure of evaluation of the cooling system. However, the thermal field characterization alone (i.e. Nusselt number distribution), is not able to provide enough information in order to allow a complete and deep understanding of the heat transfer problem because it describes an effect giving too little clues about its cause, which is the aerodynamic field indeed. Even in simple geometries, the aerodynamic behavior usually is too much complex to be inferred just exploiting the thermal data. This is a major problem if an optimization process of the cooling system is considered: with the thermal data only a trial-and-error kind of iteration is possible. On the contrary, the knowledge of the flow field allow to operate in a more thoughtful way.
For the reasons explained above, the first part of the research has been dedicated to the complete aerodynamic characterization of the simplest geometry suitable to represent a leading edge cooling system: a straight channel with triangular equilateral cross section, without bleeding holes, and with squared turbulence promoters perpendicular to the bulk velocity and placed on both leading and trailing sides. This campaign is the following of a previous work, where a smooth channel had been studied and the rotation effect was deeply characterized with both experimental and numerical analysis. In this work, the effect of centrifugal buoyancy forces is also taken into account and characterized. The data gathered with the PIV investigation had also been used to validate a numerical model and therefore extend the analysis, providing a complete characterization of the flow field evolution along the channel.
The second part of the research project involves the investigation and complete characterization of the flow field inside an advanced leading edge cooling system, with impingement cooling and film cooling extraction holes. The aim was firstly to be able to correctly set the experiment boundary conditions and constraints, such as equal repartition of mass flow rate between each film cooling hole and maintain the same distribution in both static and rotating tests, in order to avoid a wrong experiment conditioning. Flow field measurements have been conducted mostly in order to evaluate if rotation effect in the jet's alimentation channel could affect its aerodynamics and the interaction between the jet and the coolant extraction holes.

# TABLE OF CONTENTS

# List of Tables

# List of Figures

# Part I

# INTRODUCTION

CHAPTER 1

# GENERAL OVERVIEW ON GAS TURBINES

Gas turbines are one of the most utilized engine in the world throughout different sectors and various applications. Largely employed for propulsion (basically all the aviation and in many nautical sectors), power generation (from humongous combined cycles to micro gas turbines), and auxiliary purposes, this complex system experiences a continuous developing that allows to reach every year higher performances, hence lower primary fuel consumption, lower emissions and lower management costs.

Despite being one of the most complex mechanical system, the macro-architecture of gas turbines is rather simple. As it can be seen in figure 1.1 (a), after an inlet section, air passes through a compressor and then enters the combustion chamber, where it is mixed with the fuel. The combustion gases then expand in a turbine and finally are discharged through a nozzle or a diffuser depending on the specific application (i.e. aeronautical propulsion or other applications).

The typology of each component is chosen depending on the application field of the gas turbine, in fact two main branches can be identified: radial and axial machines, as it can be seen in figure 1.1 (b) and (c). The first typology had been used in the beginning of gas turbine history, due to the easier realization of the compression process with higher efficiency. However, science and technology, mainly pushed by the army aeronautical sector, progressed and allowed to build axial machines that were able to overcome the main issue concerning radial ones: obtain high compression ratios limiting the rotor radial dimension, which is a critical aspect for aircraft engines. Nowadays radial machines are principally employed for low-power applications such as micro-turbogas for distributed energy production.

On the other hand, axial gas turbines are widely utilized for high power installations, such as base-load electric power generation, especially with the development of gas-steam combined cycles, and for aviation and naval propulsion. Since the main object of this dissertation is blade

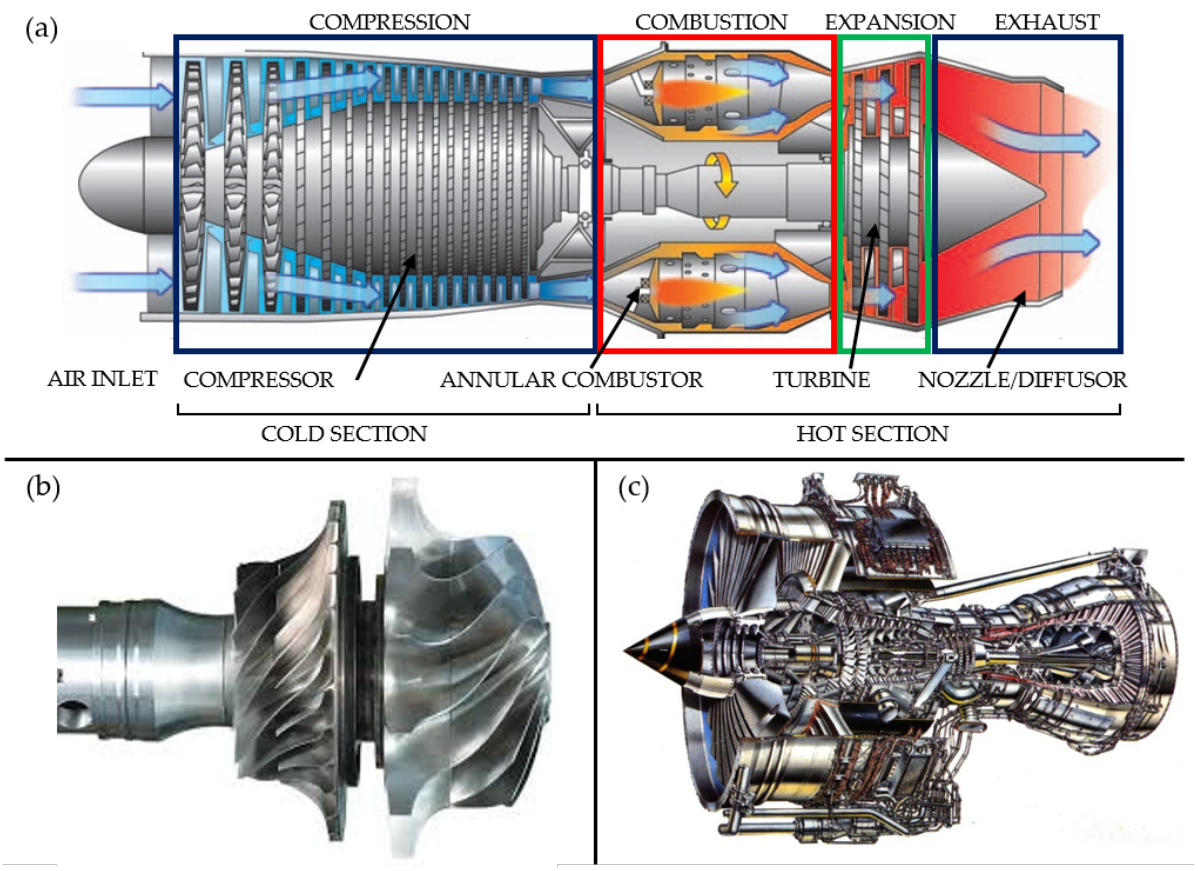


*Figure 1.1: Gas turbine main components (a) and examples of radial (b) and axial (c) architecture*

cooling, and being that a prerogative of the axial machines, from now on the discussion will involve only axial turbines. Axial gas turbines are basically divided in two main categories: aeronautical and land based. Among these two groups, aeronautical are the larger one since their application is spread to the aeronautical field (of course) and others that employ aero derivative gas turbines such as naval propulsion and medium small power plants. In conclusion, aircraft engines and aeroderivative gas turbines compose the most numerous part.

## 1.1 Aircraft engines and aeroderivative gas turbines

The purpose of an aircraft engine is to accelerate a fluid current in order to exploit Newton's third law of motion (i.e. action reaction law) to generate a thrust. Depending on the mechanical component responsible of the thrust generation, aeronautical engines exist in three types: turbojet (figure 1.2 (a)), turbofan (figure 1.2 (b)) and turboprops (figure 1.2 (c)), whose main difference is constituted by the by-pass ratio.
In turbojets, the whole mass flow rate transits through the gas turbine. It is compressed, ignited

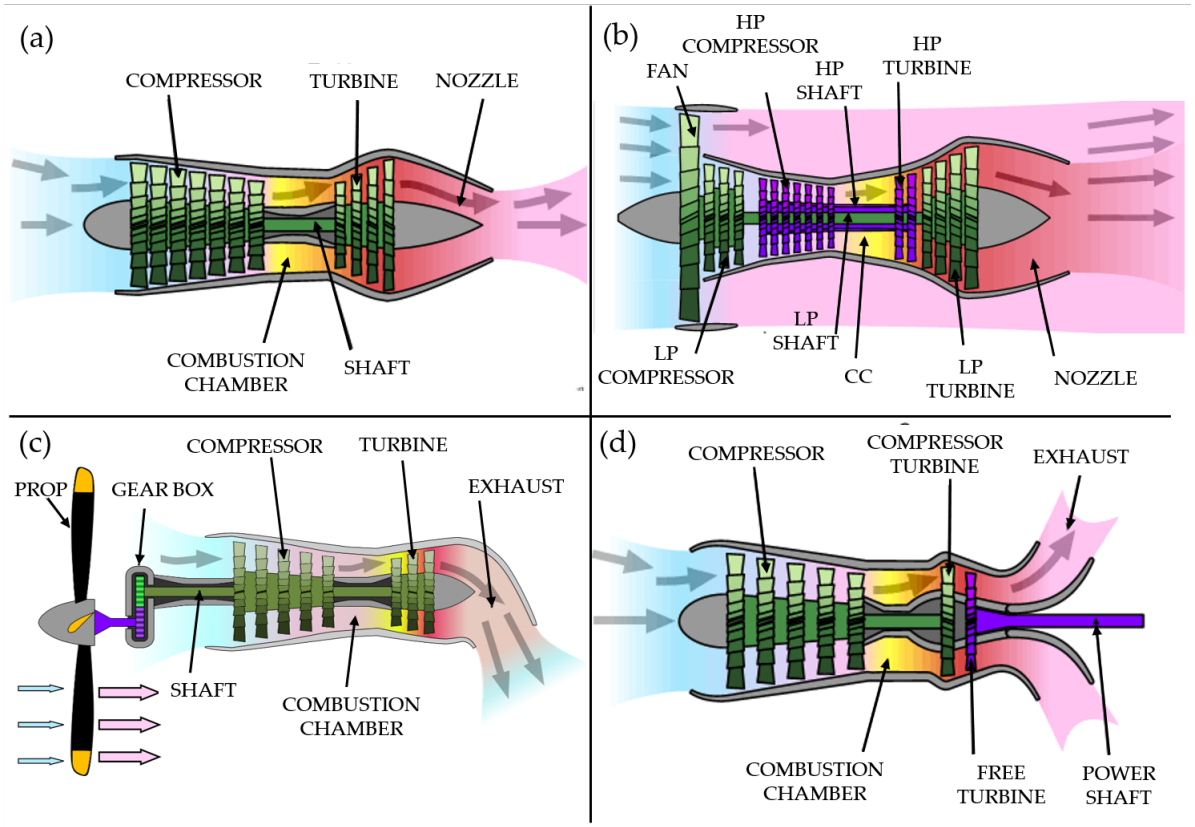


*Figure 1.2: Gas turbines employment in aeronautics: turbojet (a), turbofan (b), turboprop (c) and aeroderivative engine (d)*

with the fuel, expanded in the turbine thus generating the power necessary to spun the compressor and finally exhausted through a nozzle that accelerates the fluid stream (i.e. increasing the momentum with respect the intake), hence generating the thrust. In turbofans, a fraction of the air flow, after passing through a ducted fan, is exhausted outside the turbine main body. The ratio between the two mass flow streams is indeed call by-pass ratio. The advantages of this solution are an higher efficiency in situations like take-off and cruise and the reduction of noise due to the nozzle. By-pass ratio value depends on the specific field of application of the aircraft, in fact, military engines have a lower by-pass ratio in order to use post-burners, while in modern commercial engines, most of the thrust is generated by the ducted fan. Finally, turboprops are basically turbofans with an actual propeller instead of the ducted fan while the gas turbine has only the purpose to generate the power to spin the propeller.

Aeroderivative engines are basically realized starting from aeronautical engines, with different modifications depending on the by-pass ratio. Low by-pass and turbojets are deprived of the nozzle and became *hot gases generators*, which provide the working fluid that is expanded in a power turbine connected to the load as shown in figure 1.2 (d). On the other hand, in high by-pass turbofans and turboprops the ducted fan or the propeller is removed and the gas turbine

is directly connected to the load. The load can be either an electrical load such as a generator or a propeller for naval propulsion.

## 1.2 Gas turbines thermodynamic cycle and efficiency

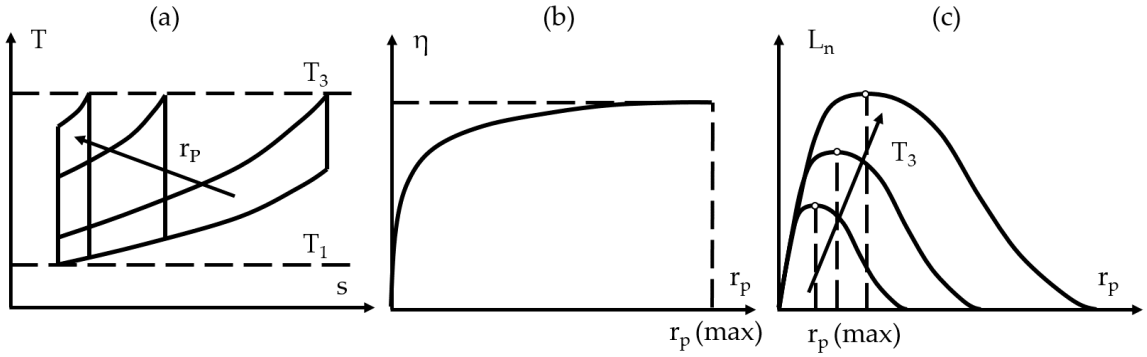


*Figure 1.3: Brayton-Joule cycle at increasing pressure ratio ($r_p$) (a), efficiency ($\eta$) vs pressure ratio ($r_b$) (b) and efficiency ($\eta$) vs pressure ratio ($r_b$) at varying maximum cycle temperatures ($T_3$) (c)*

The thermodynamic cycle governing the functioning of every gas turbine describe in the former paragraphs is the Brayton-Joule cycle. The ideal Brayton-Joule thermodynamic cycle is composed by four transformations: an isentropic compression, an isobaric heat supply, an isentropic expansion and finally an isobaric heat extraction. As it can be inferred, the ideal cycle is designed for a closed cycle where the supply and subtraction of heat occurs in heat exchangers, however, it is still valid for an open cycle where the fourth transformation is assumed to exist just to compute the cycle work and the combustion is endogenous (i.e. involves the working fluid). Cycle main figures are the compression ratio (which in both open and closed cycles is equal to the expansion ratio), maximum temperature (i.e. TIT, turbine inlet temperature) and specific work. From figure 1.3 (b), it can be seen that the cycle efficiency increases with the compression ratio ($r_p$). However, figure 1.3 (a) shows that, once maximum and minimum temperatures are defined (i.e. $T_3$ and $T_1$), the maximum pressure ratio that can be reached determines the cycle degeneration to a particular Carnot cycle with no area, hence without useful work. In fact, figure 1.3 (c) shows that for each fixed maximum cycle temperature ($T_3$), there is a value of the compression ratio that maximizes the cycle work.

The analysis of the gas turbine thermodynamics can be pushed further if the second principle of thermodynamics is considered and the so-called exergetic analysis is performed. This analysis is based on the principle that not all the energy quantities sources can be transformed into mechanical work with the same effectiveness.

According to a standard first principle analysis, the energy content of the fuel that is not converted

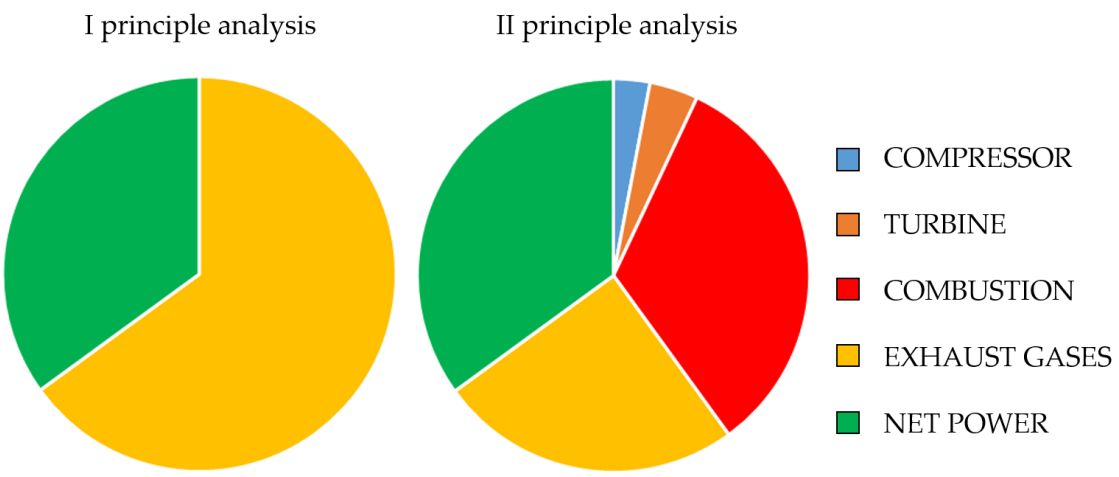


*Figure 1.4: Comparison between first (a) and second (b) principle analysis of Brayton-Joule cycle losses*

into mechanical work is wasted with the high temperature exhaust gases, in the measure of 60% of the total available energy, as it can be seen from figure 1.4 (a). However, second principle analysis (figure 1.4 (b)) shows that only about 30% of the total energy is wasted with the exhaust gases, while almost 40% is lost during the fuel combustion. The reason is that the available energy of the chemical potential of the fuel (calorific power) has to be transformed into heat in order to be utilized in the Brayton-Joule cycle. Heat, however, can be transformed into mechanical work with an efficiency that is dependent on its temperature: the highest the temperature is, the more efficient the process is. As it can be seen, the second principle analysis conclusively shows that the most effective way of increasing the gas turbine efficiency (i.e. Brayton-Joule efficiency) while increasing the work extracted from a fixed fuel quantity, is to increase the combustion temperature, hence the temperature at the inlet of the turbine (TIT).
Nowadays gas turbine combustors operate with a high dilution faction (e.g. $\lambda = 50$), hence the margin of temperature increase until the stoichiometric quantity of air is extremely vast. However, the path to follow is strongly limited by mechanical resistance at high temperatures of the turbine components, in particular the blades of the rotors that are subjected to the stress generated by the centrifugal force and damaged with the phenomenon called creep. This phenomenon of mechanical failure involves the fracture of the blade at the root, mainly in the trailing edge area. In order to solve this huge problem, mainly two path are possible: design new materials with enhanced mechanical characteristics, or cool the sensible components. Research is moving in parallel between these two branches, however, blade cooling has a direct impact on the efficiency and the developments in this field are intimately connected with the advancement in temperature increase throughout the years.

## 1.3 Blade Cooling

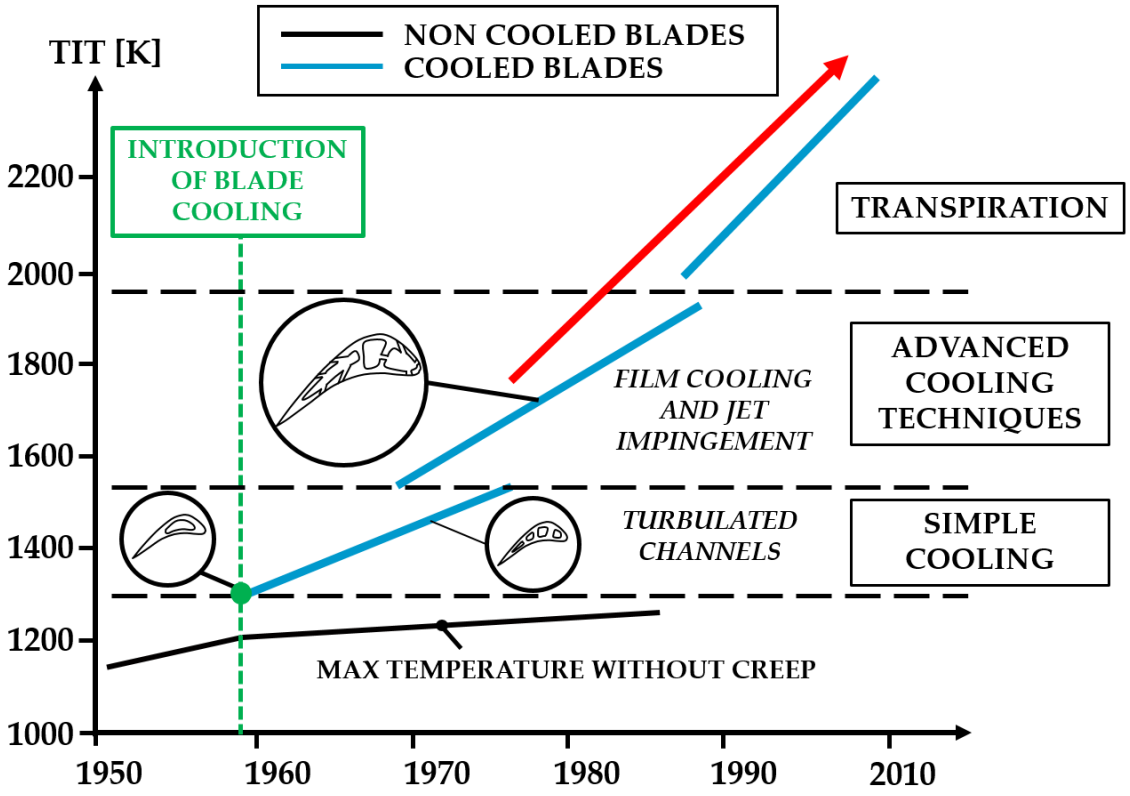


*Figure 1.5: Evolution of maximum temperature and cooling techniques*

Blade cooling has seen a strong impulse in development in the last 70 years as shown in figure 1.5. In fact, from the early years hollow blades where coolant flowed straight radially outward, cooling system have evolved to complex serpentines, in a successful attempt to optimize the cooling process.

Before entering in the detailed description of the evolution of cooling systems, it is worth discussing the thermodynamics implications of its implementation. A cooling process, thermodynamically, is the transfer of heat from a source at higher temperature to a sink at lower temperature, and since nothing gets destroyed but only degrades along these processes, it could be interesting, in order to increase the overall plant efficiency, to recover that energy subtracted to the blade metal. For this reason, the cooling system of a turbine, depending on its application, can be either an open or a closed loop. In an open loop cooling system, the coolant is air spilled from the compressor at stages of compression compatible with the channels pressure losses and main flow overall pressure level. Since it is working fluid for whom energy had been spent for, the obvious solution is to discharge the coolant back into the fluid stream that is expanding through the turbine. In this way, air will be discharged at a higher temperature but a pressure lower than

the one it is spilled (due to the cooling system pressure losses), hence providing a partial energy recovery.
In closed cycles, the coolant can be either steam or an air-steam mixture. The employment of steam is dictated by the will of increase the heat transfer using a working fluid with higher specific heat constant. The steam comes of course from the steam power plant in cascade of the gas turbine and the cooling system can be exploited for the re-heating process of the steam between the various turbine stages.
The first solution is clearly the most common since it is the one employed for aeronautical engines, hence all aeroderivative gas turbines, while the closed cycle can be employed only for land based gas turbines.
On the basis of this brief discussion on the thermodynamics implications of blade cooling, it can be clearly understood that it is mandatory to design cooling system that provide the highest degree of cooling with the least amount of air spilled from the compressor and pressure losses. Unfortunately, the last condition is in contrast with the quest for higher heat transfer, since the latter is promoted by flow turbulence, which is nothing but a mechanism of flow energy dissipation, hence pressure losses. The other mandatory feature of a cooling system design is to provide an uniform heat transfer in order to avoid hot and cold spots, which are responsible of the insurgence of thermal stress. For these reasons, cooling systems have become extremely complex and consist in the combination of several cooling techniques, each of them is optimized for the cooling of a specific blade zone.

### 1.3.1 Turbulated channel cooling

Internal forced convection has been the first solution employed for blade cooling. In the beginning, inside blades were realized straight cylindrical channels inside whom coolant flowed from hub to tip, where it was then discharged and provided also the cooling of the casing. Nowadays the internal channels are complex serpentines with different cross sections depending on the blade zone. In fact, channels in the leading edge zone have a cross section close to a triangular shape in order to fit in the blade nose, while moving towards the trailing edge, the cross section shape changes from triangular to rectangular with various aspect ratios. Finally, in the trailing edge, the cooling channels are basically a trapezoid with parallel sides (wedge like shaped channels).
On top of this, various features are realized on the interested surface in order to enhance the heat transfer by disrupting the dynamic and thermal boundary layer and increasing flow turbulence and mixing. The solution is to design a sort of protrusion, called turbulence promoter, whose shape has to fulfil the task described before without increasing too much pressure losses. Turbulence promoters can also be designed to redirect near wall flow in a convenient way in order to provide sufficient cooling throughout the whole channel. Most common turbulence promoters are ribs and pin-fins.
Ribs are ideally parallelepiped with usually a squared section that has the treble function

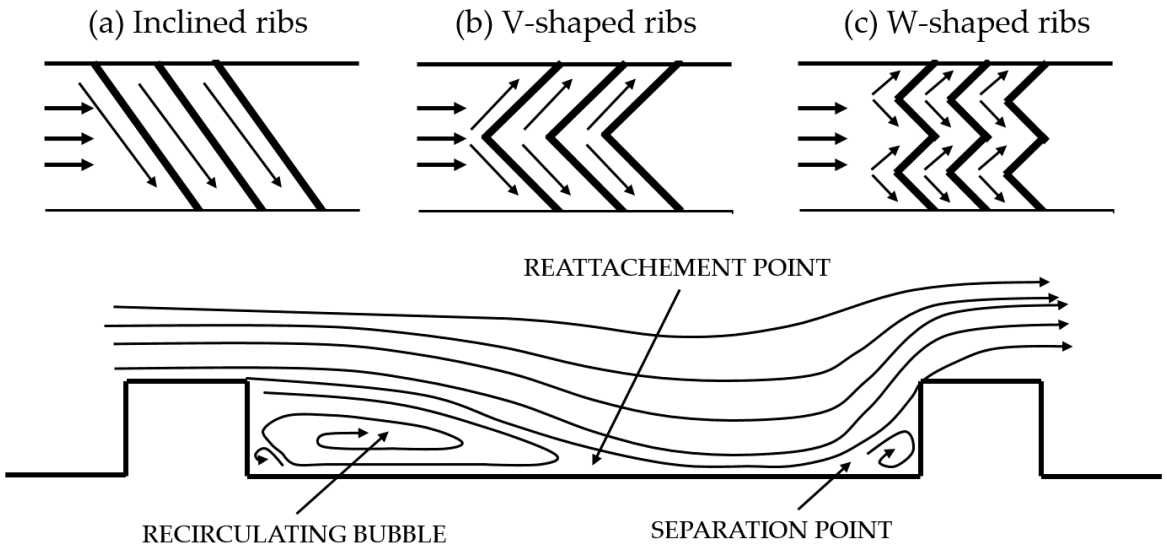


*Figure 1.6: Examples of rib arrangements, (a) through (c) and flow field feature between the turbulence promoters (d)*

of disrupting the boundary layers development, increase flow velocity due to the reduction of the passage cross section and generate near wall secondary flow [2]. Moreover, the interaction between the accelerated flow over the obstacle and the slower recirculating zone always present downstream the turbulence promoter generates a shear layer that promotes the mixing of colder core flow with the hotter near wall flow.
Turbulence promoters exist in various shapes such as straight, V-shaped, W-shaped and their variations (figures 1.6 (a) to (c)), like ribs that are not continuous along the transverse direction.

### 1.3.2 Matrix cooling

In certain blade zones, it is rather difficult to provide cooling through isolated channels when their aspect ratio is rather low, since it is complicated to ensure all the zones to be reached by the coolant. The most common example is the trailing edge cooling channel, which has to be realized in a zone where the blade thickness approaches zero, and usually wedge - shaped channels are employed. In situations like these, a common solution is the matrix cooling, where a principal cooling channel is divided in an intricate maze of minor channels.

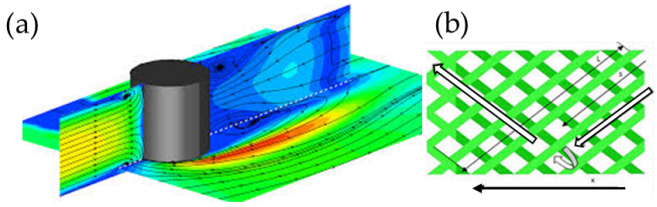


*Figure 1.7: Flow structure around a pin (a) and example of flow distribution in a matrix cooling channel (b)*

So-called wedge-like channels are often provided with a matrix of small pillars (i.e. pin-fins) that define the path of secondary channels. In this way a threefold result is achieved: coolant can be distributed through the whole channel, heat transfer is enhanced and structural integrity is improved with respect to a hollow channel (i.e. without the pin-fins).

### 1.3.3 Concavity surface cooling

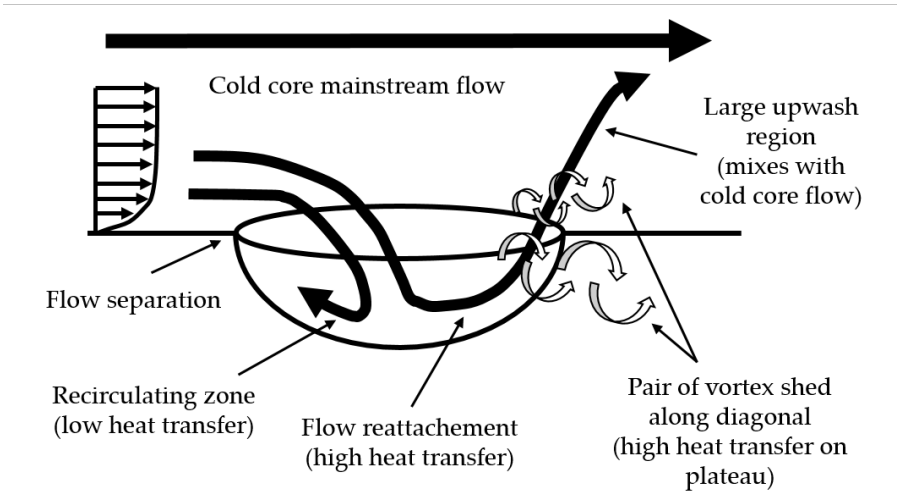


*Figure 1.8: Flow structure inside a dimple*

The enhancement of the heat transfer can be achieved also with recessions in the surface rather than projections (e.g. the former turbulence promoters). These features are known as concavities or more commonly as dimples. Among the various geometries that can be adopted for the depressions, the spherical cap is mostly famous for its drag reduction properties in external flows (e.g. golf balls, marine vessels). Concerning their application to the cooling enhancement, the fluid dynamic principle on which their application relies is the generation of organized vortical structures that, being less chaotic than shear layers (e.g. generated by protruding obstacles described in the previous paragraph), are more efficient in promoting flow mixing [3].

### 1.3.4 Impingement cooling

In zones where the cooling is particularly critical, such as the leading edge, where the surface is limited and the thermal loads extremely high, or in the trailing edge, where the blade thickness is pushing the limit for the blade structural integrity, one of the most efficient ways to increase the heat transfer is to realize jets that impact on the target surface, realizing the so called impingement cooling.
Impingement cooling channels are realized in two contiguous parts (i.e. feeding channel and impingement channel) connected through a perforated wall that allow to realize the cooling jets [4].

The jet holes can have several shapes and distributions throughout the channel and the jets can impinge in a channel where air is discharged from one extremity, hence generating a certain cross flow that affects the heat transfer along the blade height, or can feed the film cooling holes. In the latter case, jets are divided in isolated groups along the blade height. The drawback of the impingement is the high pressure drop. Indeed, the heat transfer is highly enhanced since the jets have a velocity that can easily be an order of magnitude higher with respect the bulk velocity in the feeding channel, but their dynamic pressure is mostly dissipated in the impact with the target surface and the vortical structures then generated.

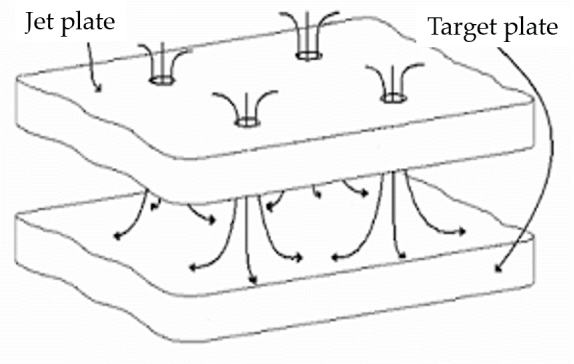


*Figure 1.9: Impingement cooling functioning principle*

### 1.3.5 Film cooling

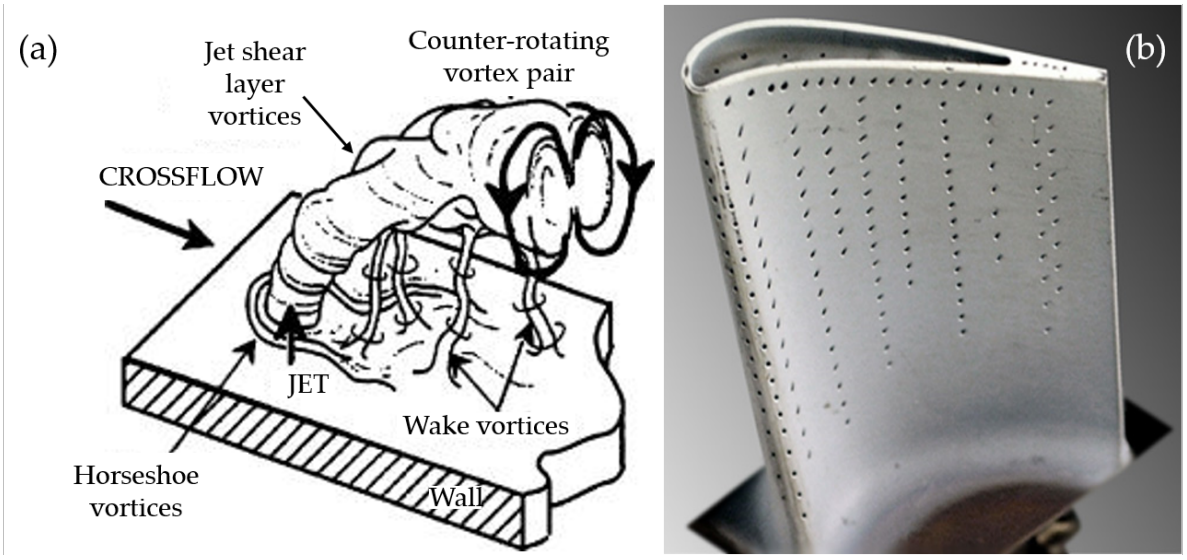


*Figure 1.10: Flow structure of jet outside a cooling hole (a) and cooling holes on a real blade (b)*

After passing through the intricate serpentine of channels inside the blade, coolant is then discharged in the main flow through openings on the blade wall, in order to realize the so-called the film cooling. The purpose is to realize a dynamic coating of cold fluid that protect the blade surface from the stream of hot gases [5]. The openings can be either small holes bigger slots. Holes are usually realized on the blade leading edge, on the first halves of pressure and suction

sides and even on the turbine hub and casing. Slots are often realized in the trailing edge zone of the suction side, guaranteeing an efficient cooling of this critical zone with an high amount of air and removing part of the material to be cooled while preserving a safe blade thickness. This latter solution is called cut-back. Film cooling design has to take into account the complex interaction between the internal air discharged and the main flow.

### 1.3.6 Future advancements

The cooling techniques treated in the former paragraphs are basically the bricks on whom blade cooling had been built from its birth to the modern days and will still play a major role in the future. However, in recent years some new cooling philosophies have been developed in order to further increase heat transfer efficiency and improve temperature uniformity throughout the whole blade surface. These new cooling techniques, however, are more dependent on the advancement in the manufacture technology. Micro cooling is a sort of macroscopic version of the former, indeed in this scheme the classic cooling serpentine is present inside the blade, however, the coolant is brought directly inside the blade wall, were micro impingement channels are realized.

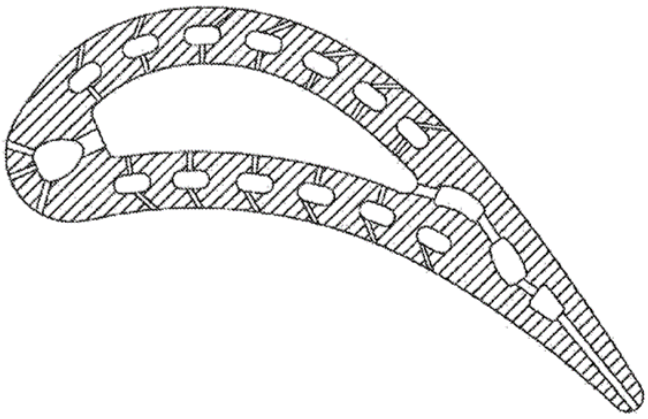

*Figure 1.11: Skin cooling scheme*

Transpiration cooling relies on the employment of porous media for the realization of blades. In this way the blade is basically in contact with the coolant at molecular level.

### 1.3.7 Full blade cooling scheme

The cooling of the complete blade is always a combination of the techniques presented in the previous paragraphs. Moreover, cooling schemes design strongly depend on the turbine stage where the blade is located in (i.e. thermal load) and if the blade is in the rotor or the stator.
In first stage rotor blades, where the thermal and mechanical loads are the highest, coolant is provided from the hub in two locations where different serpentines are responsible of the cooling either of the front part of the blade or the central and rear part. The front part of the cooling is usually provided with an impingement system, whose coolant is then fed to the film cooling of the blade leading edge. In the central part there are multiple channels connected with turns and provided with turbulence promoters. The last channel is the trailing edge cooling channel, where

matrix cooling is realized. Part of the coolant is extracted at various locations of the passages in order to realize the film cooling of sensible parts or ejected at the tip to cool the gas turbine casing. The trailing edge cooling channel is always provided with some form of coolant ejection in the main flow as cut back or trailing edge slots.
In second stage blades, the structural stresses are less demanding in terms of cooling due to the reduced main flow temperature , hence simpler schemes are employed. The typical cooling scheme for these blades is a three channel serpentine, where coolant is provided from the leading edge hub and discharged along the trailing edge. Film cooling could be avoided to ease the manufacturing process, and channels are provided with turbulence promoters.

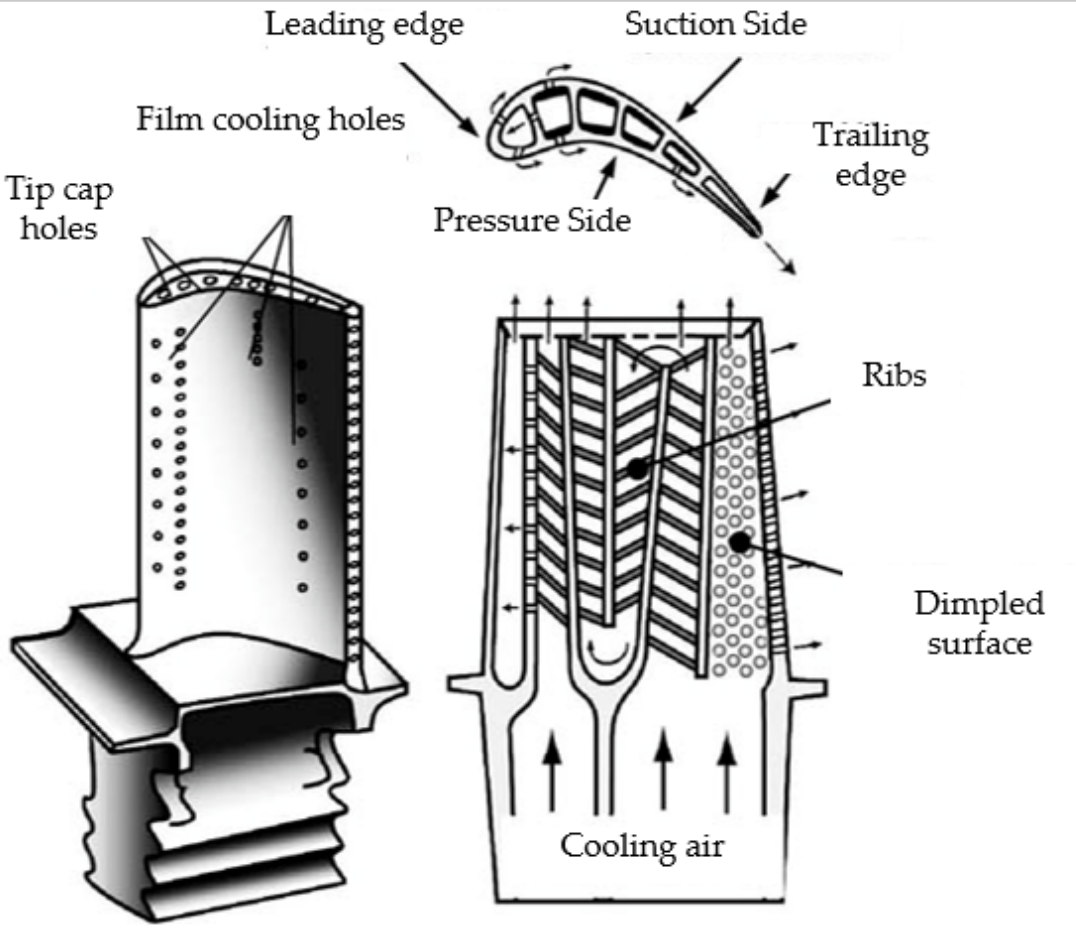


*Figure 1.12: Complete cooling scheme*

### 1.3.8 Cooling of the blade leading edge

The leading edge, as previously mentioned in the cooling techniques description, is one of the most critical zones of the entire blade. Indeed, it is faced directly towards the hot gases stream and on a small surface has to dissipate a high thermal load, reaching easily high temperatures. Moreover, due to the blade profile shape it is not easy to accommodate a cooling channel while maintaining a simple cross section. In fact, in other blade zones, channel cross sections can be squared, rectangular with various aspect ratios or at least wedge-shaped (trapezoid). In the leading edge, the channel cross section must be at least triangular equilateral, however in many real application at least one side is curved. As already said, in advanced leading edge cooling systems the cooling is provided by a combination of impingement and film cooling, complicating even more the design.

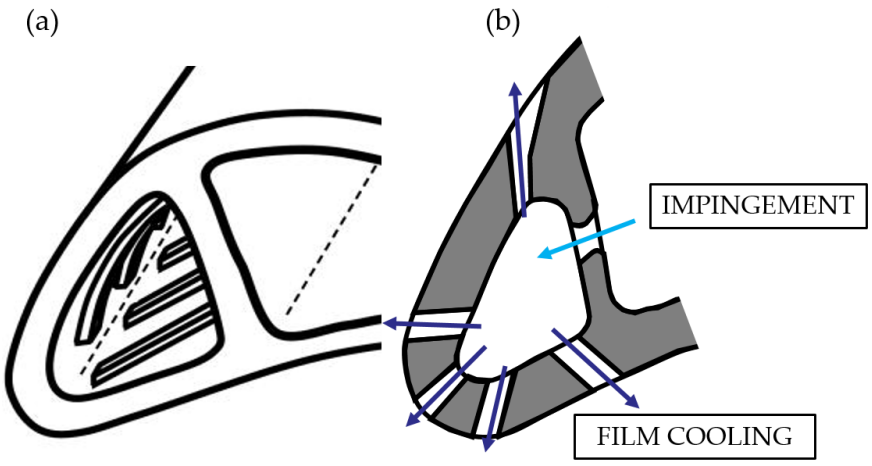


*Figure 1.13: Cooling schemes for the leading edge: turbulated channels (a) and impingement cooling with extraction holes*

CHAPTER 2

# BACKGROUND OF THE PRESENT WORK

In order to easily follow the discussion of the campaigns' results and understand the purposes of this work, it is worth to discuss the major effects of apparent forces on flows in rotating frames of reference. More in detail, confined flows (e.g flows in rotating ducts) will be depicted and the available literature on both the rotation effects in blade cooling and leading edge cooling systems will be reviewed.

## 2.1 Flows in rotating frame of reference

### 2.1.1 General formulation

Governing equations of the flow motion are the well-known Navier-Stokes equations, which under the assumption of incompressible flow, isothermal conditions and Newtonian fluid can be written in the following vectorial notation with respect an inertial frame of reference:

$$\frac{\partial \mathbf{u}}{\partial t} + (\mathbf{u} \cdot \nabla \mathbf{u}) = -\frac{\nabla p}{\rho} + \mathbf{g} + \nu \Delta \mathbf{u} \tag{2.1}$$

If the equation is rewritten with respect a non-inertial frame of reference, e.g. a frame of reference rotating with an angular velocity of $\Omega$, two additional terms representing the apparent forces appear:

$$\frac{\partial \mathbf{u}}{\partial t} + (\mathbf{u} \cdot \nabla \mathbf{u}) = -\frac{\nabla p}{\rho} + \mathbf{g} + \nu \Delta \mathbf{u} - \Omega \times (\Omega \times \mathbf{r}) - 2\Omega \times \mathbf{u} \tag{2.2}$$

The first one is the centrifugal force that can be rewritten as $(\Omega \times (\Omega \times \mathbf{r}) = -1/2\nabla[(\Omega \times \mathbf{r}) \cdot (\Omega \times \mathbf{r})]$. Since the gravitational field is a conservative force, it also can be rewritten as the divergence of a scalar field $\Phi$, allowing to group these two terms with the pressure gradient, thus redefining

$p^*$ as the sum of all pressures that are not caused by neither gravity nor centrifugal forces. The resulting equation is:

$$\frac{\partial \mathbf{u}}{\partial t} + (\mathbf{u} \cdot \nabla \mathbf{u}) = -\nabla p^* + \nu \Delta u - 2\Omega \times \mathbf{u} \tag{2.3}$$

The remaining additional term is the Coriolis force. To better understand the physical implications of this formulation, the pressure gradient can be made dimensionless dividing each equation member by the group $\rho U L \Omega$. The dimensionless equation becomes:

$$\frac{\partial \mathbf{u}}{\partial t} + Ro(\mathbf{u} \cdot \nabla \mathbf{u}) = -\nabla p^* + Ek \Delta \mathbf{u} - 2\Omega \times \mathbf{u} \tag{2.4}$$

Where:

$$Ro = \frac{U}{\Omega L} \tag{2.5}$$

is the Rossby number (i.e. the ratio between inertial and Coriolis forces)

$$Ek = \frac{\nu}{\Omega L^2} \tag{2.6}$$

is the Ekman number (i.e. the ratio between viscous forces and Coriolis forces).
This formulation is suitable to describe the flow field of non-confined flows in rotating frames of reference. The best example of this kind of problem is the investigation of atmospheric flow field.

### 2.1.2 Confined flows

Confined flows are of obvious interest for the blade cooling research field. In the following, the main rotation effects will be described in the general case of squared smooth channels in orthogonal rotation (i.e. duct axis is perpendicular to the rotation vector) as depicted in figure 2.1, considering at first isothermal conditions and then discussing the additional effects rising from thermal effects. In order to discuss properly rotation effects, it is useful to analyze Navier-Stokes equations in a rotating frame of reference using as reference length the duct diameter (d) instead of a generic quantity (L).

$$\frac{\partial \mathbf{u}}{\partial t} + (\mathbf{u} \cdot \nabla \mathbf{u}) = -\nabla p^* + \frac{1}{Re} \Delta \mathbf{u} - 2Ro\Omega \times \mathbf{u} \tag{2.7}$$

Where now:

$$Ro = \frac{\Omega d}{U} \tag{2.8}$$

Considering a rotating duct in isothermal conditions, where the main flow is radially outward (as sketched in figure 2.1), the governing equation can be written for the three components as:

$$\frac{\partial u}{\partial t} + u\frac{\partial u}{\partial x} + v\frac{\partial u}{\partial y} + w\frac{\partial u}{\partial z} = \frac{\partial p^*}{\partial x} + \frac{1}{Re}\frac{\partial^2 u}{\partial x^2} - 2Ro\Omega_z \times v \tag{2.9}$$

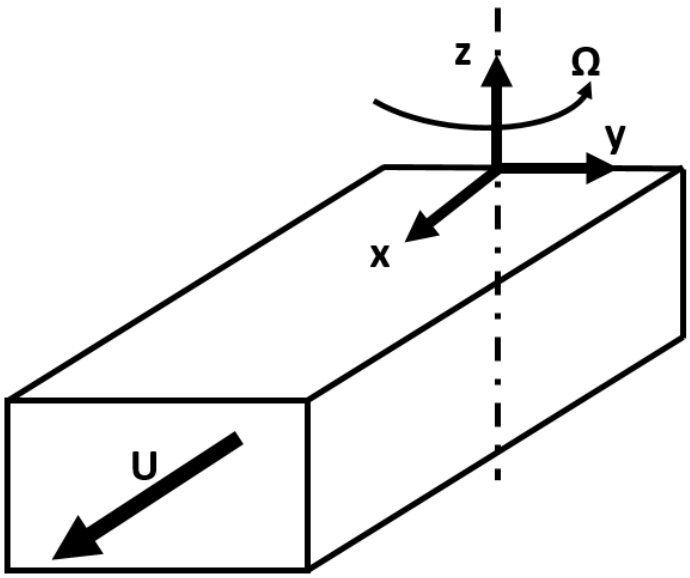


*Figure 2.1: Sketch of a squared channel in orthogonal rotation, radial main flow direction*

$$\frac{\partial v}{\partial t} + u\frac{\partial u}{\partial x} + v\frac{\partial v}{\partial y} + w\frac{\partial v}{\partial z} = \frac{\partial p^*}{\partial y} + \frac{1}{Re}\frac{\partial^2 v}{\partial y^2} - 2Ro\Omega_z \times u \tag{2.10}$$

$$\frac{\partial w}{\partial t} + u\frac{\partial u}{\partial x} + v\frac{\partial w}{\partial y} + w\frac{\partial w}{\partial z} = \frac{\partial p^*}{\partial z} + \frac{1}{Re}\frac{\partial^2 w}{\partial z^2} - 2Ro \tag{2.11}$$

At the inlet of the test section, there will be a uniform velocity distribution and along the channel, boundary layers will develop near the walls. Since only one component of velocity is present, only the Coriolis force component along the y axis (i.e. $2Ro\Omega_z u$) acts on the flow.
At the core flow, due to the former consideration and the fact that Re is extremely high, the equation 2.10 can be simplified as follows:

$$\frac{\partial p}{\partial y} = 2Ro\Omega_z u \tag{2.12}$$

The meaning is that the Coriolis force acting along the tangential direction is counter balanced by a pressure gradient, with pressure increasing towards the trailing side.
As flow develops, fluid near channel walls will decrease its velocity (i.e. due to the development of boundary layers), hence the Coriolis force acting on top and bottom flow layers is reduced with respect the component acting on the central bulk flow, while pressure remains constant along the duct height. Indeed, flow development causes an imbalance between pressure and Coriolis force

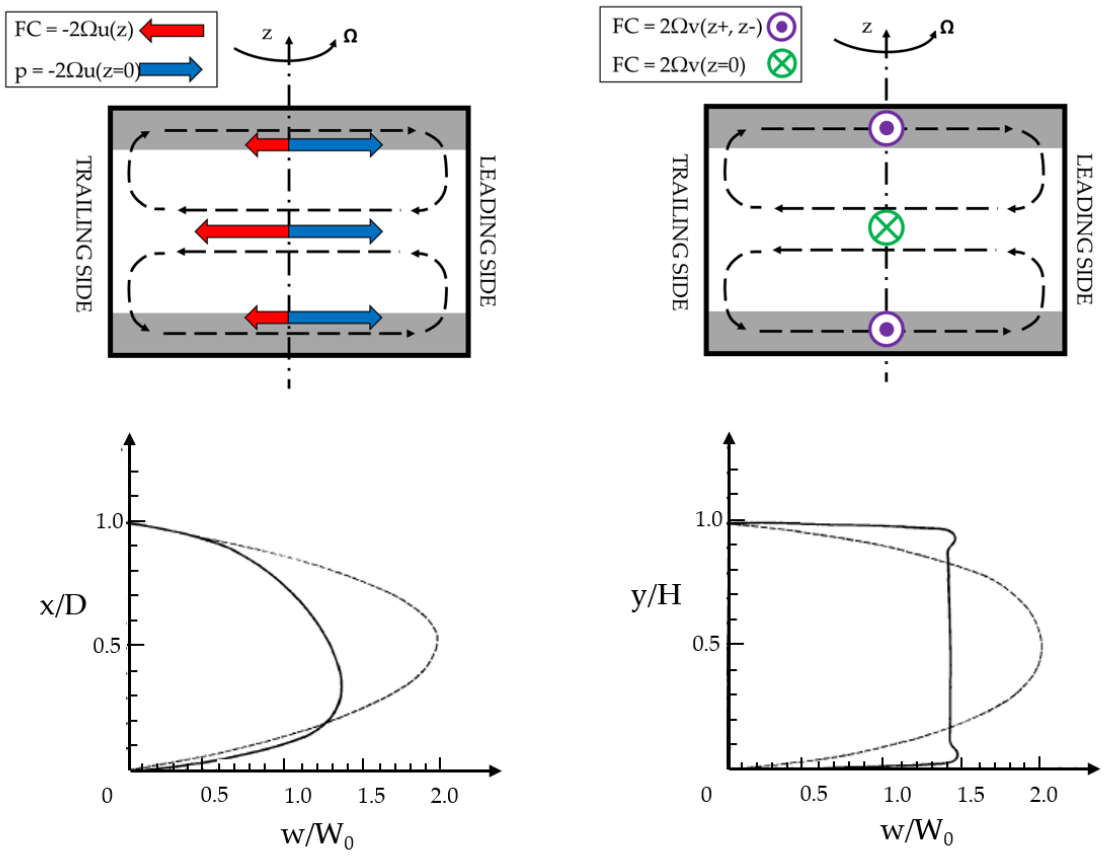


*Figure 2.2: Rotation effects: (a) main component of Coriolis force effect, (b) velocity profile extracted from horizontal symmetry plane, (c) secondary Coriolis force component, (d) velocity profile extracted from vertical symmetry plane (data from Speziale [6])*

in upper and lower boundary layers that determines the migration of near wall fluid towards the leading side as depicted in figure 2.2 (a). Since the mass conservation law has to be respected, this near wall flow organizes itself in two counter rotating vortices, hence pushing bulk flow towards the trailing side.

The fact that the cross section is symmetrical with respect both the vertical and horizontal axes, determines also the symmetry of the counter rotating vortices. For this reason the separation and reattachment zones are located respectively at the leading and trailing mid height.

This secondary flow structure has a primary effect of displacing high momentum fluid towards the trailing side, bending the velocity profile in the central plane as it can be seen in figure 2.2 (b). The secondary effect is the rise of velocity components perpendicular to the main bulk flow direction. These additional velocity components, determine additional Coriolis force components, parallel to the main flow direction, as shown in figure 2.2 (c). More in detail, these Coriolis components

determines an acceleration of the upper and lower boundary layers, while the central layers are decelerated. This effect is particularly evident if a velocity profile is extracted along the vertical symmetry axis (figure 2.2 (d)).

These secondary flow structures and the resulting Coriolis force components continue to evolve

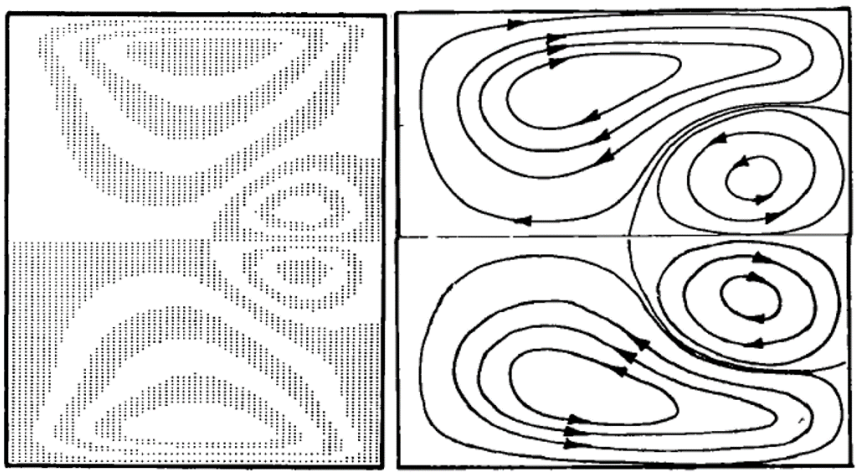

*Figure 2.3: Secondary flow structures for high rotation number. Contours obtained by Speziale [6] and stream tracers from Cheng et al.[7]*

as the flow moves along the radial direction. In particular, the counter rotating vortices determine an accumulation of low momentum fluid near the leading side, causing a decrement of the bulk velocity to levels comparable to the one found in the boundary layers. When this particular condition is reached, the Coriolis component cannot counterbalance the pressure gradient, thus determining a reversal of the flow and the formation of an additional counter rotating couple of vortices. This secondary flow structure configuration is depicted in figure 2.3, where the numerical results of Speziale [6] and Cheng et al. [7] are reported.

This evolution can be hastened if stronger rotational effects are considered, hence increasing the rotation speed at constant Re, e.g. increasing the intensity of Coriolis force with respect inertial force (i.e. increase of Ro).

When non-isothermal conditions are taken into account is generally accepted to apply the Boussinesq approximation. In this way the only temperature-dependent term still present in the equation is the centrifugal force. The dimensional equation is:

$$\frac{\partial \mathbf{u}}{\partial t} + (\mathbf{u}\cdot\nabla\mathbf{u}) = -\nabla p^* + \frac{1}{Re}\Delta\mathbf{u} - 2Ro\Omega\times\mathbf{u} - \beta(T-T_\infty)\Omega\times(\Omega\times\mathbf{r}) \tag{2.13}$$

While the non-dimensional form becomes:

$$\frac{\partial \mathbf{u}}{\partial t} + (\mathbf{u}\cdot\nabla\mathbf{u}) = -\nabla p^* + \frac{1}{Re}\Delta\mathbf{u} - 2Ro\Omega\times\mathbf{u} - Bo\Omega\times(\Omega\times\mathbf{r}) \tag{2.14}$$

Where:

$$Bo = \frac{(T - T_\infty)}{T}\left(\frac{\Omega d^2}{U}\right)\frac{R}{d} = \frac{\beta(T - T_\infty)\Omega^2}{\nu\alpha}\frac{\alpha}{\nu}\frac{\nu}{Ud} = \frac{Ra_\Omega}{PrRe^2} \tag{2.15}$$

Bo is the centrifugal buoyancy number, which represents the ratio between centrifugal and inertial forces. This dimensional group is the analogue of the Richardson where the Rayleigh number is computed considering the centrifugal force instead of the gravity force. The Bo can be rewritten in a more convenient way for this application:

$$Bo = DR\ Ro^2\frac{R}{d} \rightarrow DR = \frac{(T - T_\infty)}{T} \tag{2.16}$$

The effect of the component acting along the radial direction is analogous to the formerly described effect of the Coriolis force component acting transversally on the cross section.

At the inlet of the test section the temperature is uniform throughout the cross section, hence the

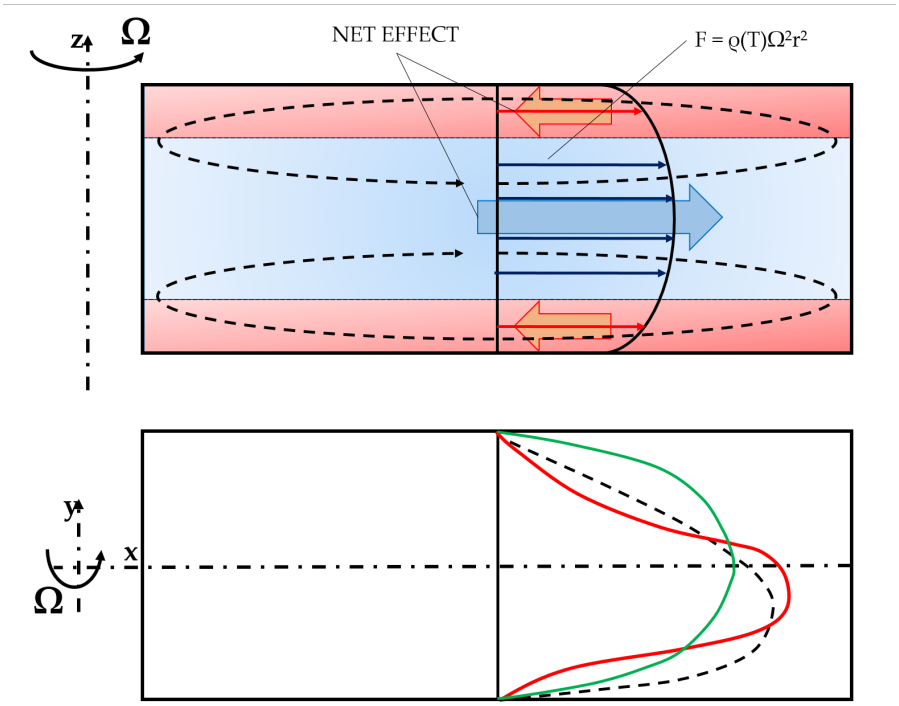


*Figure 2.4: Sketch of a rotating channel with closed extremities and buoyancy forces: net secondary flow structure caused by the radial component*

density and the resulting centrifugal force. As flow develops, thermal boundary layers develop as well, determining an imbalance of centrifugal force between the bulk flow and the boundary layers. This effect can be modelled considering as an example a duct with both extremities closed subjected to orthogonal rotation. The temperature gradient determines an imbalance between the centrifugal force acting on the core flow and the boundary layers, determining an

acceleration of the core flow towards higher radii with respect the boundary layers. However, since the duct is closed, there cannot be a mass flow inside the duct, hence, in order to satisfy the mass conservation principle fluid near the wall must flow towards lower radii. The secondary structure that develops is then composed by two counter rotating vortices in the streamwise direction, as sketched in figure 2.4 (a). This structure determine a near wall flow towards lower radii.
The net effect of this centrifugal force component on a duct with open extremities, is to thicken the boundary layers where the thermal gradient is concentrated while increasing the peak of bulk velocity (i.e. the mass flow rate has to remain constant) as shown in figure 2.4 (b).
The other component acts more like the conventional gravitational buoyancy, exploiting the density gradient to push “heavier fluid ”towards the walls, hence displacing near wall “lighter fluid”towards the center of the duct. On the contrary of previously described phenomena that organize in macroscopic secondary flows that interest the whole channel topology, the latter are confined to the near wall fluid layers, where both the considered centrifugal force component and thermal gradients are higher.

## 2.2 Rotating channels in blade cooling

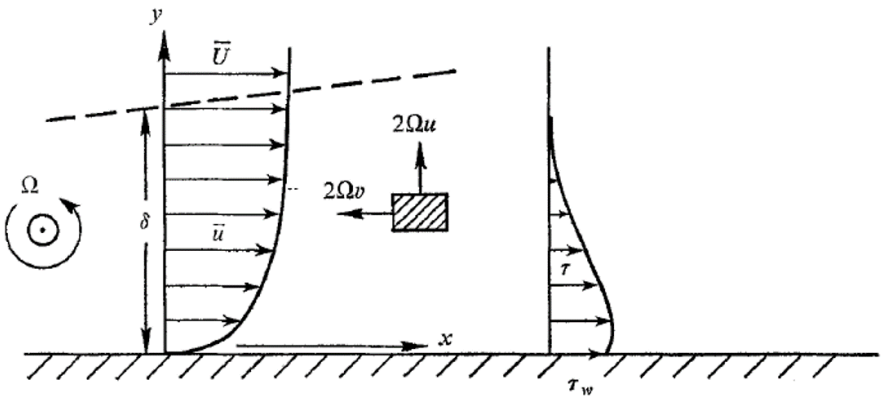


*Figure 2.5: Effect of Coriolis components on fluid particles inside the developing boundary layer (instability condition)*

The study of smooth channels allow to deepen the understanding of the physics at the basis of the fluid transport in rotating channels. However, smooth channels are of little to none interest for blade cooling applications. As explained in chapter I, one of the most common cooling technique is indeed the employment of turbulated channels. The interaction between secondary flow structures induced by the turbulence promoters and rotation is extremely critical for cooling efficiency and uniformity. Johnston [8] shows that in the duct zones where the underground vorticity (i.e. rotation of the duct) is parallel to the flow vorticity (i.e. boundary layers) a different effect of flow stabilization is determined depending on their relative orientation. In particular,

when vectors have the same orientation the flow is destabilized, hence more turbulent, as shown in figure 2.5. On the other hand, where the two vectors have the opposite direction the flow is stabilized. These two conditions occur respectively on the trailing and the leading side of the rotating duct.

These phenomena have a strong impact in the recirculating structures between turbulence

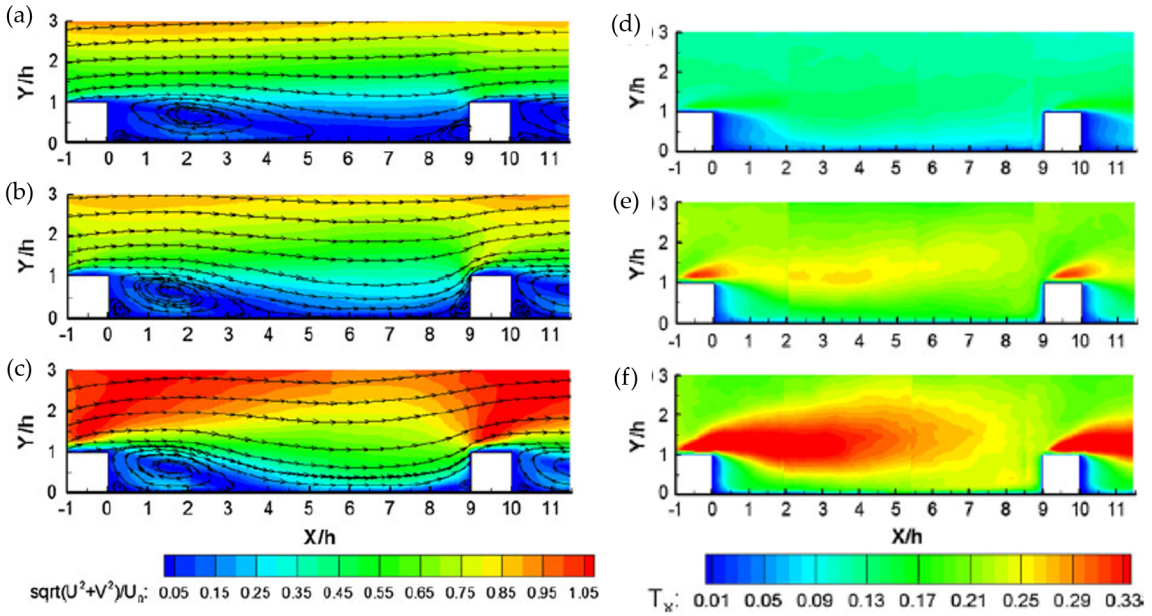


*Figure 2.6: Recirculating flow structures (a-b-c) and turbulence intensity (d-e-f) from Coletti et al. [9]*

promoters. Coletti et al. [9] investigated the flow field between the turbulence promoters (i.e. squared ribs perpendicular to the radial direction) by means of PIV inside a squared channel at two different rotation numbers. The test section consist of a squared channel with aspect ratio AR = 0.9 with one ribbed side. Ribs are perpendicular to the flow direction with a spacing of 10h. The flow fields showed that the stabilizing effect caused an increase of the reattachment length downstream the rib at the leading side (figure 2.6 (a)), while a reduction on the trailing side (figure 2.6 (c)) compared to the non-rotating case (figure 2.6 (b)). These trends were confirmed for a higher rotation number, where further increase/decrease of the recirculating structures were detected. Moreover, the turbulence intensity plots confirmed an increase on the trailing side, while turbulence intensity levels were reduced on the leading side with respect the non-rotating case.

The analysis was further extended for the case of Ro = 0.38 considering also the effect of centrifugal buoyancy forces. For the investigation of buoyancy effect, the ribbed wall is made of copper and heated by means of Joule effect. Despite not providing real engine thermal boundary conditions, the setup allowed to deepen the understanding of the flow physic.

The results confirmed the same trend for the trailing side, where almost a saturation of the

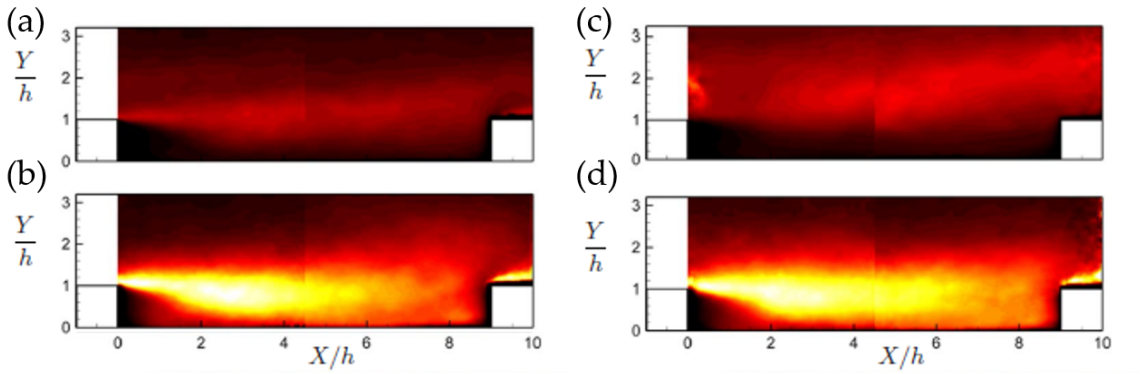


*Figure 2.7: Velocity fluctuations in the isothermal case (a-b) and non-isothermal case (c-d) from Coletti et al. [10]*

recirculating structure was reached, while on the leading side an expansion of the recirculating structure throughout the inter-rib region was measured. However, the most interesting result obtained with the non-isothermal tests regarded the velocity fluctuations. Indeed, Coletti et al. [10] found that in the non-isothermal cases, velocity fluctuations were always higher in comparison with the respective isothermal case, with the leading side being always the condition with lower levels with respect the other cases, as it can be seen from the contours in figure 2.7.

### 2.2.1 Leading edge cooling systems

Concerning the research on leading edge cooling channels, the available literature can be divided in two major branches, regarding either simple stereotyped geometries (e.g. triangular cross-section, one passage) or advanced cooling systems (e.g. impingement and coolant bleeding).

The first category represents the bulk of the open literature on leading edge cooling system, where the most important works have been made by professor Han's research team at Texas A & M. In a series of experimental campaigns, they completely characterized the thermal behavior of a triangular equilateral cooling channel in both static and rotating conditions. Performances of several combinations of ribs orientation are reported in [1], while in [11] the effect of channel stagger angle was also considered.

The experimental activity is carried out in a rotating facility where the test section is pressurized (respectively figures 2.8 (a) and (b-c)). Several slips rings allow data communication with the sensors on the rotating equipment. The experimental technique employed to obtain these thermal data is largely used among the scientific community and relies on the measurement of several temperatures on the test section internal walls. The test section walls are realized with several copper plates, each of them hosts a thermocouple. Every copper plate can be heated by Joule

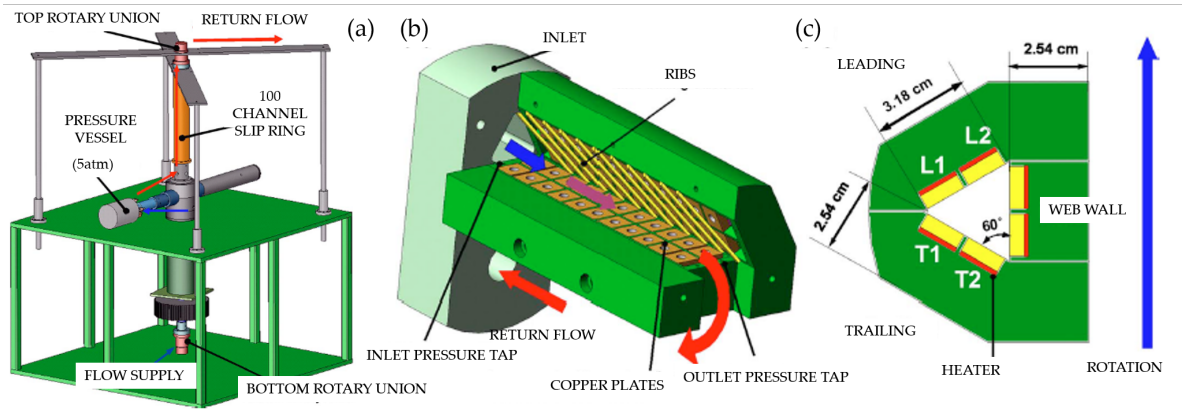


*Figure 2.8: Rotating test rig for heat transfer measurements (a) and leading edge test section (b, c) used for the experiments described in [1]*

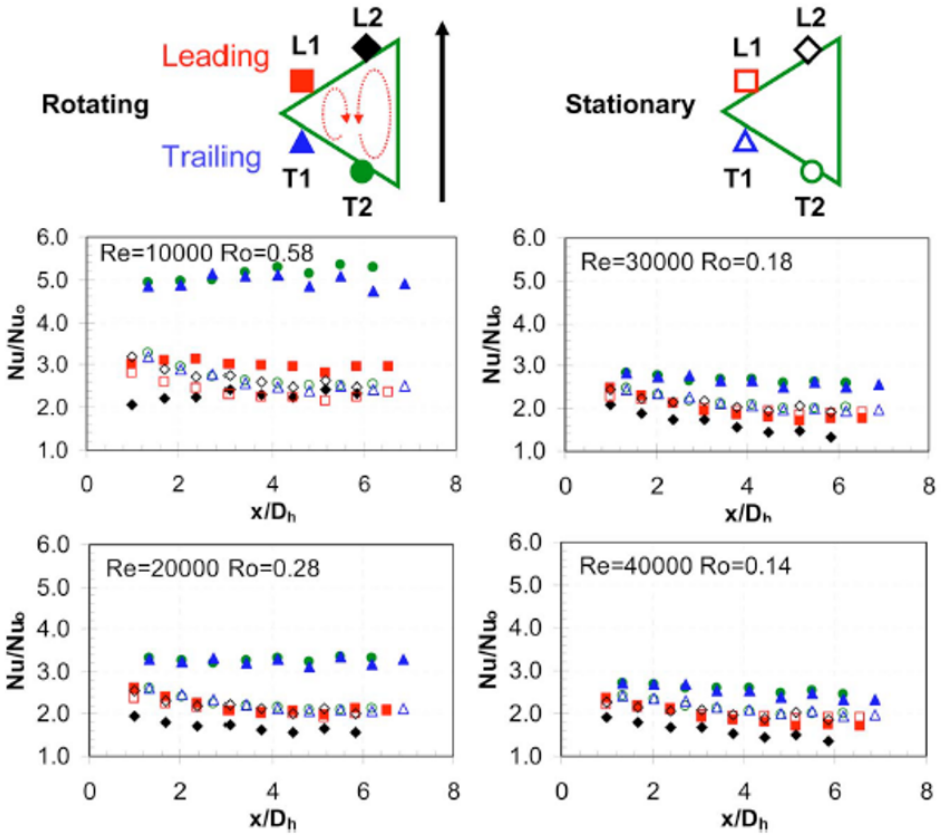


*Figure 2.9: Heat transfer coefficient distribution for the smooth channel from Liu et al. [12]*

effect allowing to impose a determined heat flux, while the thermocouples allow to measure the copper plate internal surface temperature. The flow temperature is measured at the inlet and at the outlet of the test section and then computed along the channel radial extension by interpolation. Resolving the equation of stationary convective heat transfer it is possible to determine the average heat transfer coefficient on every copper plate, hence determining a rough distribution through the cooling channel with a spatial resolution equal to the number of copper plates. This experimental technique is extremely effective in determining the performance of a cooling channel, and allowed the gathering of the dataset on a wide test matrix with several combinations of flow conditions, turbulence promoters configuration and channel orientation.
In regards of the leading edge investigations, the results reported in figure 2.9 showed the distribution of the Nusselt number in a smooth triangular channel for several rotation numbers. The results showed an increase of the heat transfer on the trailing side (T1, T2), which is enhanced for increasing Ro. On the leading side, the behavior depends on the region and does not have a linear trend with Ro.
Investigations presented in Liu et al. [12] and [1], despite being completely exhaustive from

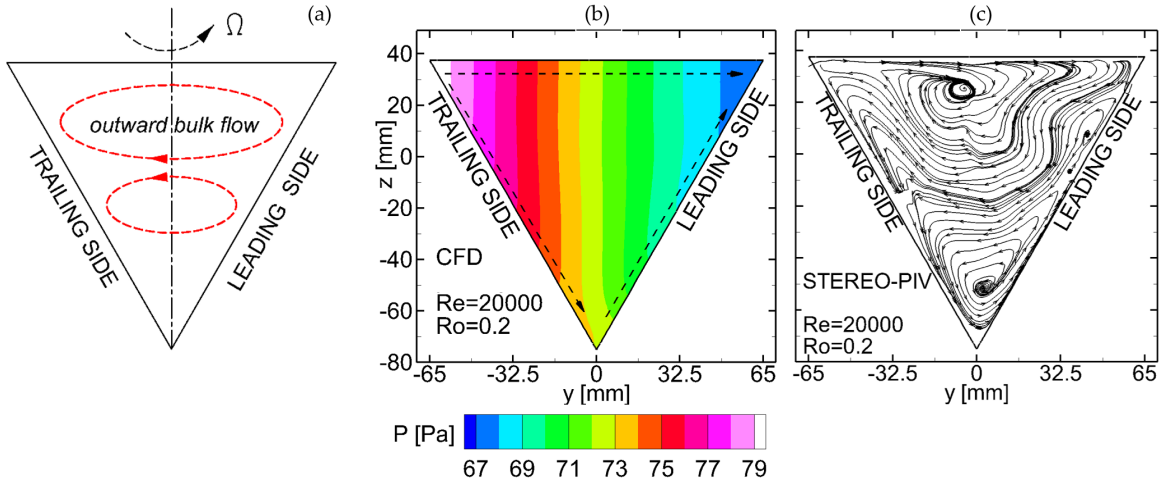


*Figure 2.10: Triangular equilateral cross sectional channel: (a) stereotyped Coriolis induced vortices, (b) pressure gradient (c) Coriolis induced vortices from Pascotto et al.[13]*

the heat transfer point of view, lack the information on the flow field needed to understand the thermal behavior. In fact, the secondary flow structures induced by the Coriolis' force are described with the simplified model presented in figure 2.10 (a). This model is drawn straightforward from the available literature on rotating square channels, and preserves its characteristics traits, like the presence of reattachment and separation zones in the middle of the trailing and leading sides respectively. In the work of Pascotto et al. [13], the flow field inside a scaled-up version of the geometry studied in [12] was investigated by means of PIV (hence the necessity to increase the model size) and CFD. The work exploited the capabilities of Ansys CFX after validating the

numerical model with experimental measurements by means of S-PIV in the facility described in Armellini et al.[14].
They showed the strong influence of the cross section geometry on the secondary flow structure. Despite how trivial this statement could sound, in the present day the secondary flow structures inside rotating channels are still modelled blindly transposing the knowledge acquired with years of study of the squared channels, as shown in figure 2.10 (a). However, as it can be seen in figure 2.10 (c), the work of Pascotto et al. [13] showed that the reattachment/separation regions do not occur on the trailing/leading sides as in the square channel, but on the trailing/leading apices, according to near wall flow driven by the pressure gradient as shown in figure 2.10 (b).
The flow field was also investigated for higher rotation numbers. The data showed the formation of a single counter rotating vortex cell instead of the symmetrical couple that occurs in the squared channel. Moreover, the increase of Ro determined a hastening of the secondary flow structures evolution along the channel axis, with the flow field pulsating between two main secondary flow structures configurations.
Despite being the available literature on simplified straight channels with triangular equilateral

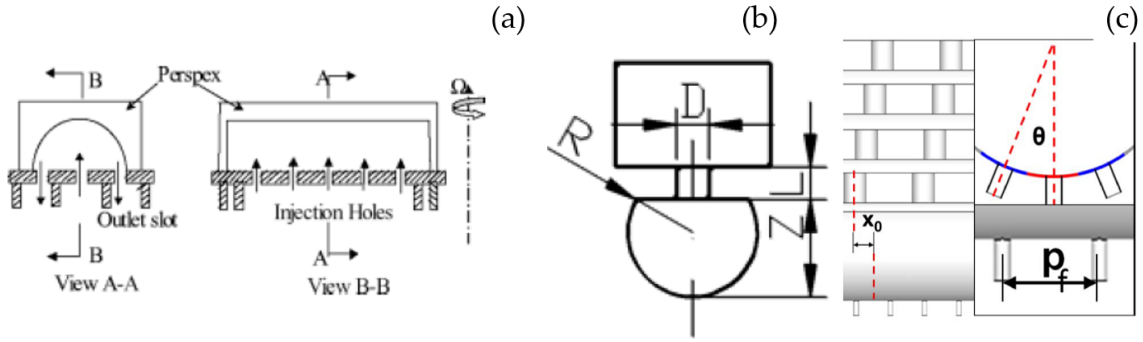


*Figure 2.11: Geometry investigated by Iacovides et al. [15] (a) and Yang et al. [16] (b-c)*

cross-section extremely detailed, it cannot provide a complete characterization of the leading edge cooling systems. Indeed, as discussed in the previous paragraphs, the leading edge region is subjected to very high thermal loads, hence the combination of cooling techniques such as film cooling and jet impingement are largely employed in this blade region.
Research on leading edge cooling systems has indeed been focusing on advanced geometries with impingement cooling and a combination of the former with coolant extraction devoted to the film cooling of the external surface of the blade. The contributions range from simplified geometries to detailed models where most of the real features (e.g. jet fillet) are reproduces.
Concerning simplified geometries, the work of Iacovides et al. [15] is devoted to the experimental analysis by means of Liquid Crystal Thermography of the flow field inside an impingement channel under rotating conditions. Flow visualizations obtained with PIV and LDV are also

presented in order to explain the thermal behavior. The test section is shown in figure 2.11 (a) and represents a row of jet impinging on a simple curved surface (i.e. semi cylindrical), where the flow, after the impact and a 180° turn is extracted at the peripheral region. The results showed that rotation determine a decrease in the heat transfer as well as some of the peaks caused by the jets impact on the surface. The explanation given is that rotation causes a greater jet velocity spread rate with respect the static case.

Another study on a similar geometry performed by Yang et al. [16] investigated the effect of

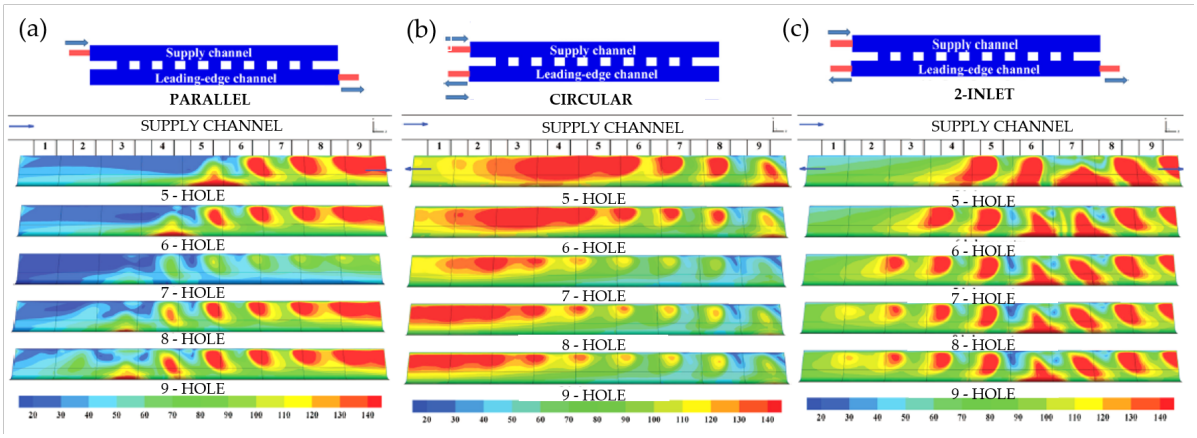


*Figure 2.12: Nusselt number distributions for the geometries tested by Elebiary and Taslim [17]*

coolant extraction from the impinging channel. In particular this work deepen the comprehension of the effect on heat transfer of cooling holes with respect the jets. The geometry, shown in figure 2.11 (b), differs from the one investigated by Iacovides et al. [15] for the jet feeding condition. In fact, in this case a more realistic crossflow condition is realized in the feeding channel. The results of the experimental and numerical campaign showed a major influence of the film cooling holes arrangement (figure 2.11 (c)) on both velocity and thermal fields.

In the work of Elebiary and Taslim [17], a geometry with a more realistic cross section (isosceles

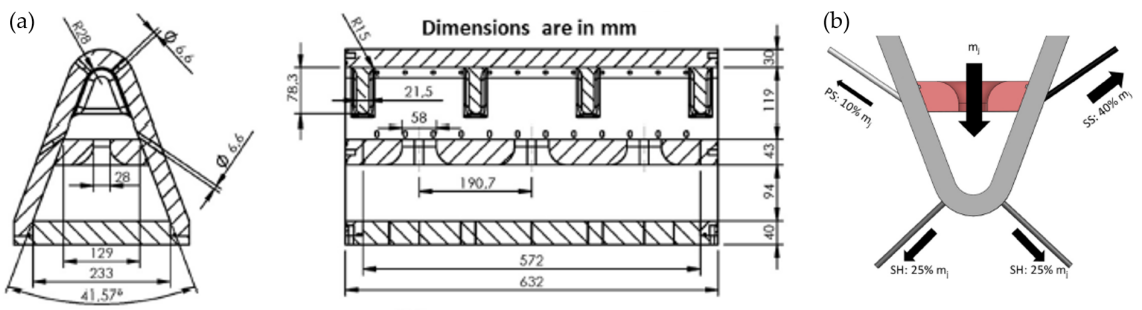


*Figure 2.13: Nusselt number distributions for the geometries tested by Andrei et al.[18]*

triangle with a rounded vertices) was studied by means of numerical simulations and thermal measurements with thermocouples (i.e. as done by Liu et al.[12]). The key features of this geometry where the racetrack jet holes and the different crossflow conditions imposed in the impingement channel, as shown in figure 2.12. The campaign investigated the effect of number of impinging jets on the heat transfer and concluded that crossflow has a major impact on the heat transfer, with the circular condition (figure 2.12 (b)) being the most effective.
Concerning realistic geometries, in the work of Andrei et al. [18] the test section investigated is an extremely detailed reproduction of a real engine leading edge cooling system with jet impingement and film cooling extraction holes, as it can be appreciated in figure 2.13. In particular, jet holes have a race-track cross section and a large fillet on the inlet section and coolant impinges in a channel where each jet is confined by two large fins, that prevent jet interaction.
The work of Andrei et al. [18] investigated the heat transfer behavior by means of the transient liquid crystal technique. They mainly studied the effect of different cross-flow conditions in the feeding channel for several jet Reynolds number and a non-symmetrical mass flow extraction distribution among the film cooling holes.

## 2.3 Motivation of the present work

The increasingly higher cooling performances demanded to leading edge cooling systems request an accurate design of channels geometries in order to meet the cooling targets (i.e. heat removal and heat transfer uniformity with limited coolant mass flow rate).
The highly detailed investigations on simple channels heat transfer behavior, however, is not supported by an equally detailed and vast presence of works that investigate the aerodynamic behavior. As discussed in the former paragraphs, rotation induced effects are extremely complex and as shown in Pascotto et al. [13], the transposition from square to triangular channel is not straightforward.
Moreover, when buoyancy and turbulators induced effects are introduced, the flow field behavior complexity further increases as shown by Coletti et al. [10]. Since the Coriolis induced secondary flow structures are substantially different in triangular channels with respect the ones in the rectangular, a different behavior can also be expected for the recirculating structures induced by the turbulators.
For first stage rotor blades, however, complex cooling schemes with impingement cooling and extraction holes have to be employed. The works available in the open literature do not consider rotation effects, and in the rare cases they do, the geometry investigated is far too simplified.
On the other hand, computation fluid dynamics has become an essential tool for the industries, however since DNS large scale applicability still demands extremely high computational costs in both time and resources, RANS and LES have to be used. The latter, in order to provide reliable results, have be validated on experimental data. For this reason, complex geometries have to be

tested in engine like conditions with variable and realistic boundary conditions.

This work is basically divided in two main campaigns, one on a simple triangular geometry and another on a more advanced jet impingement cooling system. The first one is the extension of the campaign on the smooth channel performed by Pascotto et al. [13] (and the author as undergraduate), where the effect of turbulence promoters and buoyancy on the flow field have been investigated. This work aims to provide useful information on the buoyancy effects and on the behavior of the flow field in a simple triangular geometry. Moreover, this geometry has already been studied by Liu et al. [1], as far as the thermal point of view is concerned and a wide database for several working conditions is available. The aerodynamic measures performed in this work will help to give a better insight on the thermal data.
The design of the test section for the ribbed channel investigation is a result of a compromise between the necessity to heat the walls in order to simulate real engine working conditions, and the optical access required for the PIV. As a result, only in a limited region was possible to perform PIV measurements. The analysis of the data showed a very complex behavior of the flow field, which was not possible to characterize in its completeness. In order to deepen the analysis, the experimental data were exploited to validate the computational code used for the simulations. With the latter investigation it had been possible to characterize the flow evolution along the channel, as well as the behavior of the recirculating structure between the turbulence promoters throughout the entire lateral wall.

The second part is dedicated to the characterization of the flow field inside a leading edge cooling system with impingement and extraction holes, with several mass flow rates split configurations. The test section is also characterized by several features that increase the fidelity of reproduction of a real geometry, such as: jet holes shaped as racetracks with fillet on the inlet section, rounded apex (leading edge) and many others. However, the most interesting aspect of this experimental campaign, is the imposition of complex boundary conditions. In particular, the mass flow rate extracted from the film cooling holes is different depending on the zone they are situated in (i.e. pressure side, suction side or shower head). Another variable considered has been the cross-flow over the jets. In fact, depending on the position along the blade height, jets experience a different inlet condition. Thanks to the particular design of the test article, it had been possible to perform measurements for different conditions that allowed to completely understand the flow behavior in both the feeding channel and the jets. A detailed description of the design of a test rig that allows such flexibility also is provided.

# Part II

# EXPERIMENTAL METHODOLOGY

CHAPTER 3

# PARTICLE IMAGE VELOCIMETRY

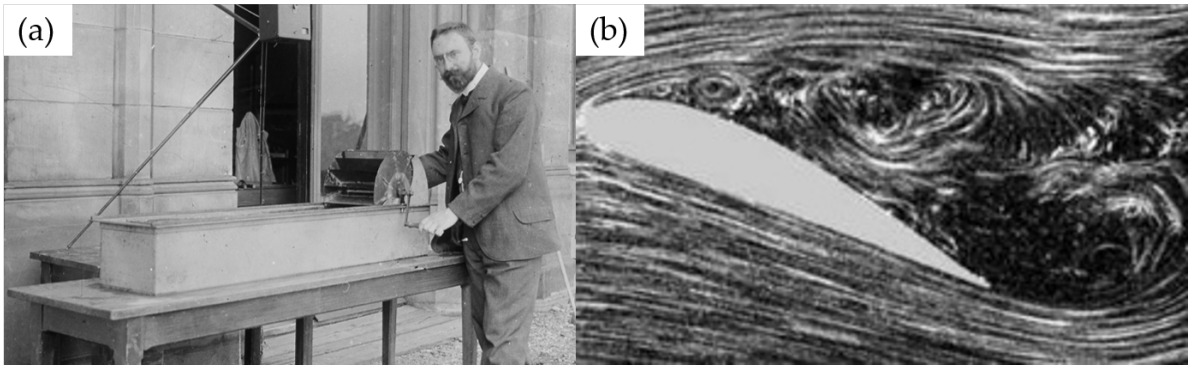


*Figure 3.1: Prandtl near the machine (a) designed to obtain flow visualization such as the one shown in subfigure (b)*

Most of the progress made in fluid dynamics had been made thanks to direct observations of various phenomena. Starting from Leonardo da Vinci and his study on vortical movements of water in rivers, Osborne Reynolds and the visualization of laminar and turbulent flow conditions with dye in water and finally Prandtl with the planar visualization of flow around objects such as cylinders and airfoils with water and silver particles (figure 3.1). Those useful methods, however, fall under the definition of "flow visualization ", which etymologically and practically are qualitative methods. Indeed they allow to deepen the understanding of complex phenomena (such as turbulence), but cannot provide data that can be used for design. The strive for knowledge and information, pushed for the invention of increasingly complex measurement methods, from the Pitot probe, to the five hole probe, which allow to measure local velocity, Laser Doppler Velocimetry (LDV) among many others, and finally particle image velocimetry, that could be seen

as the descendant of the Prandtl method.
Particle image velocimetry (PIV) is an optical (i.e. non-intrusive) experimental method that allows to obtain both quantitative and qualitative data on the flow field on an extended portion of space at the same time. More in detail, the basic 2D-PIV allows to measure the two perpendicular velocity components on a plane defined by a thin laser sheet. In order to measure all three velocity components (two in-plane plus the out of plane velocity component) on a plane, Stereo PIV (i.e. 3C-2D PIV) has been developed, while further improvements in computational tools and instrumentation allowed to develop Tomographic PIV, where the three dimensional flow field can be measured inside a volume.

## 3.1 Principles

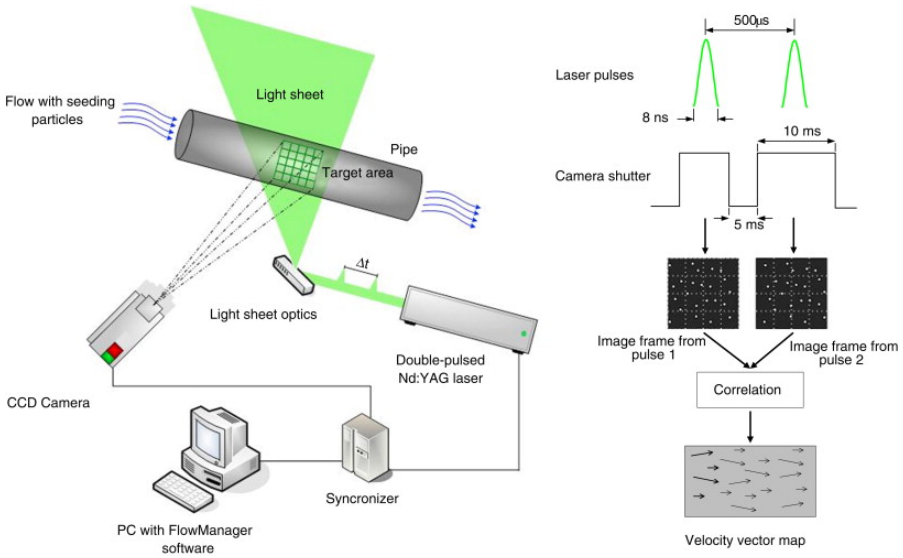


*Figure 3.2: Particle Image Velocimetry: from laser and particles to velocity data*

The experimental technique, which is showed in figure 3.2, is based on a rather simple idea: retrieve the invisible velocity components of the flow field of a fluid through the visible motion of small particles (i.e. seeding) dispersed in it. In order to obtain the measurement, particle are illuminated by a laser sheet that also determines the measurement plane. Two images of the flow field are taken with a camera at a short distance of time and the position of the particles (i.e. the light scattered by the particles recorded by the camera) in the two images is compared. The images are divided in interrogation windows (i.w.) that determine the spatial resolution of the measurement, since the movement of the particles inside each i.w. between the two images gives a displacement vector in the time elapsed, hence the velocity field. The displacement, being computed in the image space, is obtained in pixels but it can be converted in real space units

(meters) through the magnification factor (M [px/m] or [px/mm]).
The main characteristic elements of this experimental technique are the particles used to inseminate the flow, called seeding, the light source, i.e. the laser, the camera and finally the image processing. In the following each element will be described, with emphasis on the critical aspects concerning it. The PIV methodology is an indirect measurement of the flow velocity since the actual velocity measured is the particle ones. For this reason, fluid mechanical properties of the particles have to be examined in order to avoid significant discrepancies between fluid and particle motion.
A primary source of error is the influence of gravitational force if particle and fluid densities are much different, however for most of PIV application it can be neglected.
On the other hand, it is worth analyzing the velocity lag between particle and fluid. Considering a spherical particle moving in an always accelerated flow with constant acceleration at very low Reynolds number, the velocity lag ($U_{LAG}$) is expressed by the following equation:

$$U_{LAG} = U_p - U_f = d_p^2 \frac{(\rho_p - \rho_f))}{18\mu} a \tag{3.1}$$

If the density of the particle is much higher than the fluid density, the response of the particle velocity to a step change in fluid velocity follows an exponential law:

$$U_p(t) = U_f[1 - (\frac{t}{\tau_s})] \tag{3.2}$$

Where the reference time scale ts is:

$$\tau_s = d_p^2 \frac{\rho_p}{18\mu} \sim \frac{d_p^2}{\nu_p} \tag{3.3}$$

Despite the usual operating conditions involve variable acceleration and high Reynolds numbers, hence the equation of motion is far more complex and the solution is no longer an exponential, the relaxation time ts remains a convenient estimation of the particle tendency to chase velocity equilibrium with the fluid. The definition of $\tau_s$, suggests that in order to reduce the lag between particle and fluid velocity, particle diameter should be as small as possible. However, the diameter should not be lower than 1 $\mu m$ since particle dimension has a strong impact on the light scattering properties, as it will be explained in the following.
The choice of particle diameter is therefore a compromise between inertial properties and lighting requirements for a good measurement. It has also to be taken into account that in the processing procedure the velocity of the particles inside an i.w. is averaged together as it will be showed in the following, hence extremely low particle diameters (< 1 $\mu m$) should be used only if a very high spatial resolution is needed. A common example where this situation might apply is to investigate a shockwave extension.

A proper illumination of the particles is mandatory in order to ease the processing procedure. This phenomenon, for spherical particles with diameters $d_p$ larger than the incident light wavelength lambda the Mie's scattering theory can be applied.

In figure 3.3 the normalized scattered intensity of different diameter glass particles in water according to the Mie theory are shown at $\lambda = 532nm$. As it can be seen, the light is not blocked by the small particles but it is spread in all directions. Therefore, in a highly seeded flow, particle illumination does not comes only from the direct source (i.e. the laser) but also from the light diffused by the other particles. For this reason, in heavily seeded flows, the overall illumination of the image is higher than what it would be for a single particle illuminated by the same light source. In fact, increase the quantity of seeding in the flow is a strategy to overcome light limitation in an economical way. However, there is one major limitation for this strategy: the increase in background noise. Therefore the noise in the acquired images that affects the processing procedure accuracy.

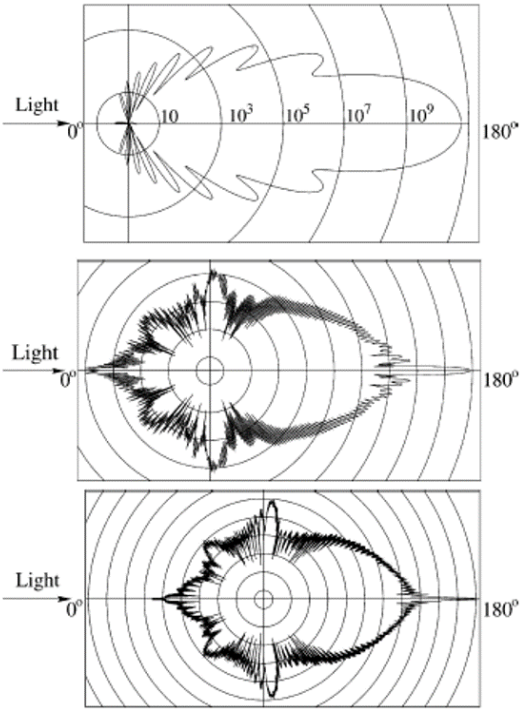


*Figure 3.3: Light scattered by 1$\mu m$(a), 10$\mu m$ (b) and 30$\mu m$ (c) glass particles in water (Mie's scattering)*

The necessary illumination is provided by lasers that have the fundamental characteristic of being coherent both in time (i.e. narrow spectrum) and in space (i.e. remains collimated over long distances). Moreover the laser can be generated as a very short impulse, allowing extremely reduced exposures times.

The beam is generated in a cavity where a gain medium is excited by a power source. Usually the light pulse has a wavelength of 1064 nm and its harmonics, however for safety reasons it is bandpass filtered to isolate the harmonic at 532 nm (i.e. green light, the only visible). The beam passes through a cylindrical lens that converts the beam into a line and then a spherical lens that compresses the light into a thin laser sheet.

Lasers can be operated in mainly two ways, i.e. continuous and pulsated light emission. The former is usually employed for time-resolved (high-speed) PIV, while the latter is employed for standard PIV. In particular, for the case of pulsated light emission, PIV lasers are operated with the technique of Q-switching, that allows to produce pulses with a high peak power (i.e. more illumination). The image couples acquisition is performed with high sensitivity digital cameras.

PIV dedicated cameras have cooled CCD, in order to reduce noise. In the past, cameras had not sufficiently short exposure times, hence it was impossible to acquire the image couples with typical PIV separation times. This problem meant that multiple exposure images were acquired, where both frames laid on a single image. The major problem was the determination of the displacement direction that could not be uniquely determined. Nowadays, digital cameras are capable of acquiring frames with separation times of the order of micro seconds with different acquisition rates. Moreover, beside standard PIV cameras with acquisition rates of the image couples of the order of the hertz, there are fast cameras that allow to reach acquisition rates of the order of $10^4$ $Hz$. The former allows only statistical flow quantities to be analyzed (e.g. mean velocity components, mean velocity fluctuations etc. . . ) while the latter, coupled with lasers operated with continous light emission, allows time resolved investigations of flow features. In this case, however, the images are acquired as a single sequence and the two frames are defined as consequential images.

## 3.2 Image processing

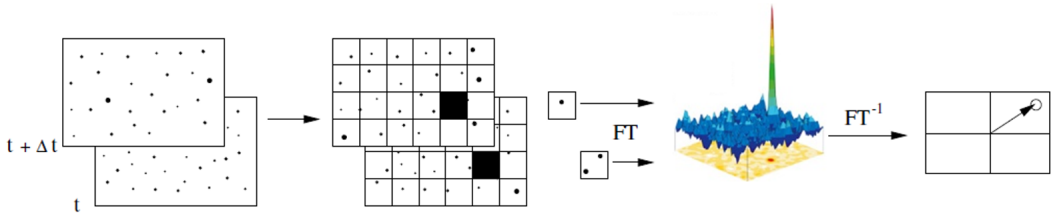


*Figure 3.4: Displacement determination and cross-correlation plane*

The flow field is retrieved from the comparison of the particle positions in the two images. This comparison is not finalized at the determination of the displacement of each particle, but the most statistically probable (i.e. representative) displacement of groups of particles. The following discussion will treat only single exposure image couples, where the first one will be referred to as frame A, and the second one as frame B.

The images are divided in a grid of interrogation windows (i.w.) that define the final measurement spatial resolution. The interrogation windows dimension depends mainly on the magnification factor and the particles dimension. For typical PIV setups with M varying between 5 and 25 px/mm and particle dimension between 1 and 10$\mu$ m the usual interrogation window dimension is 32× 32 pixel.

Each interrogation window in one image is compared with the respective in the other, and the most probable displacement of the particles inside the i.w. is determined. The images can be seen as a function $\Re^2 \rightarrow \Re$ where at each pixel corresponds a light intensity level depending on the camera resolution (e.g. 12 bits equals to a 0-4095 levels range).

In order to compute the most probable particle displacement a cross correlation between the i.w. of frame A and a region larger than the i.w. in frame B is applied, seeking the displacement of the i.w. of frame A that maximizes the cross-correlation peak. Thanks to the correlation theorem, that states the equivalence between the cross correlation of two functions and the complex conjugate multiplication of their Fourier transforms, it is possible to exploit modern computer computation capabilities. In fact, compared to $O[N^4]$ for the direct computation of the two-dimensional correlation the process is reduced to $O[N^2 log_2 N]$ operations, hence reducing the require computational time.
The use of FFT has a number of properties that leads to some effects that have to be dealt with. In particular the FFT works efficiently with data whose dimension can be represented in base-2, meaning that the i.w. dimension has to be in base 2 (e.g. $16 \times 16$ $pixel$, $32 \times 32$ $pixel$, etc...). Moreover the data is assumed to be periodical, therefore if the particle displacement exceeds $\pm N/2$ (where N is the i.w. dimension), would not be correctly detected being affected by the aliasing. The practical displacement constraint, however, is much higher due to the fact that the signal strength of the correlation peak will decrease with increasing displacements, due to the proportional decrease in possible particle matches. The reason is rather simple: the higher the displacement, the higher is the number of particle that leave the region of space defined by the i.w., hence fewer particle match can be found. Earlier literature reports a value of N/3 to be an adequate limit for the recoverability of the displacement vector [19]. A more conservative, but widely adopted limit is N/4, sometimes referred to as the one-quarter rule [20].

### 3.2.1 Advanced digital interrogation techniques

Starting from the basic description reported in the previous paragraph, several interrogation techniques have been developed:

- multiple pass interrogation schemes with integer sampling window offset [21] and [22].
- coarse-to-fine interrogation schemes (resolution pyramid [23][24]) or (flow-)adaptive resolution schemes
- second-order schemes relying on the deformation of the interrogation samples according to the local velocity gradient [25]

All these variations are based on a predictor-corrector iterative process, allowing to progressively reducing the number of non-valid vectors (i.e. when the cross correlation fails) by increasing the cross correlation peak. The philosophy is to use a first step to determine a rough displacement field that will be used to offset each i.w. pursuing the particles. In coarse to fine interrogation schemes the window dimension is also progressively reduced to increase the resolution. Second order schemes take into account flow gradients (i.e. velocity difference between close i.w.) to apply deformation of the windows in the second step.

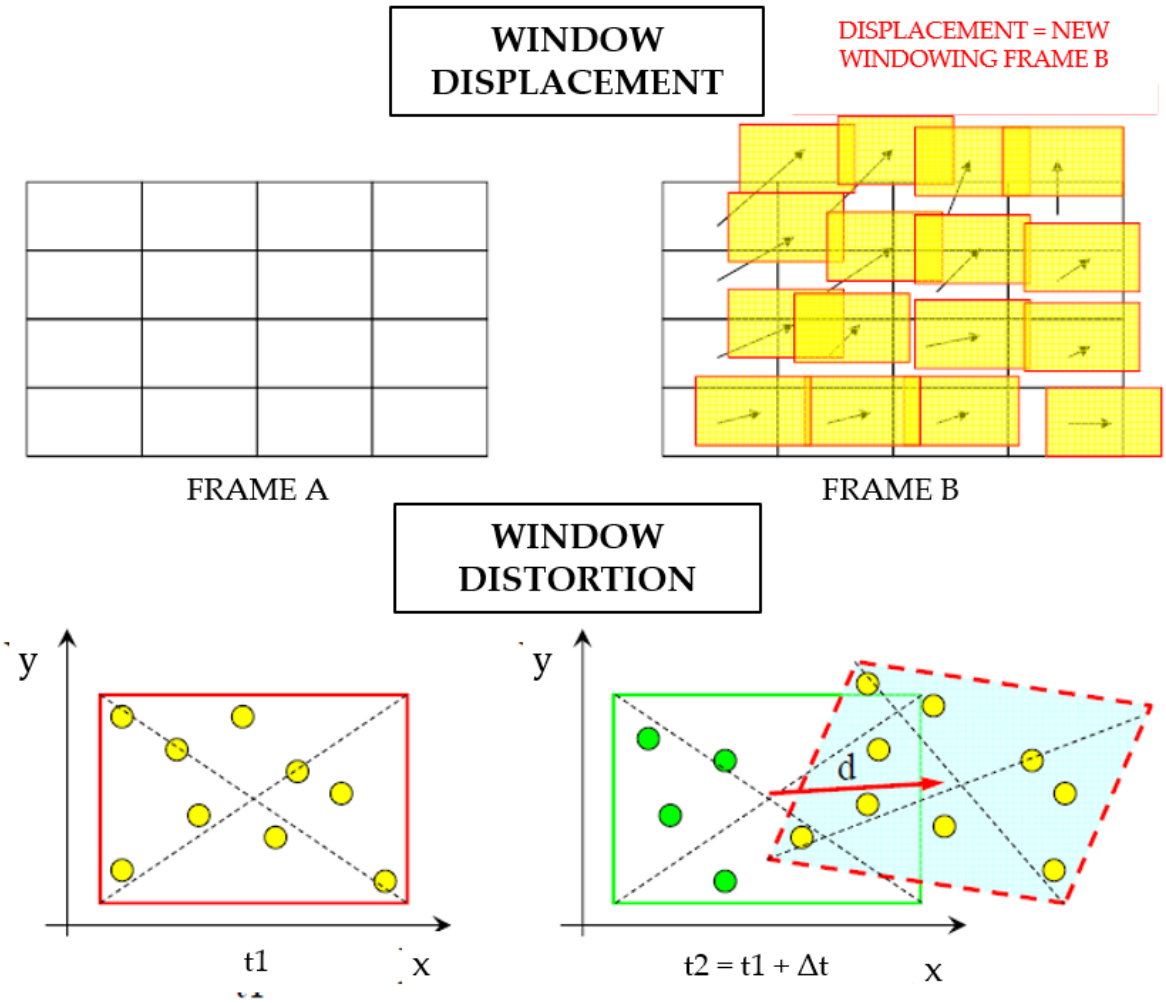


*Figure 3.5: Combination of offset and coarse to fine multipass interrogation grids*

The first two strategies in particular are also coupled together, in fact the first coarse step is used to determine an offset, then the grid is refined and the i.w. displaced accordingly.

## 3.3 Stereoscopic PIV

The limit of application of the 2D PIV, concerns the flow field characteristics. In fact, in a 2D-PIV setup, the measurement plane should be containing the main velocity components. If a strong out-of-plane component is present, indeed, the measurement is affected by the parallax error (that will be discussed concerning the measurements under rotating conditions in chapter 4.1.1). Since most investigated geometries in the application field of blade cooling are characterized by three-dimensional flow fields, the 2D PIV approach does not allow to retrieve complete information.

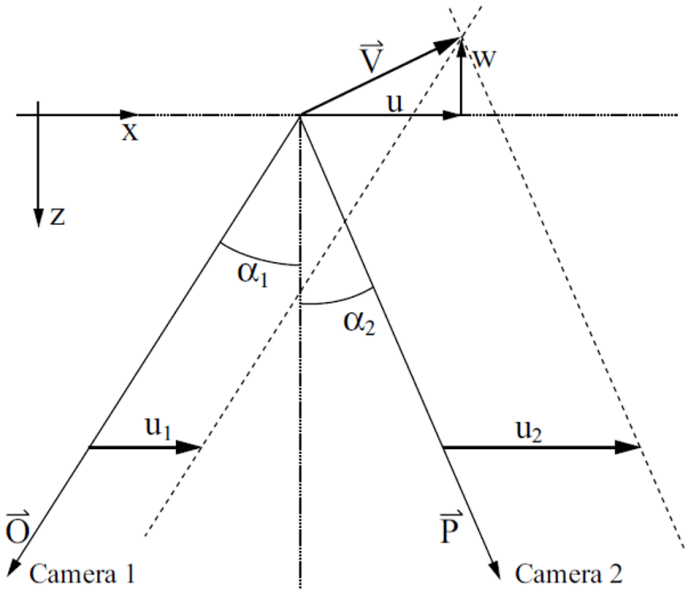


*Figure 3.6: Three components velocity reconstruction through stereo vision*

For these reasons, stereoscopic systems have been developed. Mimicking the human binocular view, two cameras frame the same region of space and acquire an image couple each at the same time. Thanks to geometrical relations of perspective, starting from the two bi-dimensional displacement fields it is possible to reconstruct the three velocity components as depicted in figure 3.6.

Two stereoscopic configurations exist: translational systems and rotational systems, as shown by figures 3.7 (a) and (b). In the former, the lenses plane and the cameras optical axes are respective parallel and orthogonal to the object plane while in the latter camera axes are not parallel and intersect in the object plane. The primary advantage of the translational method is its simplicity: in fact, the magnification factor throughout the image plane is constant, hence no image dewarping is required. However, the main drawbacks comprehend a limited common area imaged by the cameras and a limited off axis angle. This latter determines a low accuracy on the out of plane component [26][27], hence a less diffusion of this technique in favour of the angular displacement system. The rotational system, on the other hand, guarantees a much higher accuracy on the out-of-plane component but comes with a more complex setup. In fact, due to the inclination of the camera axes the focus area is small with respect the camera field of view and the magnification factor is not constant over the field of view of each camera. In order to overcome the first issue, the image plane (i.e. the CCD) has to be tilted in order to achieve the Scheimpflug condition (i.e. image, lens and object planes are collinear). The second issue, which results in perspective distortion, demands a proper image manipulation (i.e. dewarping) before combining the information available from the two cameras and perform the so called stereo

reconstruction.

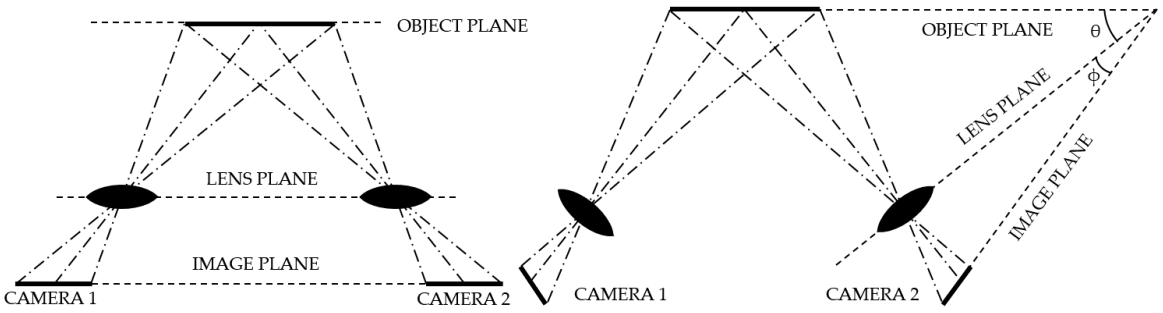


*Figure 3.7: Lens translation method (a) and angular lens displacement with tilted back plane (b)*

### 3.3.1 Stereo reconstruction

The reconstruction procedure combines the displacement measured by each camera in order to obtain the three components of velocity onto the object plane. The reconstruction can be performed in two ways:

- geometric
- calibration based

The former requires the geometry of the recording configuration to be completely known (i.e. distances between object plane and CCDs, angles etc. . . ) in order to be mathematically modelled. However, this latter may not be possible due to the presence of non-linearities such as lenses distortion. For these reasons (unrealistic precision required to the knowledge of the geometrical configuration and non-linearities) the geometric method is rarely employed.
Calibration-based reconstruction may be further classified into 2-D or 3-D calibration methods. In the former, a mapping function is determined to relate each of the two 2D image planes to the 2D object plane. The optical configuration parameters are still necessary to compute 3D displacement field starting from the two 2D camera ones. The latter method, instead, provides a direct relationship between the particle location in a 3D space with its position on each of the image planes, therefore any knowledge about the optical set-up is no longer needed.

### 3.3.2 Stereo calibration procedure

In both approaches, the calibration procedure remains rather similar. Calibrations require multiple images of a target placed in correspondence of the object plane (i.e. laser sheet) and

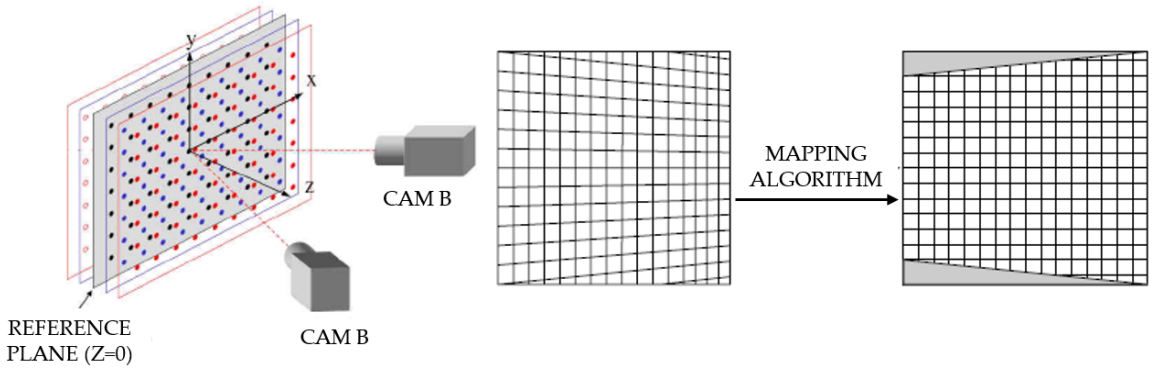


*Figure 3.8: Calibration procedure (a) and image dewarping (b)*

displaced in the off plane direction (z axis in figure 3.8) in many other positions. The target has a regular patter of markers that allow to cross correlate their positions in the images and obtain the image mapping. Briefly, 2D calibration methods require to obtain the calibration data necessary to relate each of the two cameras image plane with the object plane and then to determine the mapping function to perform image dewarping. Once the target is removed and the data acquisition is performed, the raw images are dewarped and cross correlated on a cartesian grid in the image plane as shown in figure 3.8. Then the same mapping function is used to project the two displacement fields over the object plane, where they are further interpolated to a common grid. It is important to note that the calibration data is used also to compute the optical configuration parameters which are still necessary to perform stereo reconstruction.
In contrast to 2D calibration, the 3D approach, followed by [28], does not require the detailed knowledge of the system geometry at any stage. The off plane exposures are used to retrieve the relationship between the three dimensional position on the object plane and the two 2D dimensional image fields. If the 3D reconstruction is more simple than the approach followed by Willert [24], the drawbacks of the methodology proposed by Soloff et al. [28] are a more complex algorithm of the cross correlation procedure and the impossibility of performing the misalignment correction. This latter is necessary to compensate the error generated by the impossibility to exactly align the calibration target with the laser sheet.

### 3.3.3 Misalignment error

In the previous paragraph it has been observed the impossibility of placing the calibration target at the exact position of the laser sheet, hence an additional source of error has to be considered: the misalignment error. In order to overcome this issue and minimize the error, [19] proposed a methodology called disparity correction. This approach relies on the fact that the images from the two cameras are back projected onto a plane that is not exactly the one where they lay, due to the misalignment error. Thus, the same particles will have different position in the two views that

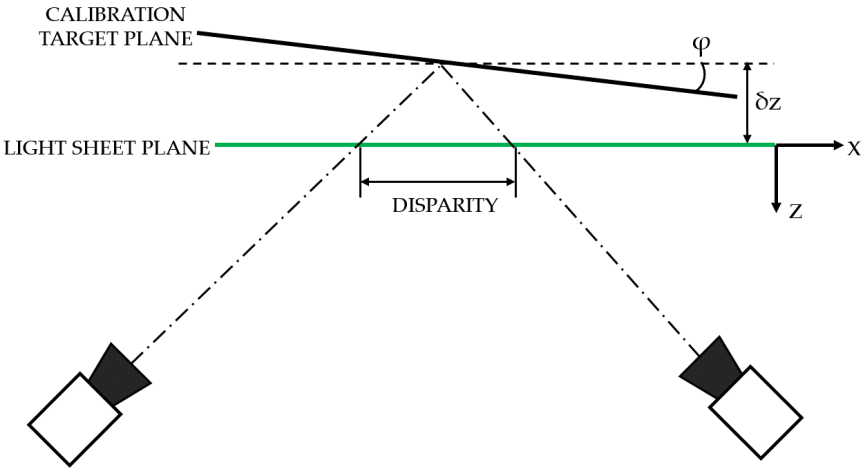


*Figure 3.9: Sketch of the misalignment error, also known as disparity*

can yield to a high bias error. However, this fact can be exploited to correct the misalignment. In an ideal condition, in fact, where there is no misalignment, the cross correlation between the first two frames from the two cameras will result in no displacement, while in a real case scenario, where misalignment is not preventable, the resulting displacement field is an indication of the misalignment indeed. Willert proposed to use this disparity map to correct the back-projection coefficients, the same approach has been followed followed by Astarita and Giordano [29]. A more sophisticated approach was proposed by Scarano et al. [30] and Wieneke [31] where the disparity map was used not only to correct the image de-warping by also the viewing angles.

## 3.4 PIV system at the University of Udine

The PIV system of the Turbomachinery Laboratory at the University of Udine is custom made and it has been developed throughout the years to support the continuously increasing demands for cooling channels research. In particular the PIV system allows to perform both 2D and S-PIV measurements in static and rotating channels, thanks to the procedure explained in chapter 4.1 and the facility described in chapter 5 The main hardware components are:

- two high sensitivity *PCO-Sensicam* cameras with cooled CCD of 1024x1280 pixels (i.e 1 Mpx) of resolution
- *Litron Nd-YAG* pulsated laser, 120$\mu J$ of peak power
- *New Wave Nd:YAG* pulsated laser, 60$\mu J$ of peak power
- *PIVTEC* sequencer, for camera-laser synchronization
- *Laskin* nozzle for seeding generation (average particle size of 1.2$\mu m$)

- two set of low distortion *NIKKOR* lenses with fixed focal length of 35mm, 60mm and 105mm
- two custom made Scheimpflugs
- *NI-6601* four counter board, with 20MHz timebase for phased-locked measurements synchronization
- photodyode, for phased-locked measurements synchronization and rotational speed measurement

The precise purpose of the last two items will be explained in chapter 4.1.
The cameras are connected to the control PC with optical fibres, in order to allow fast transfer of the acquired images. The cameras cannot be used for fast acquisition (i.e the acquisition frequency is 4 Hz), allowing to investigate statistical flow field properties, from the ensemble average of al large number of samples acquired (the typical number is a thousand).

## 3.5 PIV image processing in the present work

In the two experimental campaigns that will be described in chapters 6 and IV, the data presented, either velocity or their statistics, are the result of the ensemble average of 1000 samples, acquired with a frequency of 4 Hz for the static measurements and a frequency dependent on the test section rotational speed for the rotating tests. The latter constraint will be clarified in chapter 4.1.
For both 2D and Stereo-PIV data, the commercial software **PIVview** (from **PIVTEC GmbH**) was used to perform the processing of the image pairs. In particular, for Stereo-PIV data, image back-projection and then stereo reconstruction were computed; furthermore, a disparity correction was also used in order to minimize the misalignment errors ([24]).
Images were processed with a first interrogation window of $64 \times 64$ $pixels$, a single step of window size refinement to the final dimension of 32× 32 pixels and 50% of window overlapping. Two steps of window distortion-displacement were used for each step of the refinement procedure. Finally, a Gaussian peak-fitting was adopted to perform the sub-pixel interpolation. Vector validation was performed with tests based on a normalized median filter and on criteria of primary to secondary correlation peak and minimum signal-to-noise ratio. In order to enhance the images signal-to-noise ratio a combined subtraction and division for a common background procedure was applied. Furthermore, the boundary conditions of no-slip conditions on solid walls were imposed. For the rotating tests further dedicated pre and post procedures were needed, as it will be depicted in chapter 4.1.
For sake of completeness, since the test section analyzed in part IV is rather complex, many problems arose from the background noise in terms of light reflection due to the geometrical features (e.g. jet fillet and screws) affecting the measurements in the feeding channel. For this reason, even the adoption of not standard background computation and subtraction techniques

(i.e. specific computation has been performed on shorter image sequences instead of using the complete 1000 samples acquisition), could not avoid poor signal-to-noise ratios and non-valid vector clusters. These regions have been consequently blanked in the velocity contour maps of figures 10.5 and 10.6 that will be presented in the result discussion.

CHAPTER 4

# PIV IN ROTATING CHANNELS

Since this work is focused on the flow field investigation in rotating channels, it is worth to discuss how the PIV measurement of the relative flow field (i.e. with respect to the frame of reference fixed to the channel) can be performed and how it has been carried out in the experimental campaigns presented in the following chapters. The procedure that will be described in the following is the same described in the Ph.D. dissertation of Dott. Claudio Mucignat [32], hence for many aspects of the detailed description there will be a dedicated cross reference to it. However, the innovative aspects introduced in these experimental campaigns will be exhaustively described in the following.

The relative flow field can be measured either directly or it can be retrieved by subtraction of the peripheral velocity from the absolute flow field. In the first case, the PIV setup (i.e. camera/s and laser) is in-built with the rotating equipment and the test section while on the other one, laser and camera/s are fixed in the laboratory frame of reference.

The two configurations have both pro and cons that are dual, hence the choice that has to be made is, as in many engineering problems, a compromise. To measure the relative flow field is a great advantage in terms of post processing effort and velocity accuracy. The indirect method in fact, needs the developing of a dedicated post processing procedure in order to subtract the peripheral velocity (that has to be measured) from the absolute velocity field. Moreover the acquisition of the image couples has to be synchronized with the passage of the test section, which is not trivial due to the impossibility of guaranteeing a perfectly constant rotational speed.

Unfortunately, the direct measurement, requires that the mechanical structure of the rotating rig as well as the moving organs (electric motor, transmission) have to be designed in order to bear the weight also of the instruments (laser and camera/s) and be able to reach the rotational speed required by the experiment. Moreover, the PIV setup components have to be fixed extremely

tight in order to be stable during rotation. An additional complication comes from the laser that cannot have an auxiliary cooling module (that would be too bulky to be fixed to the rotating equipment) and those type of lasers produce impulses with lower energy respect to the lasers with cooling module. Light is a key element for the PIV measurement and limited light could mean limited measurements configurations (e.g. stereo PIV can be difficult to perform) according to the scattering patterns seen in 3.1.
The latter reasons are sufficient to encourage the study of methods to increase the accuracy of the indirect relative flow field investigation in order to close the gap with respect to the only advantage of the more technically problematic direct measurement. The approach followed in this work is therefore the indirect measurement of the relative flow field that from now on will be indicated as "phased-locked". This procedure has been developed throughout the years during the Ph.D research project of Dott. Claudio Mucignat [32] where mainly all the critical aspects had been analyzed and resolved. In the following, a brief excursus of the procedure basis will be summarized in order to ease the understanding of the advancements made during this Ph.D. research project.

## 4.1 Approach followed in the present work

The discussion reported in the previous paragraph highlights the major problem of the phased-locked measurement technique: the reliability of the data due to the several variables that can affect the resulting relative velocity field. In particular the principal sources of error are:

- Determination of the peripheral velocity, which is done indirectly with:
  - Determination of the angular speed
  - Determination of the center of rotation
- Guarantee that the acquisition of the images occurs with the test section always in the same position (average together correspondent points)
- PIV measurement chain intrinsic error

As far as the peripheral velocity is concerned, due to the high inertia of the rotating equipment, it can be assumed that the average angular speed ($\omega = 2\pi/T$) is constant throughout a single revolution. However, it cannot be assumed that it will be constant during the acquisition of the 1000 image samples, hence to each instantaneous absolute velocity field has to be subtracted the peripheral velocity computed with the respective angular speed.
The measurement of the angular speed is done by sampling a photodiode signal, which is obscured at every test section passage by a target integrated with the rotating arm. The signal produced by the photodiode is a square wave (the high phase corresponds to the passage of the target over the photodiode) that is sampled at extremely high frequency by a counter (embedded in a NI - 6601

PCI board) between two consecutive rising edges. Since the counter time base is known (20 MHz), the period, hence the angular speed, can by computed as follows:

$$\omega[rad/s] = 2\pi \frac{time\ base}{counted\ quantity} \tag{4.1}$$

Where:

$$T[s] = \frac{counted\ quantity}{time\ base} \tag{4.2}$$

A dedicated study conducted by Armellini et al. [33], showed that the subtraction of the corresponding peripheral velocity to each instantaneous absolute velocity field instead of the subtraction of the average peripheral velocity to the average absolute field allowed to further reduce the error on the velocity fluctuations fields.In order to determine the peripheral velocity of each point in the measured plane, their rotation radii has to be determined. The easiest way to achieve that is to determine the coordinates of the center of rotation, and then the pixels rotation radius can be easily computed. In order to determine the center of rotation position, a dedicated procedure

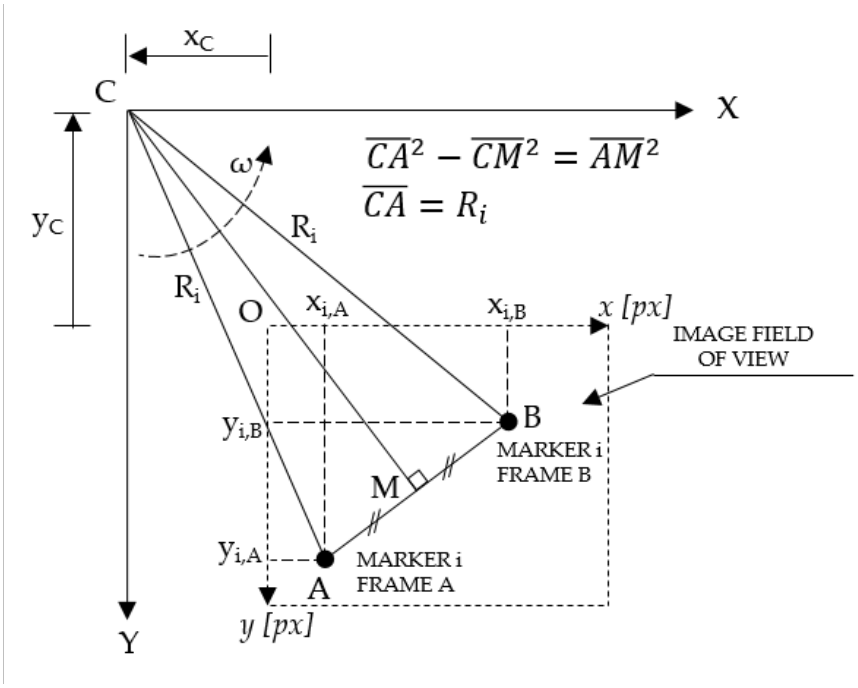


*Figure 4.1: Geometrical reconstruction of the markers translation*

has been developed by Armellini et al. [33] and refined during this Ph.D. research project. The procedure relies on the rigid body rotation without translation that links the positions of a point of the rigid body between two angular positions and the relation between absolute coordinates (camera frame of reference) and relatives one (channel frame of reference). In figure 4.1 a sketch of the considered problem is reported.

The positions of the marker and the center of rotation are linked by the following relation derived from figure 4.1:

$$x_C(x_{i,A} - x_{i,B}) + y_C(y_{i,A} - y_{i,B}) = \frac{x_{i,A}^2 - x_{i,B}^2 + y_{i,A}^2 - y_{i,B}^2}{2} \tag{4.3}$$

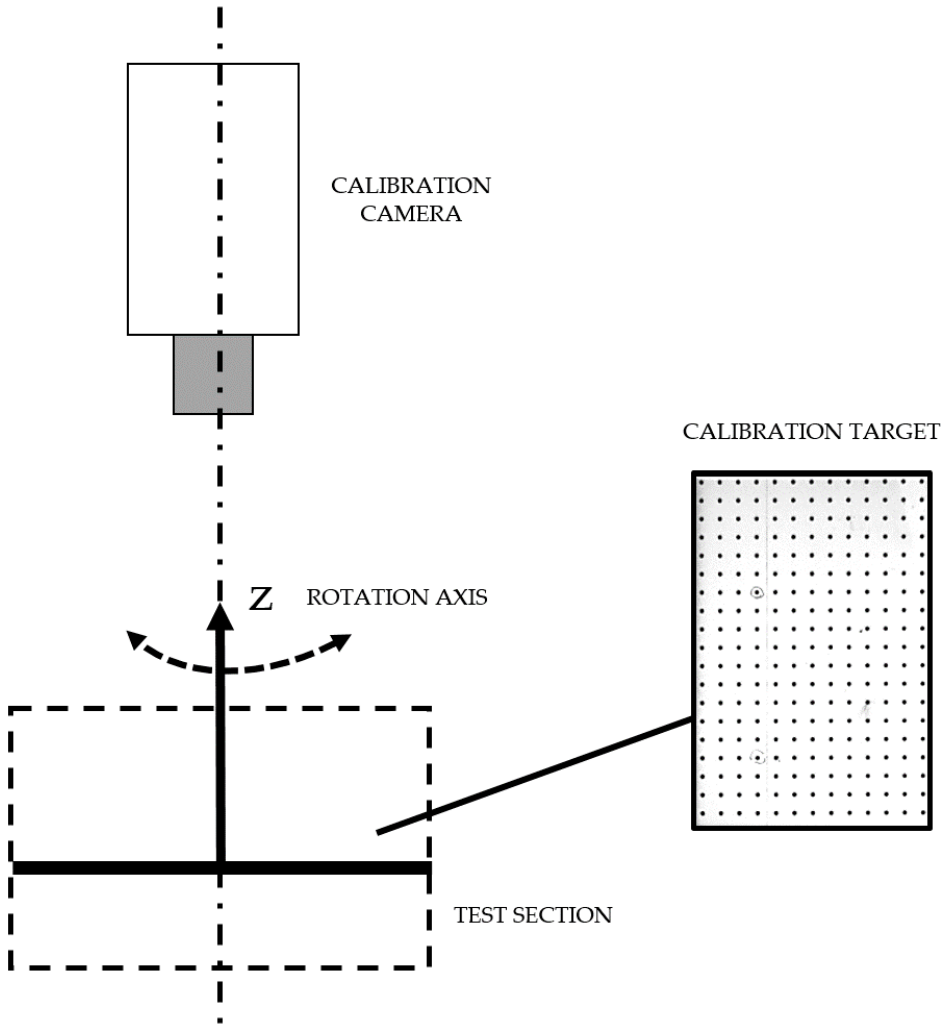


*Figure 4.2: Setup for rotation center determination. Highlighted, an example of calibration target*

In order to carry out the described procedure, the setup needs a camera with the optical axis parallel to the rotation axis (z in figure 4.2) and a target with a pattern aligned with the plane xy (see figure 4.2). The pattern can be a grid of crosses, dots or a grid of perpendicular lines, where the distance between the elements is constant. In this specific case, a target with

a dotted pattern has been used (see figure 4.2). The use of a target with such pattern allows to write the equation 4.3 for several elements couples, hence compute the center of rotation with the least squares method. In this way, the determination of the element center error can be extremely reduced, leading to the determination of the center of rotation with an error of the order of 0.1 mm that with typical radii of the order of 500 mm corresponds to a relative error of 0.02 %.

The fact that the angular velocity of the rotating arm is not constant, in addition to the demand

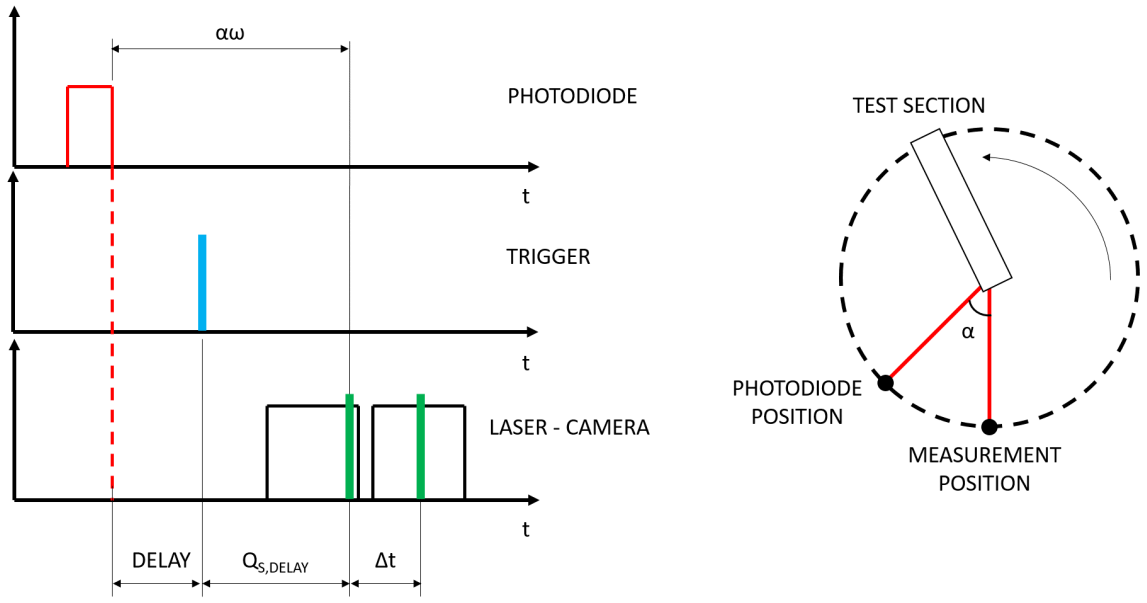


*Figure 4.3: Sketch of the problem relative to the determination of a suitable delay that allows to perform the PIV measurement with the test section always in the same position*

of measure it for each revolution, yields to an uncertainty in the measurement zone position. This non-trivial problem can be resolved by exploiting the photodiode signal. Considering the situation depicted in figure 4.3, the angular distance between the photodiode and the measurement position (i.e. position of the test section during the static measurements) is obviously fixed and can be easily determined with the help of laser reflections. This angular distance corresponds to a time delay that depends on the instantaneous (i.e. average on the revolution) angular velocity. The actual time delay that has to be taken into consideration to send the acquisition trigger to the PIV chain is the difference between this time delay and the laser intrinsic Q-switch delay according to the following equation:

$$t = \frac{\alpha}{\omega} - Q_s \tag{4.4}$$

This correlation can be better understood if the graphs reported in figure 4.3 are analyzed. They show the evolution of all the signals (photodiode, trigger, laser pulses and camera/s exposures)

with respect the time domain, which can be easily correlated to the angular position of the test section considering that angles and times are linked through the angular velocity. In order to reduce the error, the photodiode has to be positioned as close as possible to the measurement position, in order to avoid that angular velocity fluctuation within the revolution can affect the acquisition. In this simple way, it has been possible to obtain a variable time delay by defining a constant angular delay between photodiode signal rising edge and acquisition position. This method allow to reduce the acquisition position instability to the order of 0.5 mm, that is far lower with respect to the typical PIV spatial resolution, hence the derived error can be neglected.
The last source of error is probably the most difficult to overcome as well as the most critical: the PIV measurement chain intrinsic error, that, as shown in the literature [34], it can be assumed equal to 0.1 pixels. In order to better explain the way it affects the measurement accuracy, it has to be considered that in typical phased-locked applications, the peripheral velocity can be up to an order of magnitude higher than the relative flow field bulk velocity, and the ratio is even higher for the flow recirculation zones. This means that if displacements measured are of the order of 10 pixel (e=1 % on the absolute velocity field), the relative displacements can be of the order of 1 pixel, leading to a relative error e=10 %, which is unacceptable for the PIV measurement technique (considering that the final accuracy has to take into account other source of error).
This critical aspect cannot be dealt with during neither the setup nor the measurement phase, but has to be taken care of during the image processing. In the case of a plane perpendicular to the rotation axis, Mucignat [32] developed a dedicated image pre-processing procedure that involved the de-rotation of the second frame of the image couple. The procedure exploits the knowledge of the center of rotation relative position with respect to the image frame of reference, the separation time between the two frames and the average rotational speed on the revolution. Thanks to these data, it is possible to retrieve the peripheral displacement of each pixel and reconstruct a frame $B^*$ without rotation. The new image couple is then processed and the resulting displacement field is already the relative one. This procedure allow to set the PIV separation time as if it was a static measurement, hence maximizing the relative displacements magnitude(i.e. minimizing the relative error on the displacement field).
Unfortunately, the image de-rotation pre-processing can be applied only to measurement planes perpendicular to the rotation axis and in the case of 2D-PIV measurements. As far other plane orientations and S-PIV are concerned, the frame B de-rotation cannot be performed as a simple planar rotation, but it would require a complex reconstruction of the perspective view of the camera. In order to allow the setting of the same PIV separation time in both static and rotating conditions in every plane configuration, a two-step procedure has been adopted. This procedure can be applied for every PIV setup (i.e. 2D, S-PIV and plane orientation) except when the measurement plane is perpendicular to the peripheral direction (i.e. plane defined by the axes aligned with the radial direction and the rotation axis). The reason why this method cannot by applied in this particular case will be clarified later on in the discussion.

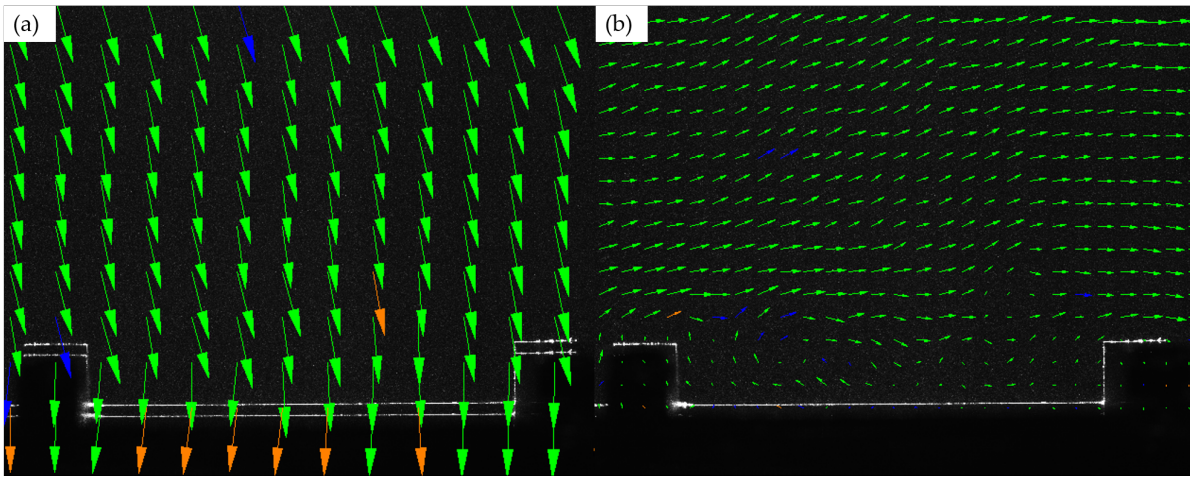


*Figure 4.4: Processing result of the raw image couple (a), and processing after the translation of the frame B (b)*

The two-step procedure is as simple as it possibly can be. Despite being impossible to exactly retrieve the peripheral displacement of each pixel, when the measurement plane is not perpendicular to the rotation axis, it is extremely easy to exploit laser reflections on the test section walls to evaluate the average peripheral displacement components (along both axes of the image frame of reference) of the frame B. An example is reported in figure 4.4 (a), where the processing of a raw image is reported. As it can be seen, the displacement vectors mainly represent the peripheral motion of the test section, while the bulk velocity main direction is horizontal and directed from left to right. In figure 4.4 (b) is reported the processing output of the same image couple after the frame B translation, where the computed displacements are in the range between 3 and 10 px through the whole image. This rough frame B de-rotation performed during the pre-processing can be applied to all image samples acquired, allowing to set the PIV parameters equal to the ones used for the static measurement, hence maximizing the relative displacement measured without exceeding the limit imposed by the quarter rule [20]. The cross correlation of images thus pre-processed (i.e. frame B translation equal for all th samples) allows to determine a first approximation of the relative displacements fields and concludes the first step.
In the second step of the procedure, the relative velocity fields have to be correctly computed using the actual peripheral velocity. In order to do so, the displacements used for the rough translation of frames B are algebraically added to the displacements fields obtained from the first step and finally, for each point the correct peripheral displacements are computed using the measured rotation velocity and the radius. The latter is computed starting from the knowledge of the rotation center position determined with the calibration procedure described before.
In the particular case of a plane aligned with both radial direction and the rotation axis, for the exemplification case of a 2D-PIV measurement, this procedure cannot be applied simply because the peripheral displacement is aligned with the camera optical axis. This means that if an ideal

optical configuration is considered (e.g. camera infinitely far from the focus plane), the measured peripheral displacement is zero on the whole plane, i.e. the camera would measure directly the relative velocity field.

Unfortunately, the real optical field of view of the camera in these applications cannot be approx-

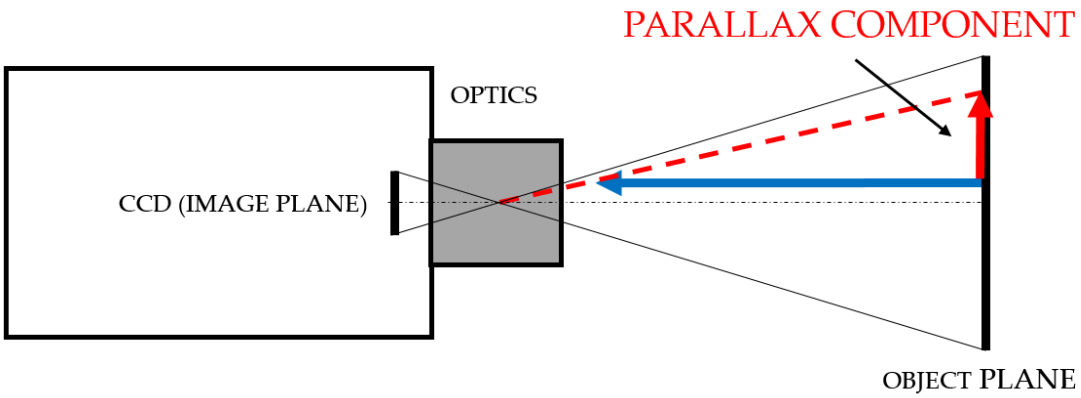


*Figure 4.5: Definition of the parallax component measured by a camera modelled as a pin-hole*

imated to one where light rays are collected parallel to the optical axis. Indeed, the optical field of view is conical and it can be modelled as depicted in figure 4.5. Modern camera optics such as the ones used in the present study are a complex system of several lenses with various shape, however, the pin-hole model (figure 4.5), despite being the most simple optical model, allows to deepen the understanding of the problems derived by the presence of a velocity component parallel to the optical axis.

This fact obliges to reconsider the assumption made in the former discussion that displacements parallel to the camera optical axis are not measured. Indeed, as shown in figure 4.5, the camera sees on the image plane the projection of the displacement, which from now on it will be referred to as parallax component. This displacement component is the result of the perspective view of the camera, in fact it affects only 2D-PIV setups while S-PIV is exempt because its functioning principle exploits the perspective view indeed.

### 4.1.1 Parallax error correction

The parallax error is a known problem of 2D-PIV that can be easily avoided by choosing the measurement plane orientation in order to contain the two major flow field components (e.g. avoid to measure the flow field on the cross section of a pipe, where the main velocity is perpendicular to the plane).

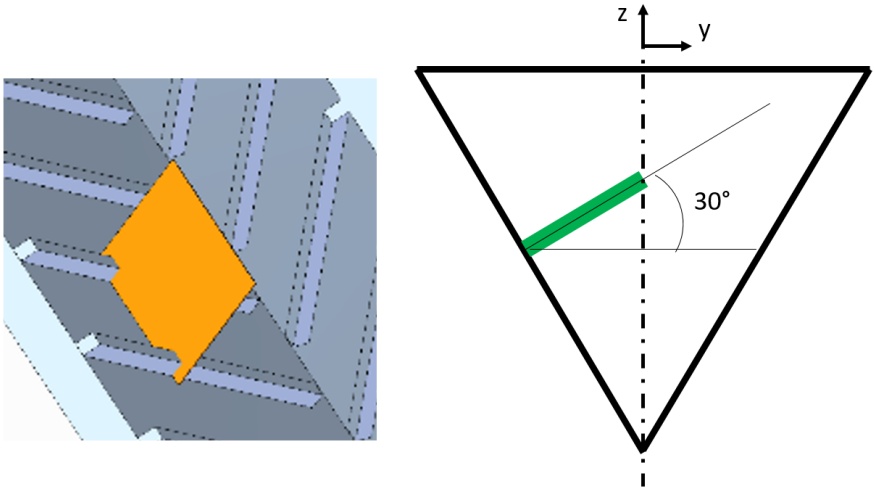


*Figure 4.6: Plane tilted* 30 deg *w.r.t. the xy plane*

In the rotating measurements, however, a much worse problem occurs: in fact, even if the plane is oriented accordingly to the flow field main components, in many plane dispositions, the major out of plane component happens to be the peripheral one. As previously discussed, the peripheral velocity could be up to one order of magnitude higher than the bulk flow velocity, hence the parallax component can be comparable to the velocity components, especially in the zones of recirculation.
In order to ease the discussion, it is worth to consider a practical case of a plane investigated in the present campaign. The specific plane had been chosen in order to investigate the flow field between the turbulence promoters inside the triangular equilateral channel (figure 4.6). As depicted in figure 4.6, the plane is perpendicular to both the channel side wall and the turbulence promoters, and it can be seen as an xy plane rotated along the x axis by 30°. Figure 4.7 shows the peripheral velocity and its components on the measured plane

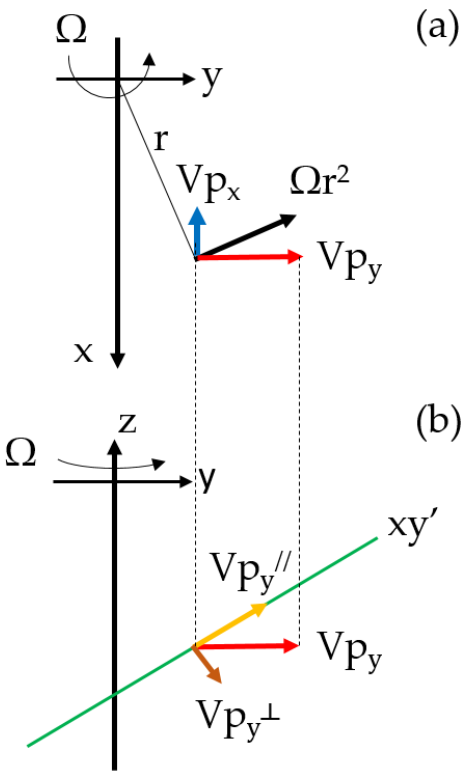


*Figure 4.7: Peripheral components on xy plane (a) and yz (b)*

that has to be used to retrieve the relative velocity field in the final step of the two-step procedure. As it can be seen in figure 4.7 (a), on the xy plane the peripheral velocity can be decomposed in a $VP_x$ and a $VP_y$, however, while $VP_x$ lies on the measurement plane, $VP_y$ can further decomposed in two other components. Figure 4.7 (b) depicts the decomposition of $VP_y$ in a component parallel to the measurement plane ($VP_y^{//}$) and a one perpendicular ($VP_y^{\perp}$), the latter being also parallel to the camera optical axis.

The peripheral components used to compute the relative velocity field are $VP_x$ and $VP_y^{//}$, however,

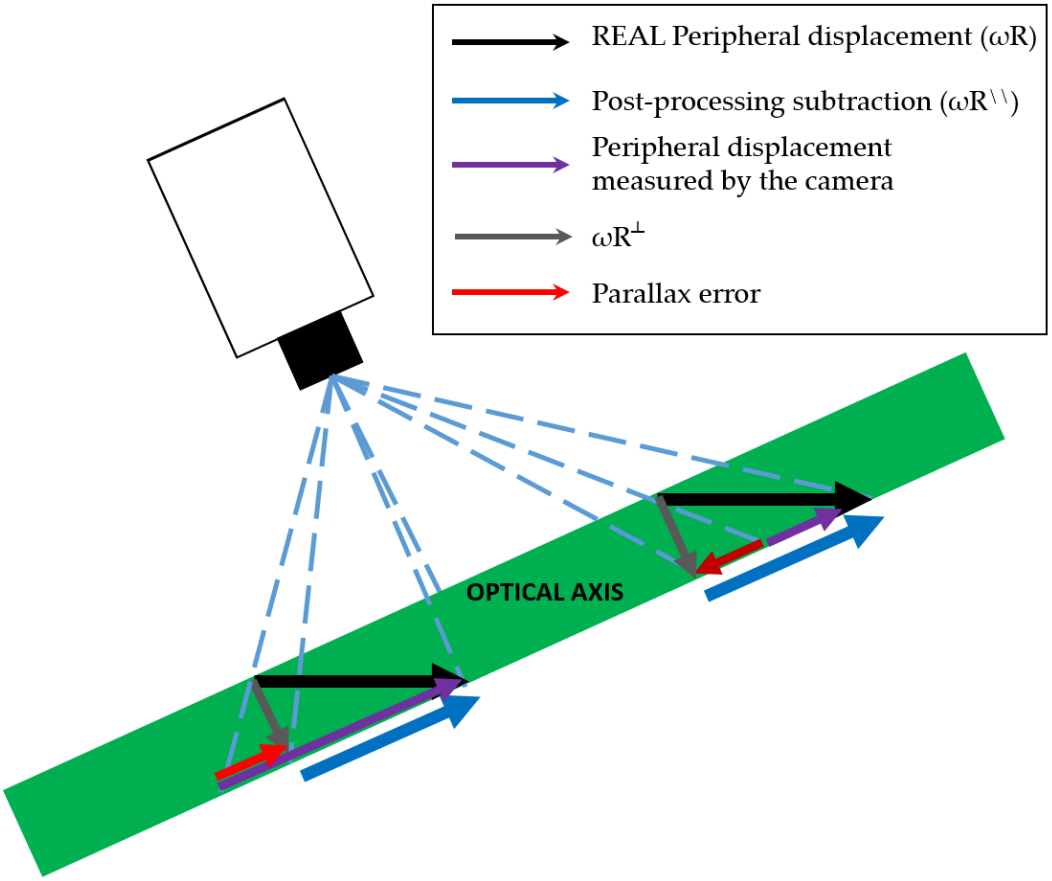


*Figure 4.8: Sketch of the parallax error*

due to the conical field of view, those are not the velocities seen by the camera. This concept is clarified in figure 4.8, where the view of the yz plane is represented and two examples of peripheral velocity views are schematized. As it can be seen, the velocity component seen by the camera (purple arrows) are projections of the real ones (black arrows). The difference between the actual peripheral velocity components and those measured by the camera is indeed the perspective view of $VP_y^{\perp}$ projected on the measurement plane, i.e. the parallax error. The parallax error affects both peripheral components (along x and y), however only the schematization for

the y component is reported here.
In order to obtain reliable velocity data, it is obvious that a parallax correction is mandatory. Exploiting the pin-hole model, in order to be able to compensate for the parallax distortion, two data are required: the distance between the focus point and the focus plane and the optical axis projection position on the image plane. As far as the latter is concerned, in an error-free setup, the projection of the optical axis falls exactly in the center of the image. However, in this kind of application, where the distance between the camera CCD and the measurement plane can be up to one meter, a misalignment of the camera of one degree would led to an optical axis projection displacement from the center of about 18 mm. Since the correction we are looking for is very small, the exact position of the optical axis projection is fundamental.
Since it is not possible to directly measure the distance between the focus point and the mea-

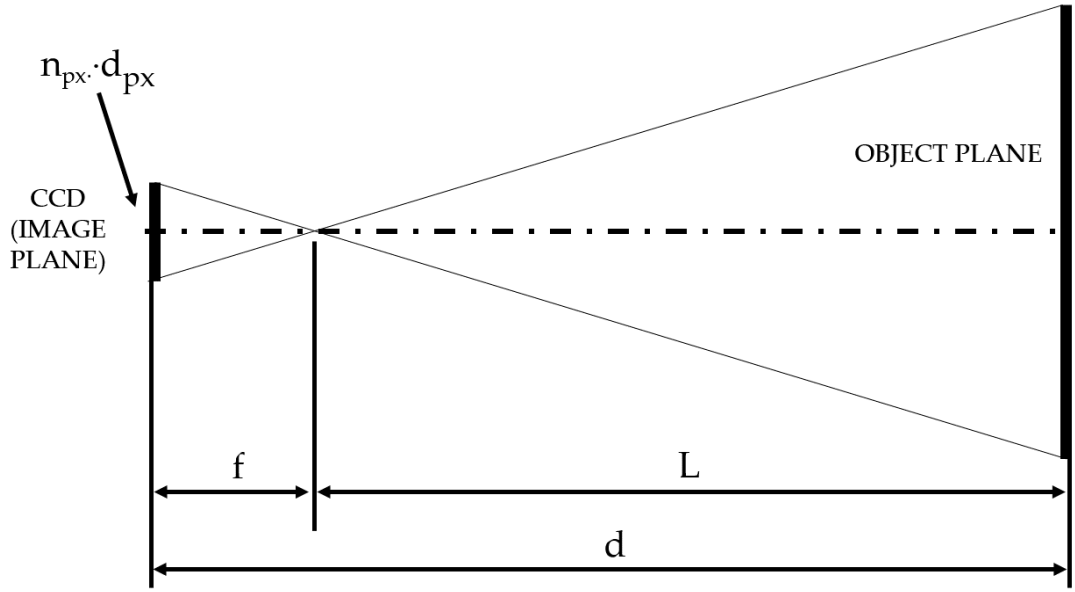


*Figure 4.9: Sketch of pin-hole model*

surement plane (i.e. focus plane), the pin-hole model depicted in figure 4.9 had been exploited to retrieve a correlation between the main system characteristics parameters, i.e. the pin-hole model focal length (f), the magnification factor (M), the CCD pixel dimension and finally the distance between the CCD (i.e. the image plane) and the object plane. The resulting equation gives the distance in function of the former parameters:

$$f = \frac{d}{1 + \frac{1}{M \cdot d_{px}}} \tag{4.5}$$

However, the pin-hole model focal length (f) does not correspond to the real optics focal length, since the real optics is now modelled as a single point. In order to correlate these two parameters,

a dedicated pin-hole model focal length calibration procedure has been developed. The camera is fixed on a table and a target with a regular grid has been positioned at several known distances from the CCD, which position inside the camera is known from the constructor datasheet. The calibration allows to correlate the magnification factor (M), computed thanks to the acquisition of an image of the target, and the distance ($d = L + f$) between the CCD and the focus plane as shown in figure 4.10. Thanks to equation 4.5, it is possible to compute the pin-hole model focal length in function of the magnification factor (M), the pixel dimension and the measured total distance (d). With these data, L can be computed as difference between d and f.
The calibration output is then a direct correlation between the magnification factor and the distance L as reported in figure 4.10 (a). In this way the correct distance L can be computed directly from the measurement setup, since the only data required is the magnification factor. For sake of completeness, the correlation between magnification factor and focal length is reported in figure 4.10 b). In this case the optic was a Nikkor with f=105mm, and it can be noted that the computed f goes to the nominal value for increasing distances, hence the system behaves more like an ideal one where light rays are collected parallels. As far as the optical axis projection on

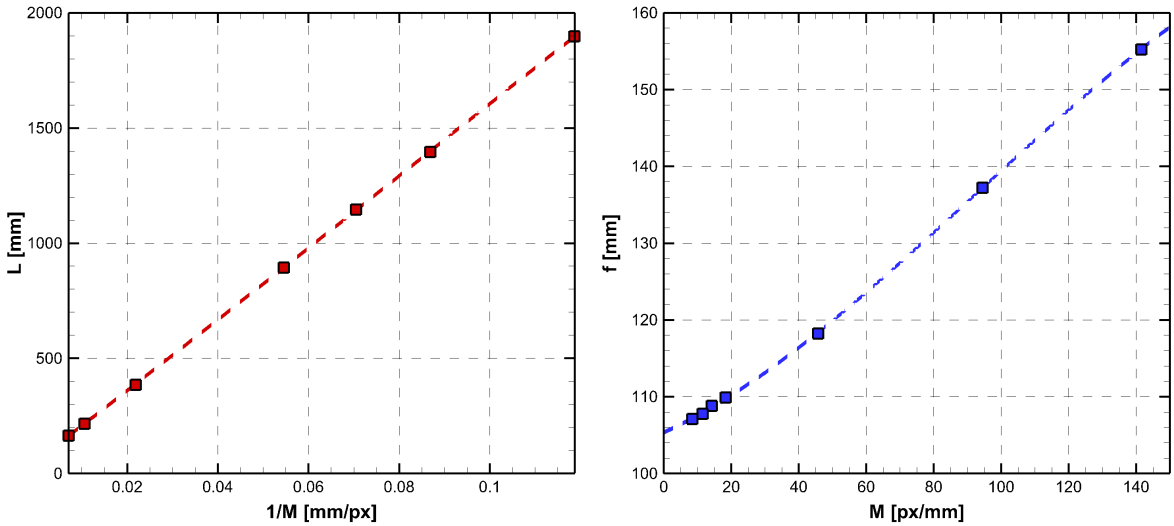


*Figure 4.10: Correlation between L and 1/M (a) and f and M (b) for a Nikkor optic with f=105 mm.*

the image plane is concerned, the definition of a reliable procedure took a higher effort. In the beginning, it was chosen to use a free software for camera calibration such as Camera Calibration Toolbox developed at Caltech. However, after several tests, the results were never repeatable and reliable due to the complexity of the PIV optical setup. Indeed, the high focal length (f=105 mm) and the complexity of the optics and the almost comparable dimension of the CCD and the image plane (64x51 mm vs 8.6x6.8 mm) determined a problem too sensitive to small perturbations to be solved with the numerical tool.
However, in order to overcome this problem, a dedicated empirical calibration procedure has been

developed exploiting indeed the perspective view of the camera conical field of view. The basic ideas are that points moving along the optical axis are seen by the camera as fixed and lines aligned with it are seen as points. From these two elementary concepts, two different calibration procedures have been defined. Exploiting the first one, several images of a dotted target parallel to the focus plane have been taken at different positions along the optical axis, with a distance between each position of about one millimeter. The images are processed in order to compute each dot displacement using all combinations of target positions. For each dot, all the displacements obtained with that procedure are averaged together. In this way it is possible to obtain a map that allows to determine the optic axis projection, which corresponds to the point where the displacement is minimum. An example of result is reported in figure 4.11.

The other calibration procedure involved the use of a parallelepiped target shown in figure 4.10,

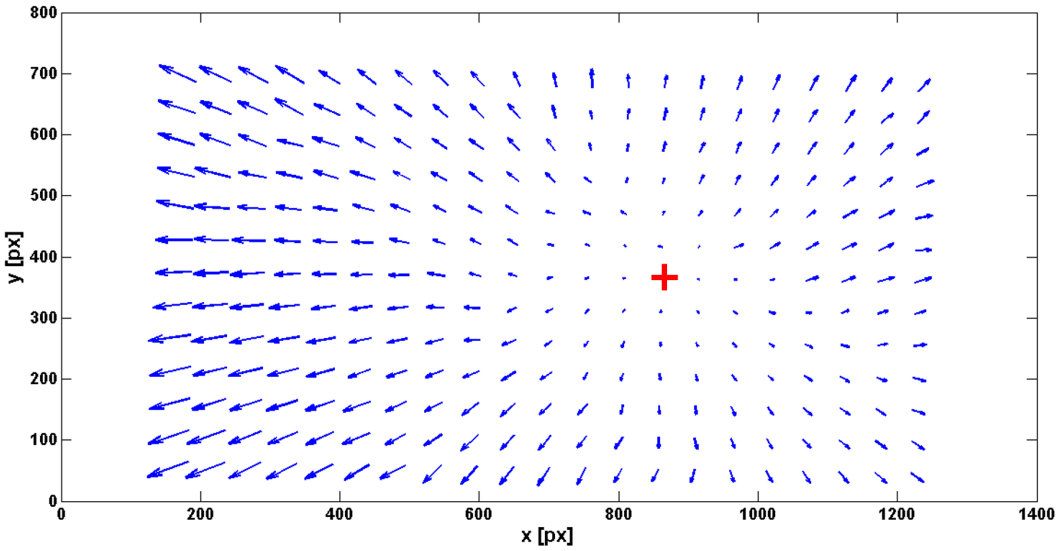


*Figure 4.11: Example of determination of the optical axis projection with the displacement of a target with a regular pattern. The position of the optical axis is highlighted by a red cross*

where on one of the main faces several lines were carved parallel to the side. The target was then put in the test section either parallel to the channel wall (figure 4.12 (a)) or the turbulence promoter side (figure 4.12 (b)) and displaced in the perpendicular direction until the lines were seen by the camera as points. The two position define the x and y coordinates of the optical axis projection on the image plane.

The result of this elaborated procedure is reported in figures 4.12 (c) and (d), where the parallax component on the image plane is shown for two opposite rotation directions of the channel. As it can be seen, the parallax component can be up to 1 pixels, hence the correction allow to further increase the reliability of the measure.

The procedure described in the former paragraphs can be applied for every plane orientation,

provided a deep understanding of the resulting peripheral velocity components is achieved. In particular, going back to the particular case of the plane xz, only the parallax compensation is needed in order to obtain the correct velocity field.
A more quantitative discussion on the methodology uncertainties will be provided in appendix A.3.

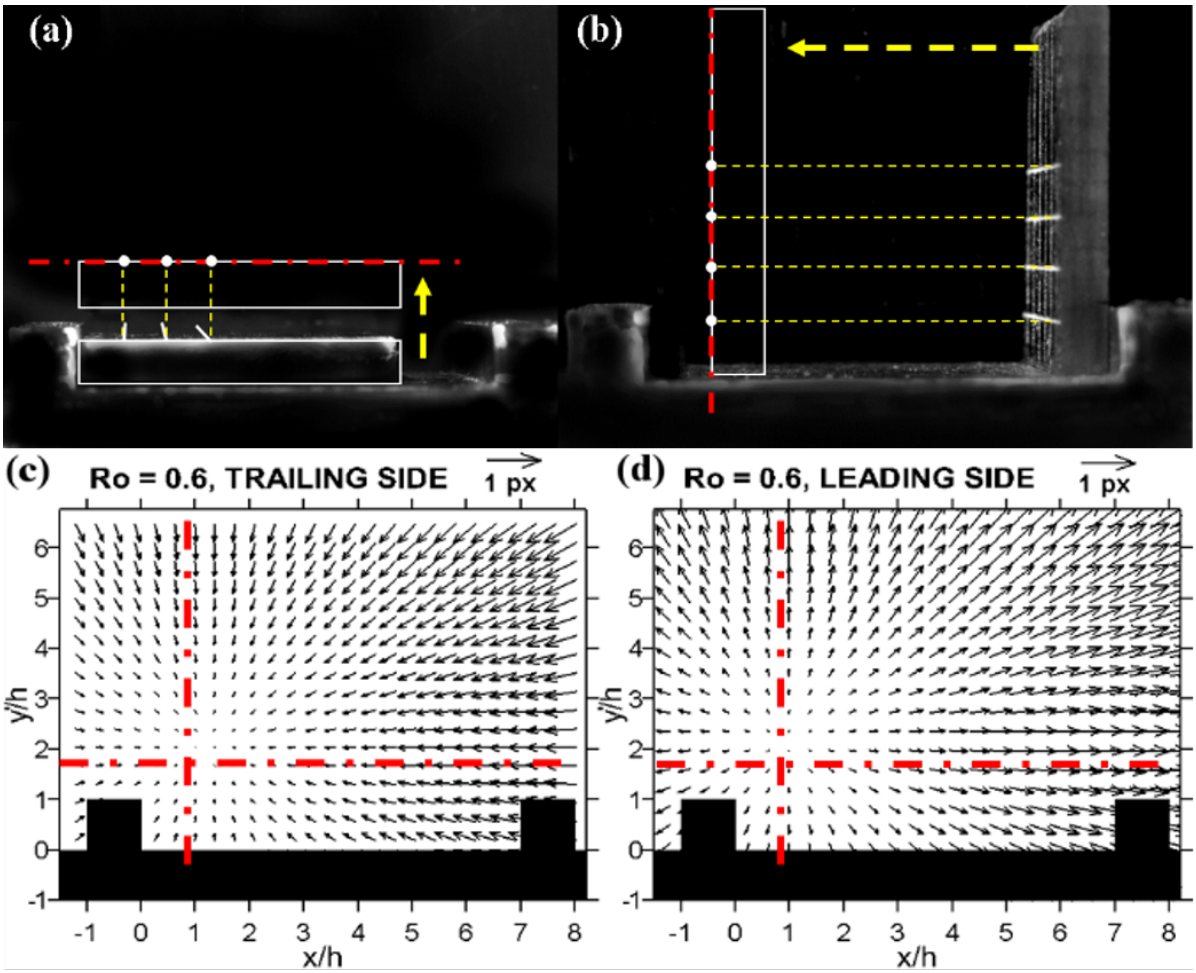


*Figure 4.12: Empirical procedure for the determination of the optical axis projection y (a) and x (b) coordinates. Resulting parallax correction for two rotation directions of the plane (c-d)*

CHAPTER 5

# FACILITY FOR ROTATING CHANNELS INVESTIGATION

The experimental activity of flow field measurement on both geometries has been carried out on the rotating facility of the Turbomachinery Laboratory of the University of Udine. The facility has been firstly developed and realized during the Ph.D research project of Mucignat [32], however, in order to be able to carry out the experimental campaigns conducted during this research project, the rotating facility had been upgraded.

The improvements mainly regarded the structure containing the test rig, the test rig mechanical structure, the mechanical transmission. Various additional and minor features were also added to the facility in order to improve its functionality.

The ceiling of the confining structure had been moved to an higher height in order to allow a more comfortable setup realization. In fact, a metallic frame with rails for the PIV setup instruments carriages is fixed on the ceiling. In the experimental activity described in part 6, indeed, the measurements have been conducted with both the cameras and the laser fixed to the suspended frame, as it can be seen in figure 5.2 (a). Probably the most important improvement had been the substitution of the metallic frame that supports the rotating equipment. The new one, as it can bee seen by comparing figure 5.3 (b) and (a), has a reticular structure composed by elements with increased cross section and thickness (respectively $40 \times 40$ mm vs $25 \times 25$ mm and 4 mm vs 3 mm), conferring to the structure more stiffness and mechanical resistance. The replacement of the old structure had been twofold beneficial: heavier test sections could now be tested and under the rotating facility an electro-fluidic joint could now be placed.

In the old configuration, air was fed to the rotating equipment through a bearing placed on top of a rotating settling chamber and the rotating equipment was driven by an electric motor though a mechanical transmission realized with a crown worm, as it can be seen in figure 5.3 (a). In the new configuration, air is fed from the bottom, through an hollow shaft with internal diameter of

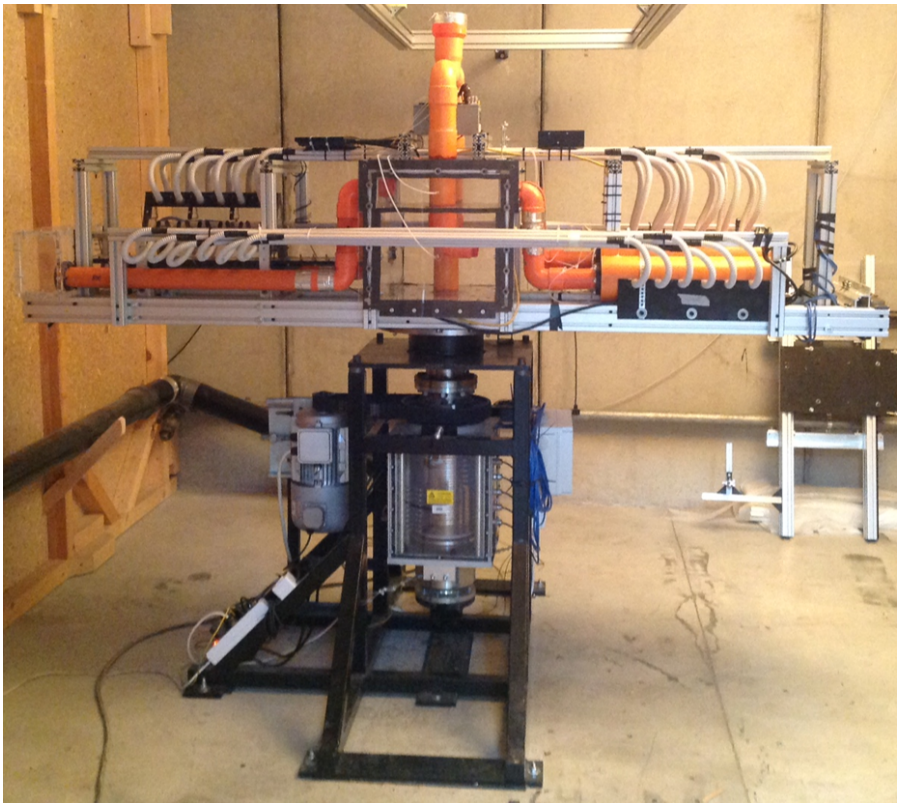

*Figure 5.1: Facility for measures in rotating channels*

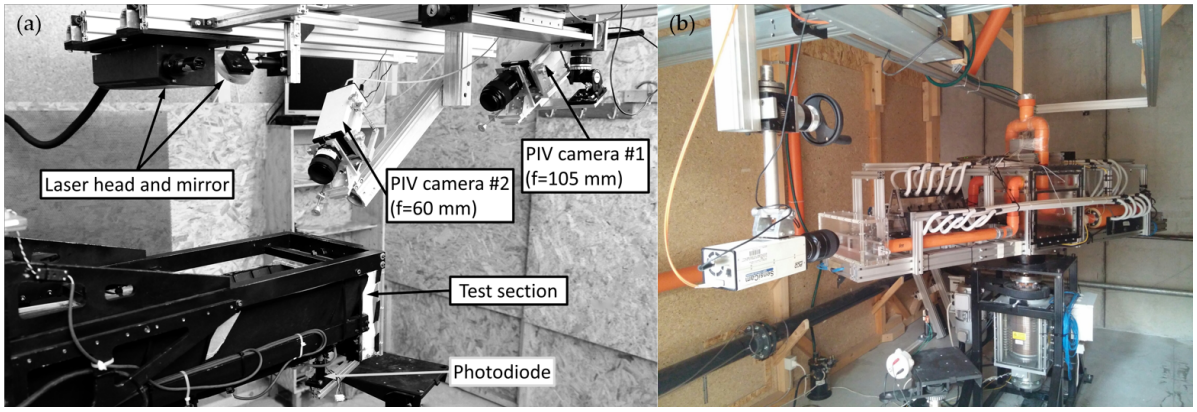


*Figure 5.2: Subfigure (a): PIV setup designed for the experimental campaign on the ribbed channel (chapter 6). Subfigure (b): PIV setup designed for the experimental campaign on the advanced leading edge cooling system (part 5.2 (b))*

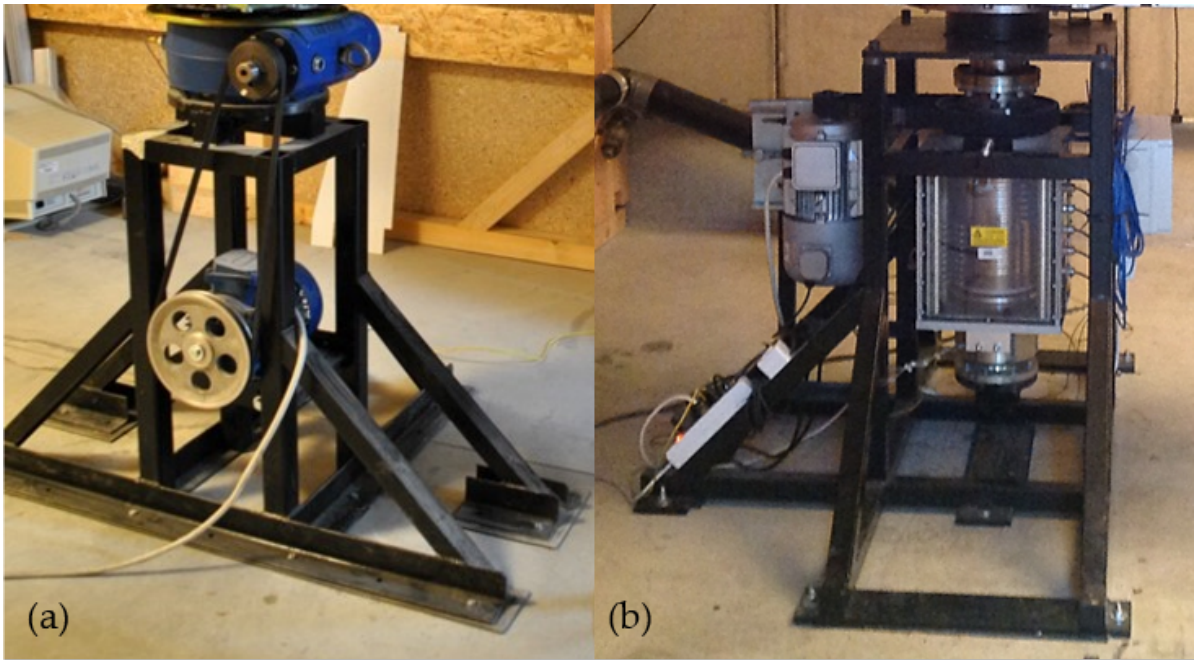


*Figure 5.3: Comparison between the old structure (a) and the new one (b). There can also be noted the electro-fluidic joit, the different mechanical transmission and electric motor*

100 mm and a thickness of 15 mm. The shaft is supported by two bearings on the top extremity and kept aligned with two more bearings installed on the bottom end. The shaft, hence the rotating part of the test rig, is driven by an electric motor with four times the power of the old one (8 kW vs 2 kW) through a toothed belt (5.3).The electric motor is controlled by an inverter that allows to set the desired rotational speed.
On the shaft several slip-rings had been installed in order to realize an electrical link between the rotating equipment and the control station. The slip-rings allow to transfer the following signals:

- thermocouple (J type) - 10 channels
- low power output signal of measurement instruments (e.g. pressure transducers) - 20 channels
- standard 24 VDC / 220 VAC power supply
- high current power supply (maximum current of 200A)
- ethernet communication

Unfortunately, the ethernet communication reached a maximum data rate of 9 Mbps, and didn't provide a reliable and stable connection between the on board instrumentation. The solution

adopted to overcome this problem was to install a router on the rotating equipment and one on the control station; by linking the two of them (i.e. creating a Wi Fi bridge) it was possible to ensure a effective communication.
In particular, this solution had been fundamental for the experimental campaign on the advance leading edge cooling system (part IV), where a pressure scanner (NetScanner-9116, 16 channel 0-25mbar) was installed on the rotating test article in order to measure the pressure signals of three calibrated orifice mass flow meters.
As far as the air circuit is concerned, the facility is an open loop meaning that air is drawn/discharged from/in the ambient, and it can work either in pressurized or depressurized conditions. This possibility allow higher flexibility in the test section design and can be easily achieved using either a six stages fan (for the pressurized condition) or a vacuum pump, specifically a trilobe rotor pump. In either cases, the machine is driven by an electric motor, which rotating regime can be controlled through an inverter.

# Part III

# RIB ROUGHENED TRIANGULAR CHANNEL

CHAPTER 6

# EXPERIMENTAL INVESTIGATION

## 6.1 Test section

The investigated test section (Fig. 6.1) is a straight channel with triangular equilateral cross section and turbulent promoters (i.e. square ribs) perpendicular to the flow main direction (i.e. radial) realized on two lateral walls (i.e. leading and trailing walls). The test section geometry, beside the turbulent promoters, is the same as the one investigated by Pascotto et al. [13], where cross sectional sides have a length of L = 130 mm and a hydraulic diameter $D_h = 75.05mm$ while the whole channel is 870 mm long. Considering the settling chamber, the maximum radius is 1.1 m while the inlet is placed at r = 214 mm. The test section lateral walls are made by two aluminium slabs, where turbulence promoters are directly machined on them as squared ribs of 6.5x6.5 mm section and p = 52 mm, giving a pitch to height ratio p/e = 8. The latter had been chosen in order to be consistent with the geometry investigated by Liu et al [1]. Moreover, the ribs are staggered as depicted in figure 6.1. The remaining wall (top) has been realized with removable plexiglass or glass covers in order to allow optical access for the PIV camera/s and to allow the positioning of ad-hoc realized targets necessary for both 2D-PIV and S-PIV calibrations, which were performed as described in section 3.3.

In order to provide the heat necessary to reach non-isothermal conditions (i.e. $Bo \neq 0$) a $25\mu m$ thick inconel sheets have been glued on the outside face of the lateral aluminium walls (figure 6.2 (b)). The two inconel sheets have been connected to realize a parallel of resistors, and, in order to provide the powering and exploiting the Joule effect, the inconel sheets have been connected to a power supply ($P_{max} = 1600W$, $I_{max} = 100A$ $V_{max} = 16V$) through the rotating joint.

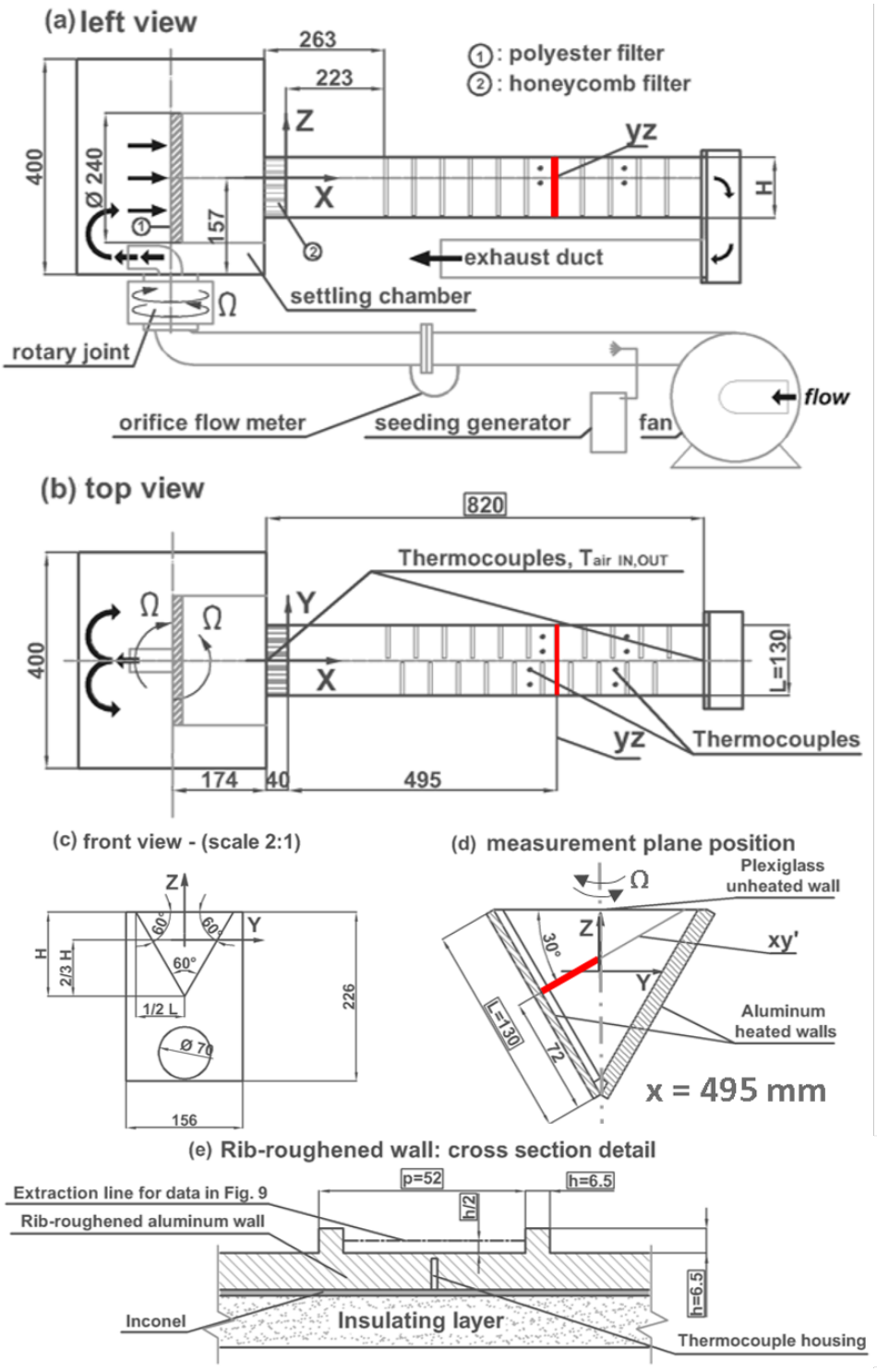


*Figure 6.1: Experimental facility, nomenclature and positions of the PIV measurement planes (highlighted in red)*

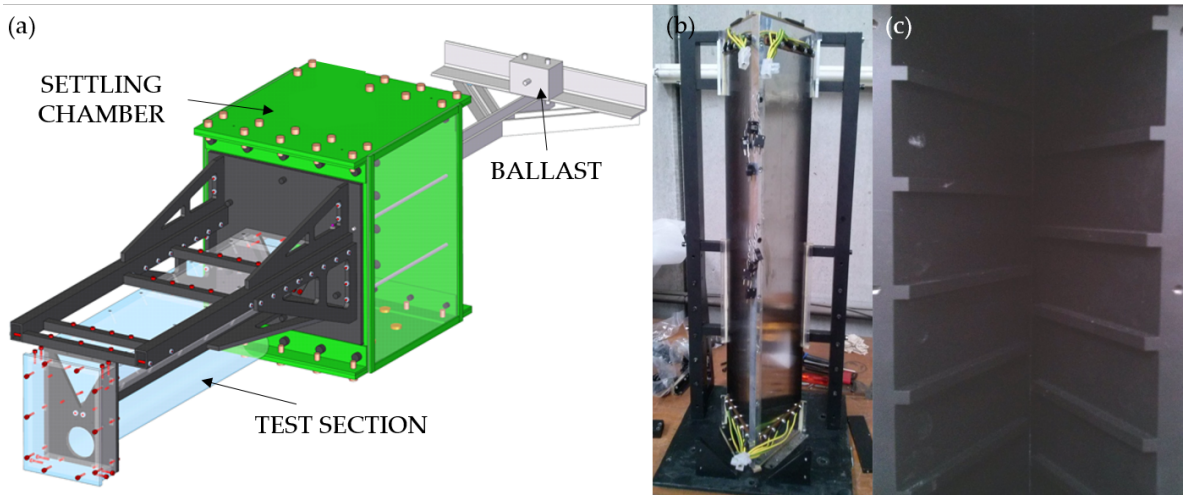


*Figure 6.2: 3D model of the rotating arm (a), test section (b) without the insulating layer and a detail of the internal surface (c) painted black to increase PIV image contrast*

Since thermal losses are a critical aspect when a constant temperature has to be guaranteed and moreover, stationary conditions have to be maintained through a significative period of time (e.g. the acquisition of PIV image samples), the test section has been isolated. Three centimeters thick foam slices have been glued to the air exposed face of the inconel sheets and the whole zone has been covered with a neoprene sheet 10 mm thick, which has been fixed by means of plastic strips. The latter has the additional purpose of ensure the fixing of the isolating coating during rotation.

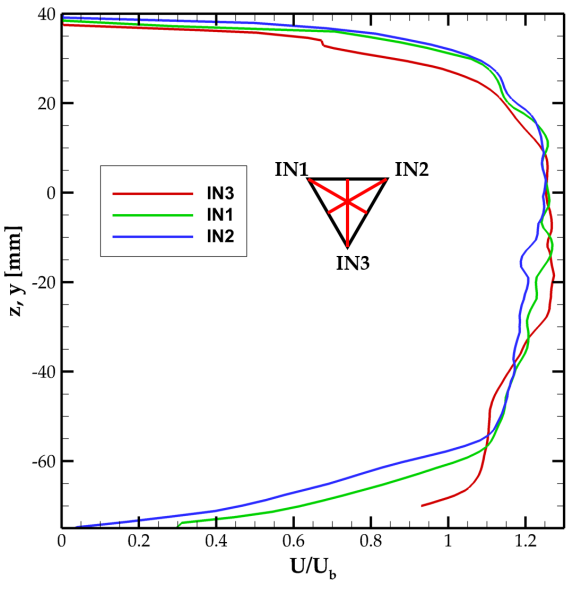


*Figure 6.3: Comparison of the streamwise velocity profiles from the 2D-PIV extracted at position x = 120 mm from planes IN3, and IN1-2*

The temperature of the internal face has been monitored in several points by means of thermocouples embedded in the walls. The thermocouples where inserted in the walls inside holes machined from the external side and deep enough to leave a 1 mm aluminium thickness on the wall. Eight thermocouples were installed, two one inter-rib pitch before the measurement zone and two after and for both lateral walls (see figure 6.1 (c) and (e)). The thermocouples signals were continuously monitored by a NI Compact RIO. Tests have been performed in order to assess the temperature uniformity

in both static and rotating conditions: 1K differences between the readings of thermocouples on the same wall was the typical behavior. Under rotation, the difference between thermocouples in homologous positions on the two walls, showed a maximum difference of 5K due to the non-symmetrical behavior of the flow field, which is intrinsic in the triangular geometry ([13]).
The test section is assembled with a settling chamber and the counterbalancing ballast, as it can be seen in figure 6.2 (a). Between the test section and the settling chamber a layer of bakelite has been installed in order to reduce thermal conduction. The same solution has been adopted for the coupling with the metallic frame that supports the discharging volume at the tip.
As it can be seen in figure 6.1, the test section inlet is not in a symmetrical position with respect the settling chamber. In order to avoid ill-conditioned inlet velocity profiles, an additional cylindrical chamber had been added as depicted in figure 6.1. The cylindrical chamber sucks air through a polyester filter that allows to uniform velocity and a coarse honeycomb filter that suppresses velocity components not aligned with the radial direction. As it can be seen also from the velocity profiles extracted along the test section bisectors, shown in figures 6.3, the velocity distribution is rather uniform and symmetrical. The settling chamber and inlet conditions assessments were performed only for the smooth channel, due to the lack of the necessary optical access in the ribbed channel. However, since the settling chamber and the channel inlet configurations are the same for both test sections, there is an extremely high confidence that the inlet conditions are the same for both geometries.
The whole ensemble (test section-settling chamber-ballast) is installed on the rotating joint flange. The air is fed to the test section by a six-stages centrifugal fan through an orifice flow meter and the rotating joint. At the inlet of the test section a fine honeycomb filter is installed for the first 40 mm in order to suppress eventual velocity components raised in the cylindrical chamber during rotation. After the test section air is discharged at the tip in a rectangular volume and then is redirected radially inward where it is discharged in atmosphere. The adoption of a return volume allows the avoidance of any perturbation to the channel flow near the tip region that could conversely occur under rotation if the channel was set with a free radial outlet.

## 6.2 Investigated planes and reference conditions

The measurements planes were chosen considering the final twofold aim of the investigation. On one hand, the purpose is to investigate the macroscopic rotation-induced flow structures in the channel in order to explain the thermal results obtained by Liu et al. [1]. On the other hand, buoyancy effect has to be assessed and the recirculating structure between the turbulence promoters has to be characterized and compared to the flow field measured by Coletti et al. [10] in the square channel. In order to fulfil these aims, the most representative planes are the yz and xy', as shown in figure 6.4. In particular, plane yz is coincident with the channel cross section

and it is placed at the center of the 6th inter-rib on one side and at the center of the 7th rib on the other. Plane xy' is perpendicular to both the test section lateral wall and the rib (i.e. from a frontal view it is inclined of 30° with respect the rotation axis). Plane yz is placed at a radius of 709 mm, which has been used as an average value for the computation of the Bo on xy'.
In order to evaluate both leading and trailing side, the test section had been spun in both rotation directions. This approach has the advantage to allow the use of the same PIV setup and to reduce experimental time.
Measurements on the inter-rib plane have been performed with the 2D-PIV approach mainly

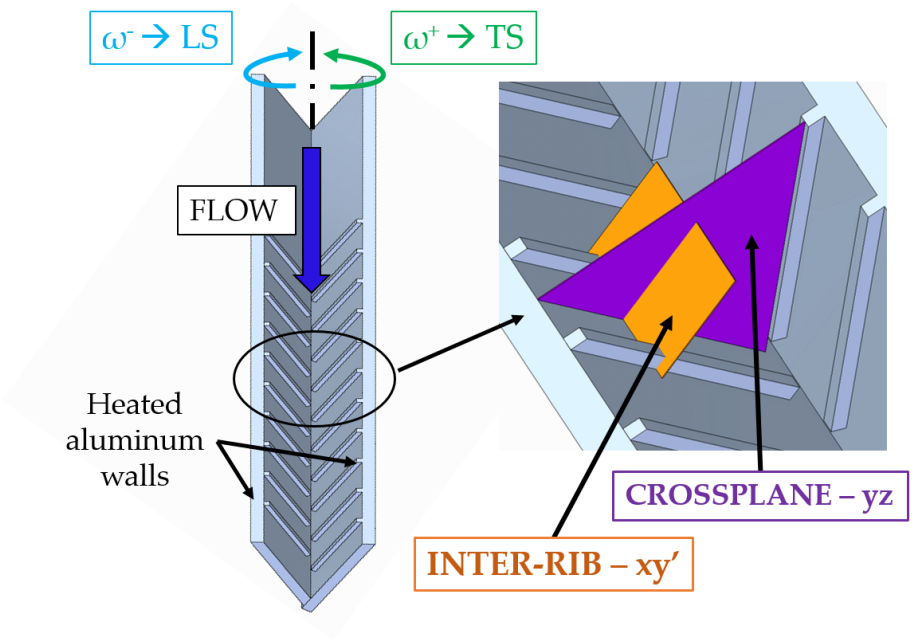


*Figure 6.4: Investigated planes: cross section (purple) and inter-rib zone (orange)*

to reduce the setup complexity and in view of the fact that, despite de existence of out of plane components (i.e. secondary flows in rotating condition), predominant velocity components would lie on the measurement plane. Furthermore, the location of the plane did not allow to realize a S-PIV setup with a satisfying angle between the cameras. Thus, the stereo approach would not have resulted in a higher flow field accuracy, not justifying the increase of setup complexity.
Measurements on the cross plane have been performed with the S-PIV technique in order to obtain information on both secondary flow structures and bulk velocity distribution. The calibration have been performed as described in chapter 3.3.2.
The nominal magnification of the PIV images ranges from 17 pixel/mm (S-PIV) to 20 pixel/mm (2D-PIV), which turns in a vector resolution from 1.06 to 1.25 vectors/mm, respectively. The PIV separation time had been chosen in order to guarantee maximum relative displacements of the

**Table 6.1:** *Test Matrix*

| Re | Ro | Bo | Channel side |
|---|---|---|---|
| 10000 | 0.2 | 0 | LS |
| | | | TS |
| | | 0.08 | LS |
| | | | TS |
| | 0.6 | 0 | LS |
| | | | TS |
| | | 0.7 | LS |
| | | | TS |

order of 8-10 px, following the quarter rule [20].
The test matrix shown in table 6.1 had been chosen in order to fulfil many requirements: the data indeed had to be compared with the data available from the smooth channel [13], the thermal data obtained by [1] on the same geometry, and the flow field measurements performed on the squared channel by Coletti et al. [10]. Tests have been performed at constant Reynolds number of Re = 10000 for two rotation numbers Ro = 0.2-0.6 and for one wall temperature of $Tw = 110°C$, resulting in Bo = 0.08-0.7 for the lower and higher rotation number respectively.
Both Re and Ro are defined at the inlet of the test section, while Bo is defined at the center of the 6th inter-rib, corresponding to a radius of r = 0.709 m.

## 6.3 Results

The test section inlet conditions are te same of the smooth channel investigated by Pascotto et al.[13]. In fact, not only the settling chamber configuration and the filters used are the same (in particular the fine honeycomb filter placed in the first 40 mm of the channel), but also the initial channel tract (263 mm) is smooth, as it ca be seen in figure 6.1 (a). In view of these considerations, the velocity profiles provided in figure 6.3, can be taken as representative for the ribbed channel inlet conditions. The initial smooth section has been also designed in order to replicate the channel investigated by Liu at al.[1], in order to exploit the thermal data already available.

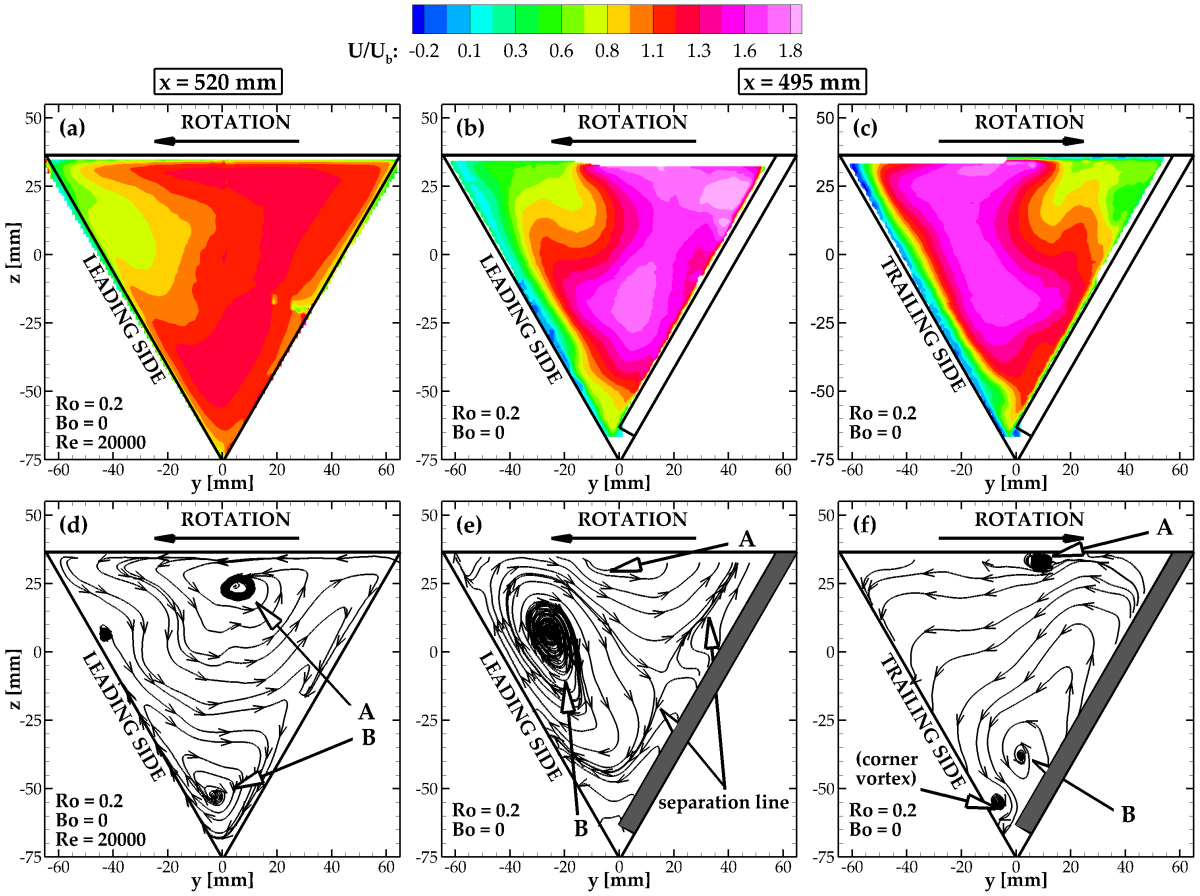


*Figure 6.5: Comparison of the three components flow field on the cross-section between the smooth channel from Pascotto et al. [13] and the ribbed channel. Ro = 0.2*

### 6.3.1 Coriolis induced vortices

#### 6.3.1.1 Isothermal case

In order to better understand the flow field in the ribbed channel, it is worth to compare them with the results obtained in the same facility on the smooth channel and reported by Pascotto et al. [13]. It has to be pointed out that the data from [13] had been obtained for a different Reynolds number with respect the one of this experimental campaign (Re =20000 vs Re=10000). However, in the work of Pascotto et al. [13] the Coriolis' induced vortices were found to be Reynolds-indipendent.

As it can be seen in figure 6.5 (d), the secondary flow structure is characterized by two counter-rotating vortices and separation/reattachment points located in the upper apices of the test section. The bulk velocity distribution (figure 6.5 (a)) reflects accordingly the mass transportation provoked by the vortices, hence the deficit of velocity near the leading side (top apex), and the velocity increase near the trailing side. Another aspect that can be highlighted is the velocity peaks

located near the upper wall and the lower apex. These are caused by the Coriolis force component aligned with the bulk velocity direction that accelerates zones where velocity component V (y) is negative (i.e. near the top wall and the lower apex).

In the ribbed channel, the presence of turbulence promoters does not affect the secondary flow

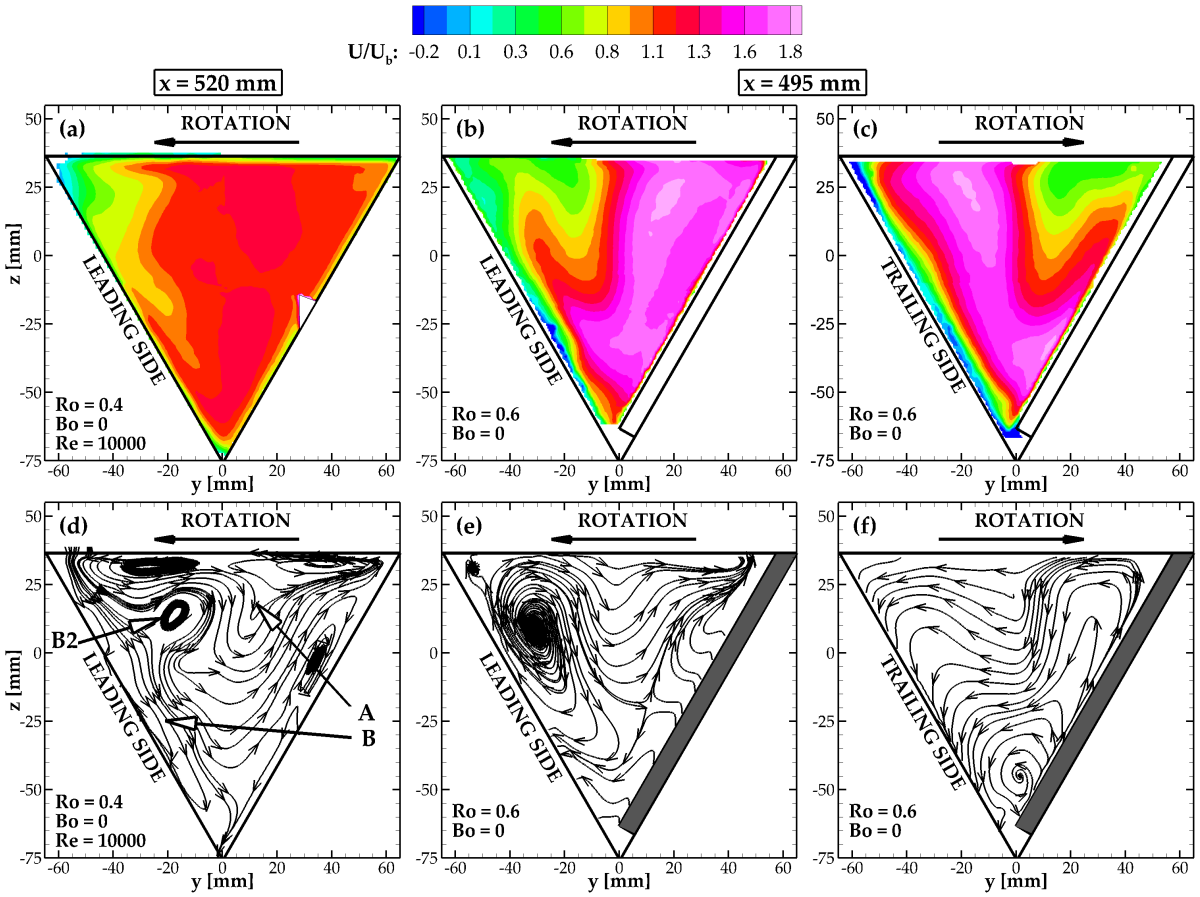


*Figure 6.6: Comparison of the three components flow field on the cross-section between the smooth channel from Pascotto et al. [13] and the ribbed channel: Ro-dependence*

structures development despite strongly changing their layout. Indeed, as it can be seen in figure 6.5 (e), the two vortices A and B are still recognizable, even with the presence of the rib causing an upward movement of the flow that pushes the vortices couple towards the leading side. Moreover, vortex B covers a larger area of cross section with respect the smooth channel, confining vortex A near the upper wall. When the rotation direction is inverted(figure 6.5 (f)), the same vortices can still be found with opposite orientation (clockwise becomes counter-clockwise and vice versa) accordingly to the background vorticity (i.e. channel rotation side). The velocity contours in the two geometries are rather similar (figure 6.5 (a-b-c)) in distribution, however in the ribbed channel the velocity peak near the lower apex is penalized with respect to the smooth

channel. This effect is probably due to the high blockage realized by the ribs in correspondence of the apex.
The last aspect that can be highlighted is the rather different conditions the trailing and leading side experience in the ribbed channel in regards of near wall flow. In fact, as it can be seen by comparing figure 6.5 (e) and (f), vortex B is much closer to LS than TS, unlike in the smooth channel, where the vortices are almost symmetrical with respect the channel vertical bisector (figure 6.5 (a)).
When the rotation number is increased, however, the smooth and the ribbed channels show very different behavior. In the smooth channel the secondary flow structures are very sensitive to Ro increase, as it can be seen in figure 6.6 (d). The genesis of the third rotating cell B2 has been already discussed in section 2.2, and the cause is, as for the squared channel, the accumulation of low momentum fluid near the leading side top apex. The ribbed channel, on the other hand, does not show any kind of rotation number sensitivity, at least as far as the secondary flow structures layout is concerned and actual Ro numbers are considered. The streamwise velocity distribution (figures 6.6 (b) and (c)), however, shows an higher non-uniformity, with an higher velocity peak near the trailing side and a more extended velocity deficit region near the leading side upper apex.

#### 6.3.1.2 Non-isothremal case

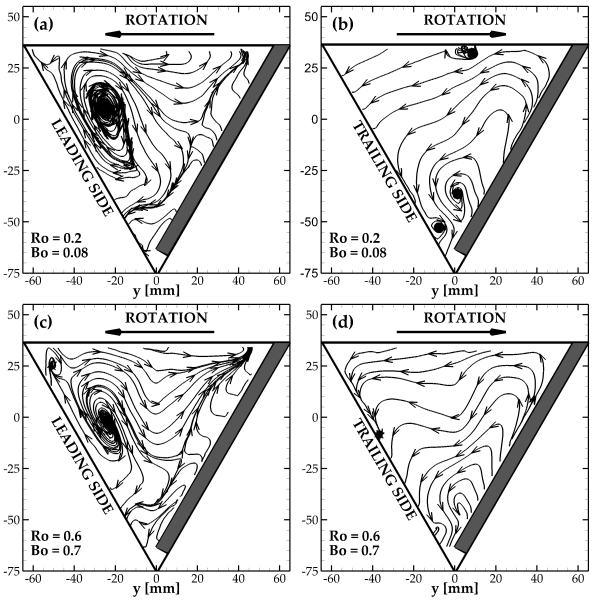


*Figure 6.7: Secondary flow structures for the non-isothermal case: upper row Bo = 0.08, lower row Bo = 0.7*

When the effect of buoyancy forces is taken into consideration, the secondary flow structures do not change considerably. In fact, buoyancy forces, unlike Coriolis ones, do not generate velocity

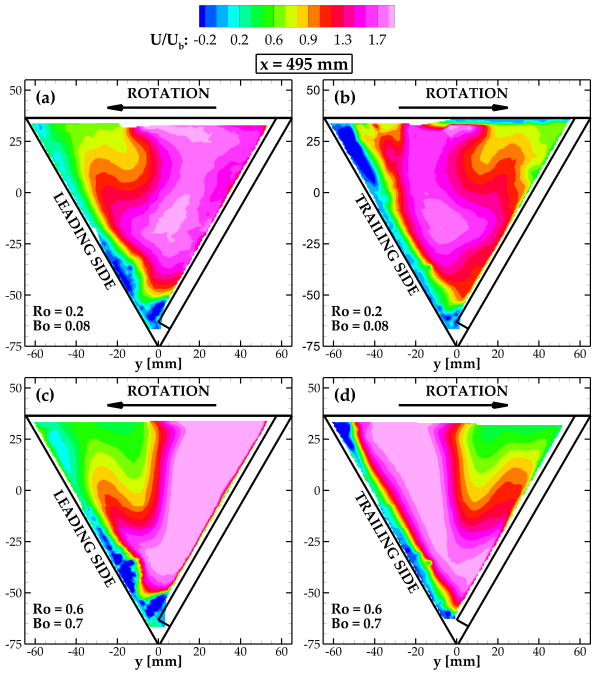


*Figure 6.8: U velocity component contours: upper row Bo = 0.08, lower row Bo = 0.7*

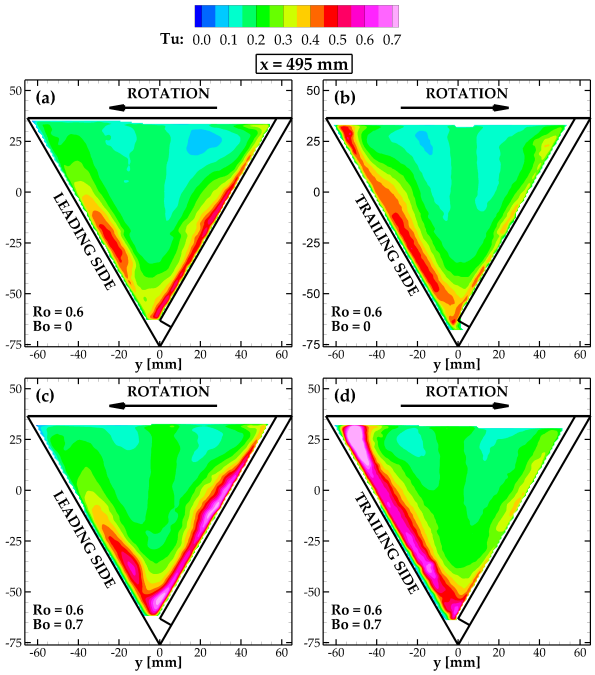


*Figure 6.9: Turbulence intensity (Tu) contours: left column Bo = 0, Ro = 0.6 (isothermal), right column Bo = 0.7, Ro = 0.6*

components on the channel cross section, therefore a behavior like the one showed in figure 6.7 (b-c) has to be expected. Moreover, the increase in Bo (from 0.08 to 0.7) does not causes relevant changes in the secondary flow structures, as it can be seen in figure 6.7.
On the other hand, buoyancy forces generate an acceleration unbalance between near wall fluid and core flow (due to the temperature, hence density, gradient), as described in section 2.1.2, that increases the velocity peak at the disadvantage of the near wall flow. This effect can be appreciated in figure 6.8, where the U velocity component contours are reported.
Figure 6.9 reports the comparison between the turbulence intensity levels (Tu) in the rotating case at the higher rotation number (i.e. Ro = 0.6) with Bo = 0 (top row) and Bo = 0.7 (bottom row). As it can be seen, the turbulence intensity is much higher in the boundary layers for the non-isothermal case, as it can be seen by comparing figures 6.9 (a) and (b) with figures 6.9 (c) and (d). In fact, higher levels can be found throughout the whole cross section. These figures allow also to highlight the stabilizing/destabilizing effect on the leading/trailing sides of the channel for either the isothermal and non-isothermal cases. As it can be seen by comparing figures 6.9 (a) and (b), turbulence intensity levels are always higher for the trailing side with respect to the leading side. The same conclusion can be drawn if figures 6.9 (c) and (d) are compared.

### 6.3.2 Inter-rib flow

#### 6.3.2.1 Static case

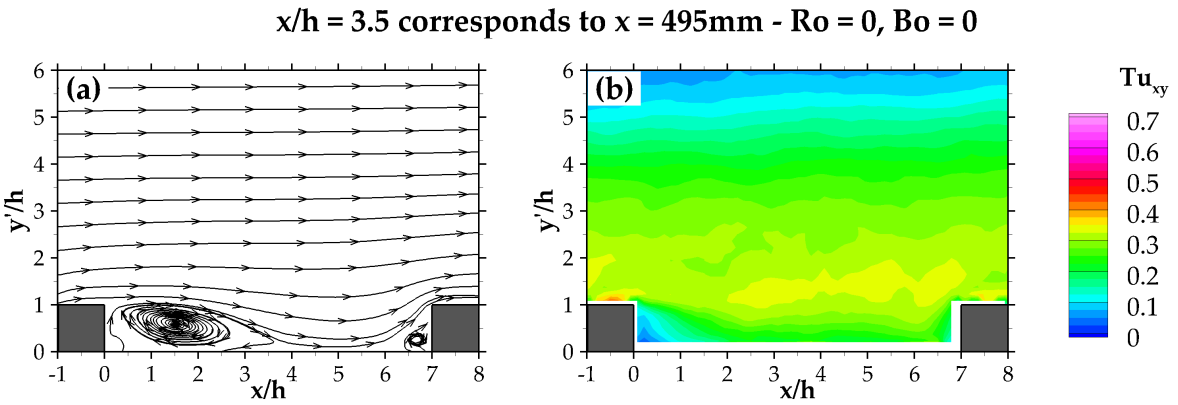


*Figure 6.10: Streamtracers (a) and $Tu_{xy'}$ contour plot in the interrib region, static case*

The investigation of the flow field between the turbulence promoters is of extreme importance for the assessment of the heat transfer properties of the channel.
In figure 6.10, the static case is reported. As it can be seen from figure 6.10 (a), the measured flow field is the typical one for this kind of turbulence promoters: a recirculating structure due to flow separation downstream the rib, flow reattachment at about 3.4h and another separation upstream the next rib, where the vena-contracta determines an acceleration above the rib.

Figure 6.11 reports the velocity and velocity fluctuations profiles extracted in correspondence of

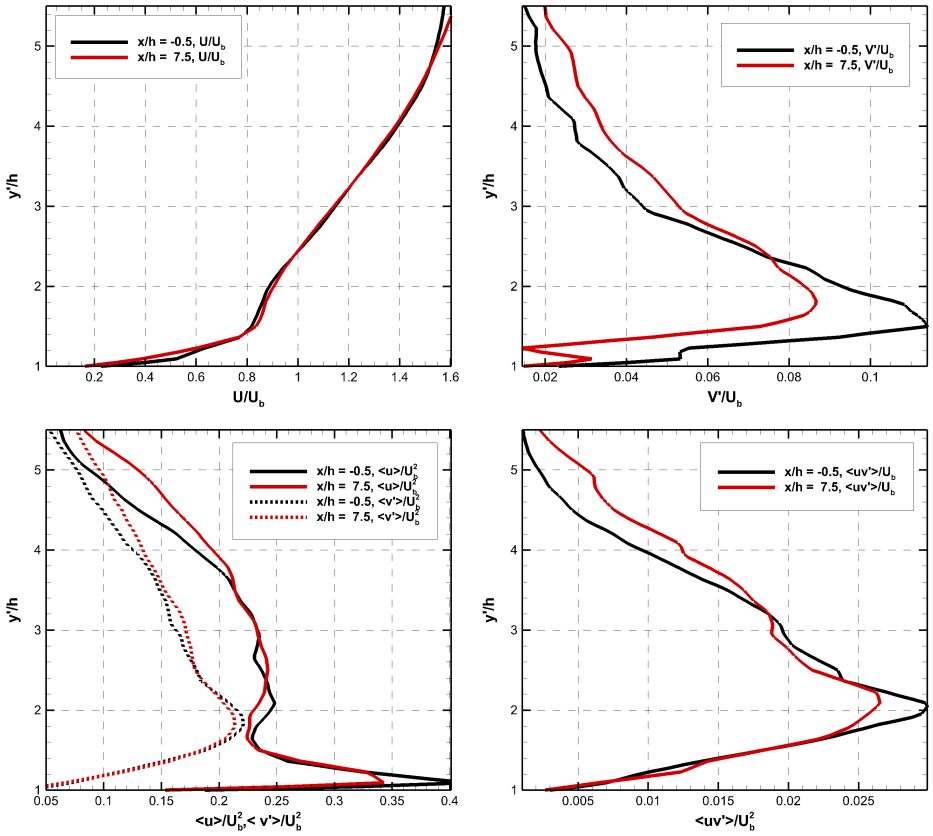


*Figure 6.11: Comparison between profiles extracted at homologous positions one pitch apart: (a) $U$ component, (b) $V$ component, (c) $u$ fluctuations, (d) $v$ and $uv$ fluctuations*

half rib length (i.e. x/h = -0.5 and x/h = 7.5) along $y'/h$, which is the direction perpendicular to the channel wall. As it can be seen, the two velocity components (i.e. $U/U_b$ and $V'/V_b$) as well as their rms quantities profiles extracted at homologous positions match in a satisfactory way. This means that the flow is fully developed and the periodicity is verified, hence the measurement zone is representative of the investigated problem.

In figure 6.10 (b) the turbulence intensity levels are reported. The distribution is typical for this kind of feature, with a turbulence injection from the trailing edge of the upstream rib and the shear layer between the recirculating bubble and the free stream expanding above it. As expected, the detected flow features are in agreement with those observed in a rectangular ribbed channel [35]. In the following, the results obtained for the rotating cases, both isothermal and non-isothermal will be presented. The discussion of the results will be made with a double comparison, involving both the other investigated cases (in order to highlight the Bo and Ro stabilizing/destabilizing effects,) and results available from the literature obtained in similar conditions (e.g. Bo and Ro) for the square channel. The data from the square channel are exploited

in order to highlight the differences between these two simple geometries.

#### 6.3.2.2 Isothermal rotating case

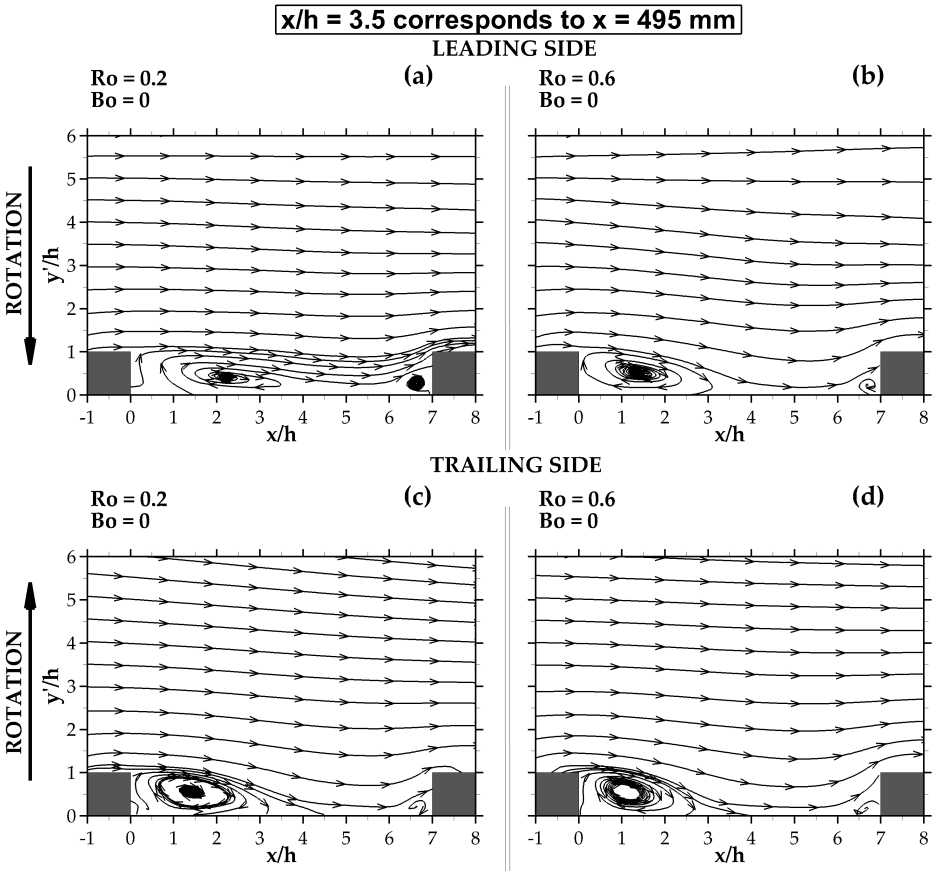


*Figure 6.12: Flow field for the isothermal case*

The time-averaged flow field results reported in figure 6.12 show the data obtained for the case at Ro=0.2 at the TS and LS. As it can be seen, at the trailing side, the flow field is not much influenced by rotation effects, in fact, the length of the recirculating structure is the same as in the static case (compare figure 6.10 (a) with figure 6.12 (c)). However, when the turbulence intensity levels reported in figure 6.13 are analyzed, a destabilizing effect on the shear layer can be clearly detected. In fact, comparing this levels with the one shown in figure 6.10 (b), it can be seen how in the zone of the shear layer the turbulence intensity is much higher, hence the flow mixing is enhanced accordingly to the literature [8].
On the other hand, at the leading side, an evident stabilizing effect on the shear layer can be already appreciated by comparing the recirculating bubble length with the static case. Considering the turbulence intensity contours reported in figure 6.13 (a), higher levels with respect the static case have been measured, in contrast with what can be expected since the presence of a clear

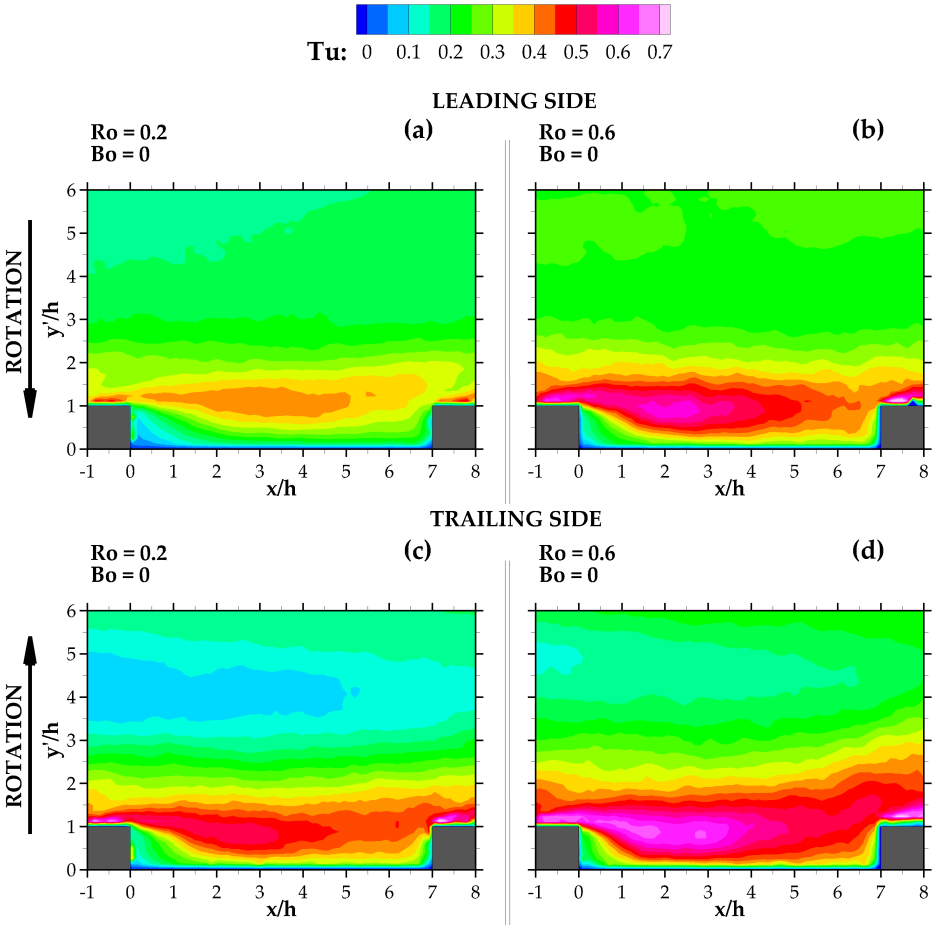


*Figure 6.13: Turbulence intensity levels for the isothermal case*

stabilizing effect (increase of the reattachment length). However, the turbulence intensity levels measured at the leading side are still lower than the one at the trailing side, meaning that the two zone experience different flow conditions.

These results are in partial agreement with the one from the square channel, in fact some differences can be highlighted. In the square channel, indeed, the difference between stabilizing and destabilizing effect on the leading and trailing side respectively, is rather more evident in both the flow field, and the velocity fluctuations (figures 2.6 (a-b-c) and figures 2.6 (d-e-f) in chapter 2.2). The former shows an evident shortening/increase in the reattachment length, while the latter shows an increase/decrease of velocity fluctuation with respect the static case. On the contrary, in the triangular channel, velocity fluctuations are always higher for tests under rotating conditions.

If the rotation number is increased to Ro = 0.6, the differences between the behavior of the flow field in the square and triangular channels become even more evident.

As far as the trailing side is concerned, the destabilizing effect becomes more evident with respect

the case at Ro = 0.2. As it can be seen in figure 6.12 (c), the recirculating structure shrinks to almost saturation, reaching a reattachment length of about 3h. This behavior is found also in the squared channel.
When the leading side is taken into consideration, the expected behavior would be a further increase in the recirculating bubble dimension, according to the trend showed by the flow field data in the rectangular channel. Instead, the length remains almost the same of the one for the case at lower Ro. The turbulence intensity contours reported in figure 6.13 show an increase in flow agitation with respect the case at Ro=0.2, with the trailing side more turbulent than the leading side, confirming what highlighted by the comparison between the static case and the one at Ro=0.2.

#### 6.3.2.3 Non-isothermal rotating case

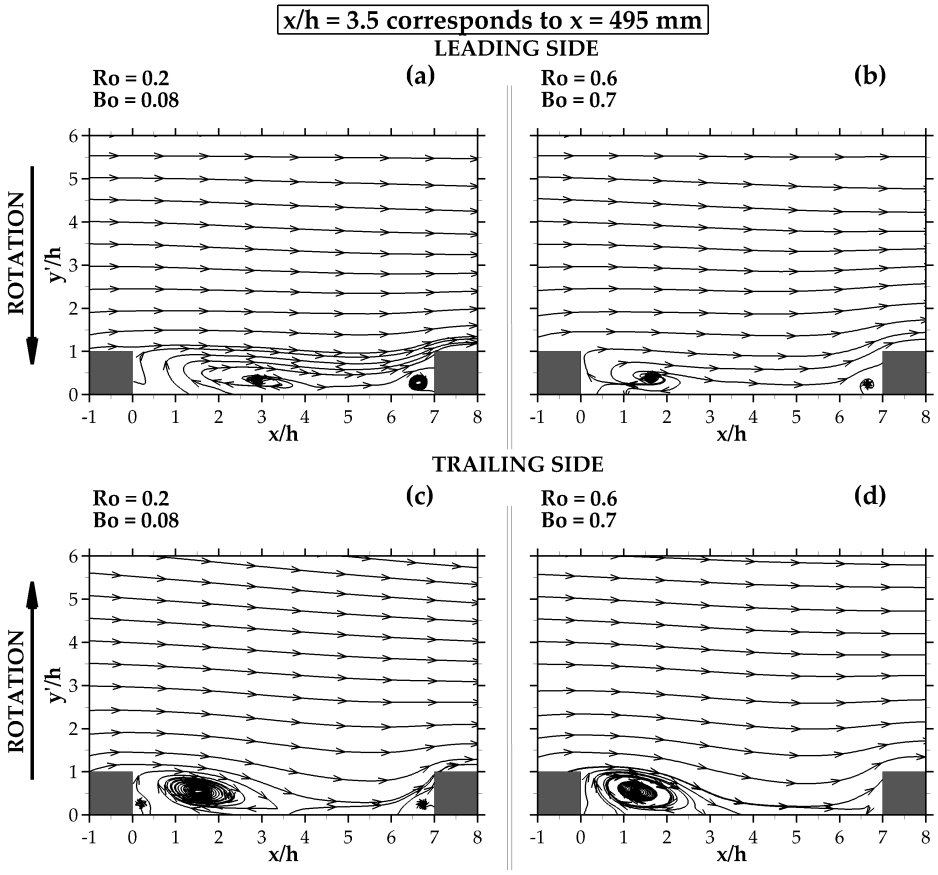


*Figure 6.14: Flow field for the non-isothermal case*

The results obtained for the trailing side with non-isothermal conditions (i.e. Bo>0), show an enhancement of flow turbulence. This behavior is particularly evident in figure 6.15 is compared to figure 6.13. As it can be seen, in fact, in the non-isothermal cases (Bo = 0.08 Ro = 0.2, Bo = 0.7

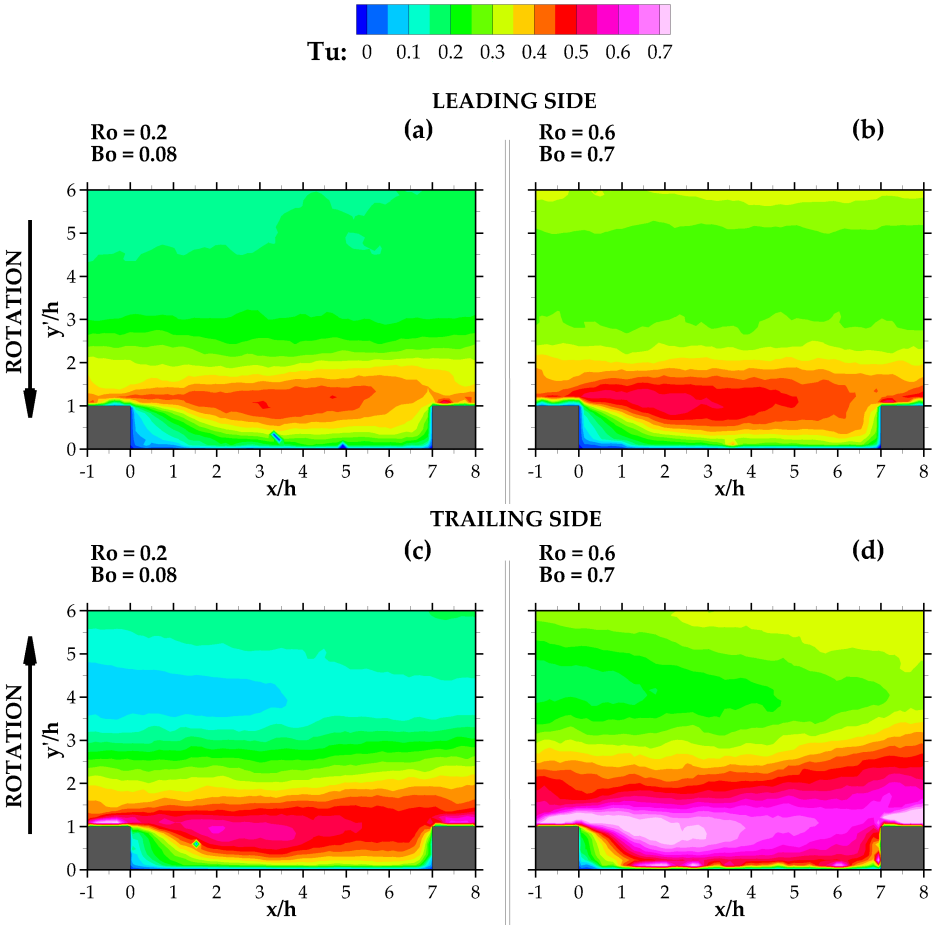


*Figure 6.15: Turbulence intensity levels for the non-isothermal case*

Ro = 0.6 in figure 6.15) the levels are higher with respect the relative isothermal cases (Ro = 0.2, Ro = 0.6 figure 6.13). Moreover, the case at Ro = 0.6 (and Bo=0.7) is characterized by a higher average level of turbulence intensity with respect the case at Ro = 0.2 (and Bo=0.08), consistently with what observed comparing the same cases at isothermal conditions. The flow field confirms the considerations made on the basis of the turbulence intensity contours. It can be observed in figure 6.14 (c) and (d) that the recirculating structure indeed is shorter with respect the correspondent isothermal cases.

The flow field behavior found at TS of the triangular channel is similar to the one reported for the square channel. Indeed, also in [10] an enhancement of the destabilizing effect is found, with the progressive shortening of the reattachment length as well as an increase of the velocity fluctuations with respect to the isothermal case.

On the leading side, the flow behavior is far more complex with respect the one found at the trailing side. The main difference that can be noted is that, while at the trailing side the buoyancy effect is the same for both rotation numbers, at the leading side it has an opposite effect depending

on Ro. At the lower rotation regime (i.e. Ro = 0.2) the trend followed by the flow field is the same commented for the comparison between Ro = 0 and Ro = 0.2. In fact, it can be seen that the reattachment is found further downstream with respect the isothermal case (compare figure 6.12 (a) and figure 6.14 (a)). Turbulence intensity levels confirm as well the trend found for the case at Ro = 0.2 and at the trailing side, indeed higher values are found for the case at Bo = 0.08 as it can be seen in figure 6.15 (a). When the case at higher rotation number is considered, an unexpected behavior is found as previously anticipated. The flow field reported in figure 6.14 (b) shows a recirculating structure with a complex topology, which does not allow to speculate about the reattachment length. Moreover, in the isothermal case, the turbulence intensity peak, found in the shear layer downstream the first rib, is higher with respect the case with Bo = 0.7. However, it has to be noted that this is only a local feature, in fact, the average

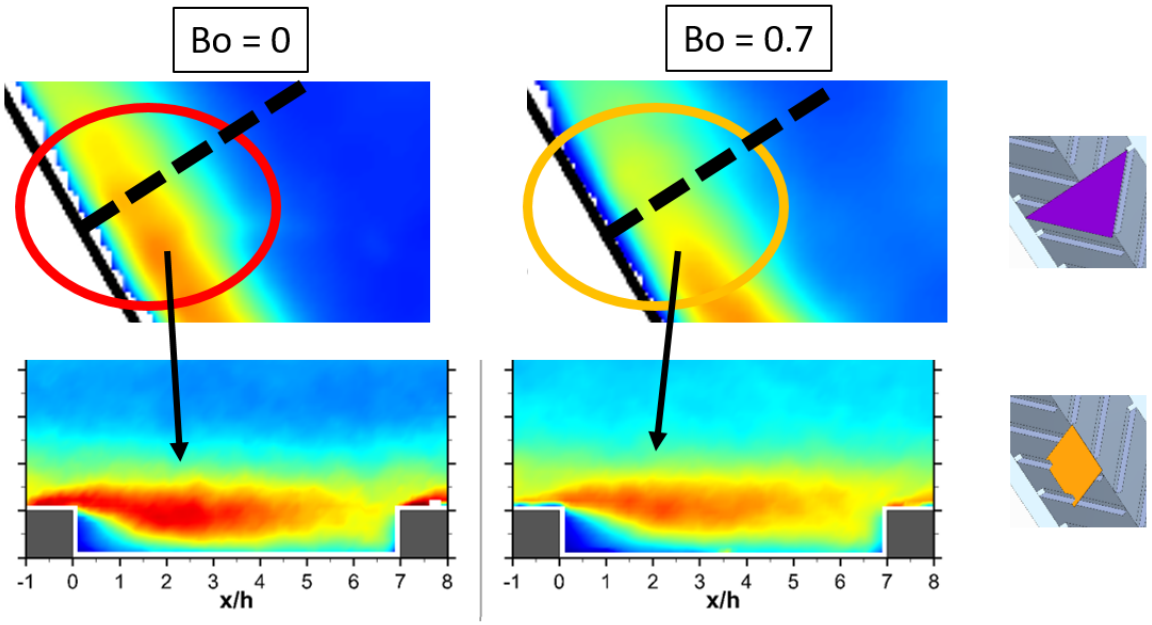


*Figure 6.16: Comparison between the cross section and the inter-rib region at the leading side for the cases at Ro = 0.6*

turbulence intensity level is higher for the case at Bo = 0.7. The proof of this consideration can be drawn from the comparison with the 3D data on the cross section. In figure 6.16 the position of the plane xy' is highlighted, and it can be seen that the turbulence intensity levels in correspondence of said plane are higher for the case with Bo = 0. However, figure 6.16 shows that this is only a local feature, while in fact, turbulence intensity levels are much higher for the non-isothermal case (i.e. Bo = 0.7) as it can be seen in figure 6.9 (c).

A quantitative comparison of the turbulence intensity throughout all the condition tested for both leading and trailing side is reported in figure 6.17, where the data extracted along the whole inter rib (i.e. x/h = 0-7) at $y' = 0.5$ are shown. As it can be seen by comparing figure 6.17 (a) and

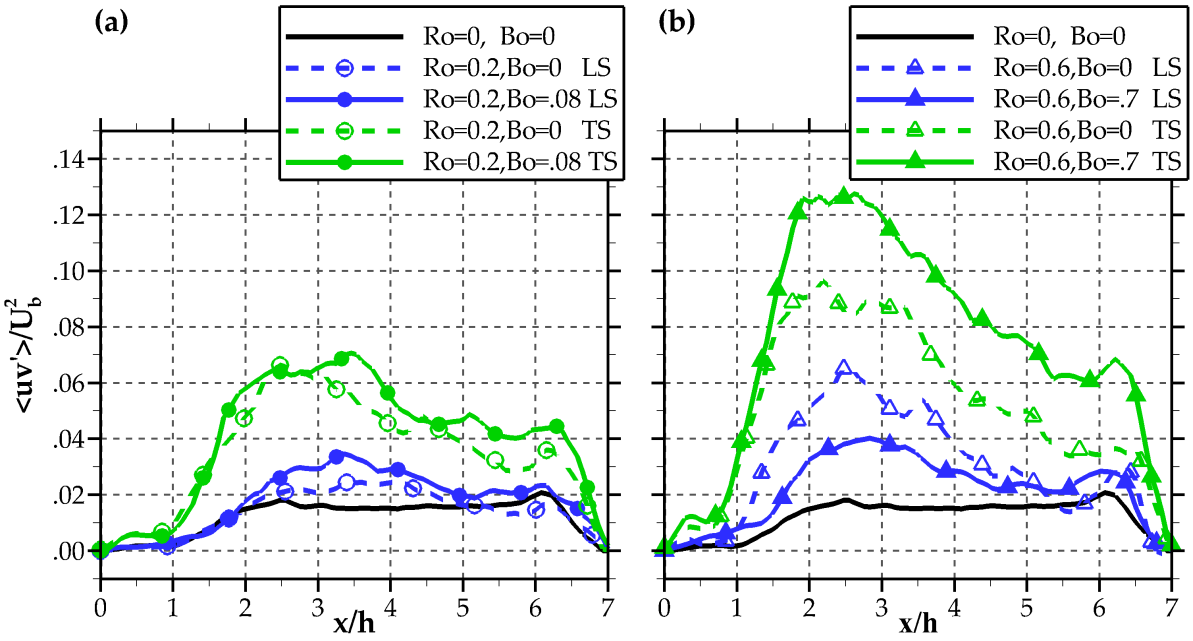


*Figure 6.17: Reynolds stresses component extracted at $y'/h = 0.5$ from plane xy', (a) static vs Ro = 0.2 and (b) static vs Ro = 0.6 test cases*

(b), buoyancy enhance the effect of rotation (exception made for the leading side, as commented before). Moreover, differently from the square channel, turbulence intensity levels of all rotating tests (both leading and trailing side) are higher with respect the static case and always lower at the leading with respect to the trailing side.

### 6.3.3 Remarks on the comparison between triangular and rectangular channel

The comparison between the two geometries had been carried out throughout the result discussion in order to highlight the profound flow field differences present even with extremely simplified geometries. A final remark will be made on the differences between the two planes where the measurements of the turbulent promoters recirculating structures had been made for the triangular and rectangular channel.

As it can be seen in figure 6.18, the investigation plane, for the rectangular channel, is both a symmetry plane for the geometry (even considering the ribs) and the secondary flow structures (sketched in green). Moreover, either it is positioned in a separation or a reattachment zone of the Coriolis' induced vortices, where the out of plane velocity is negligible. For this reason, trailing and leading side experience also a rather similar flow condition.

On the other hand, in the triangular channel, the measurement plane is not a symmetry plane for the cross section if the ribs are considered (gray rectangle) and the Coriolis' induced vortices

do not have a regular shape, hence the plane is not a symmetry plane also for the flow structures. For these reasons, as it can be seen in figure 6.18, the measurement plane is subjected to a cross flow condition that is opposite for the leading and trailing side. In fact, the near wall flow is directed upward for the leading side, while it goes downward in the trailing side. Moreover, as previously commented in section 6.5, the secondary flow is much stronger near the leading side than in the trailing side. These behaviors can explain the different topology of the recirculating structures downstream the ribs in regards of the different stream tracers rotating direction (leading side outward, trailing side inward).
The overall information obtained from the comparison between inter-rib and cross section planes suggests that the recirculating flow structures between the ribs are characterized by and extremely three-dimensional behavior.

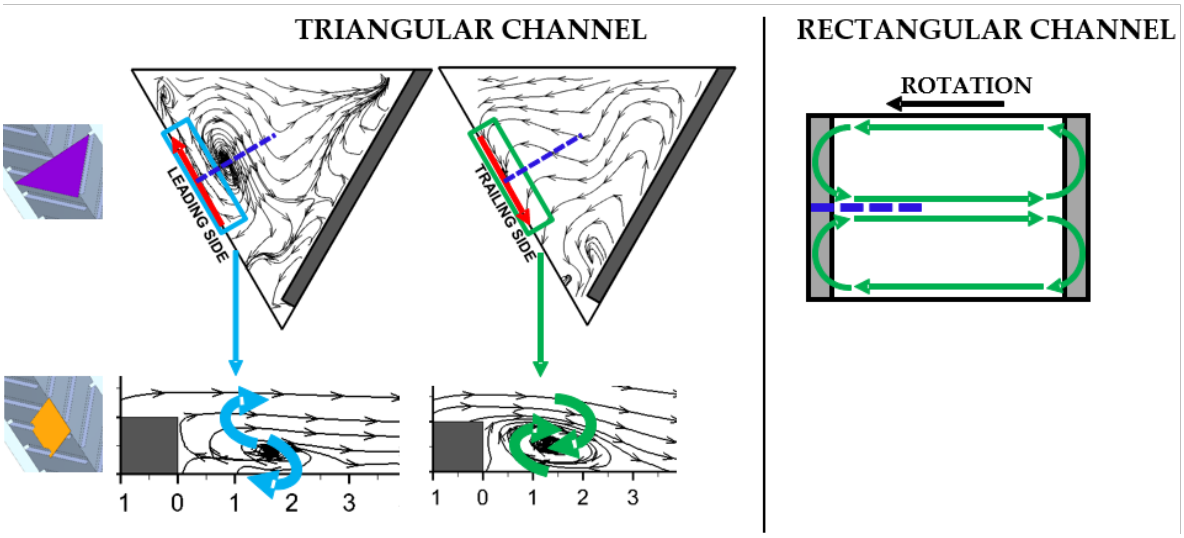


*Figure 6.18: Comparison between the position of the interrib plane in the triangular and rectangular channel. Highlight on the crossflow condition*

CHAPTER 7

# COMPUTATIONAL INVESTIGATION

Since the experimental activity highlighted an extremely complex flow field behavior both between the turbulence promoters and on the cross section, further data are required to confirm the conclusions drawn in section 6.3.3. As previously described in section 6.1, the test section architecture does not allow to perform PIV measurements on other relevant planes. Moreover, the three-dimensionality of the flow field would require a larger number of planes in order to completely characterize the flow field behavior. Thus, the effort required to obtain more data would not be adequately rewarded with the certainty of a deepen understanding of the aerodynamic behavior. For these reasons, it has been chosen to extend the analysis to the whole channel extension by means of CFD.

## 7.1 Numerical approach

The numerical procedure suggested by Pascotto et al. [13] has been applied to provide accurate simulations using the commercial solver Fluent v.15. The overall computational domain is portrayed in figure 7.1 (a). Since the experimental setup did not allow velocity measurements at the test section inlet, the following approach was followed in order to correctly impose the boundary conditions of the investigated domain. A multi-block structured mesh with hexahedral elements was used to discretize the triangular channel, together with the upstream settling chamber and the downstream exhaust duct. The whole test rig was modelled using a reasonable number of cells (approximately 4.6 million) for two reasons: on the one hand, 2D maps of U, V, W velocity component were extracted just downstream of the honeycomb filter (see blue slice in figure 7.1 (a)), on the other hand, it was verified that the static pressure distribution at the channel outlet is not significantly affected by the presence of the exhaust duct. Finally, for the actual computation of

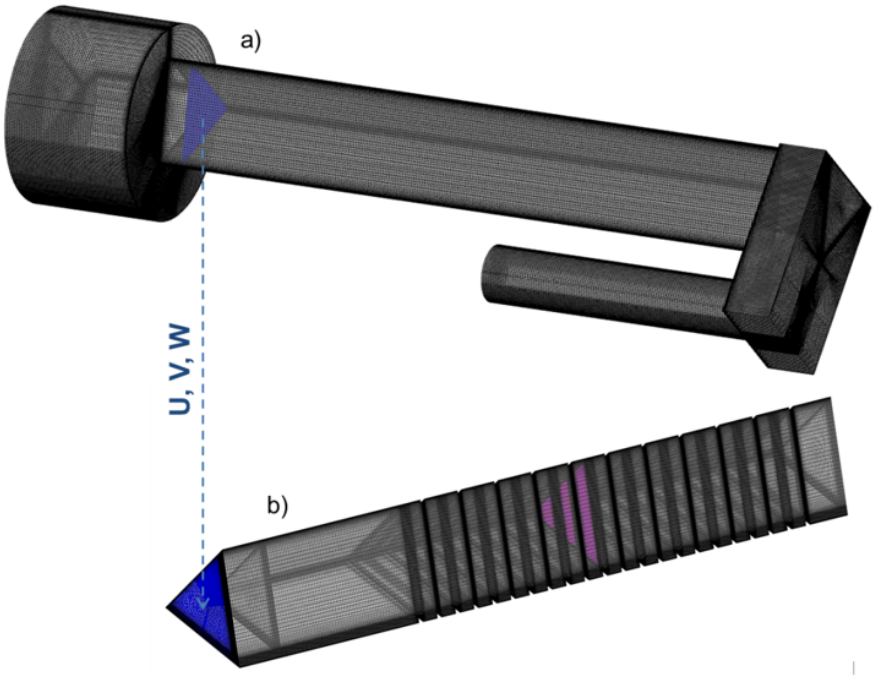


*Figure 7.1: Numerical domain: (a) overall test rig and (b) triangular ribbed channel*

the flow field, the domain was restricted to the triangular channel shown in figure 7.1 (b), and the velocity maps obtained from the previous simulation were applied as inlet conditions (blue slice in figure 7.1 (b)). For the final domain, grid independence was evaluated through progressive refinement. A base grid of 7.58 million cells, ensuring y+ lower than 0.85, was further refined close to the walls. The fine grid consisted of 9.35 million cells, with maximum y+ of 0.55. A section between the 5th and the 6th rib of the leading side (see pink slice in figure 7.1 (b)) is shown for both grids (figure 7.1). The base grid was found to provide sufficient resolution since base and fine mesh results were in close agreement. A difference of less than 4.2% between monitor variables, such as velocity magnitude along dotted lines of figure 7.2, was gained when comparing results from both grids, at Ro = 0.2 and Bo = 0.

The solutions were obtained by solving the uncompressible steady RANS equations. Air flow enters the channel at room temperature (293 K). When dealing with buoyancy, the ribbed wall temperature was set at 383 K to match the experimental conditions. The classical second order scheme was adopted. For turbulence modelling, the $\kappa - \epsilon$ model was employed in combination with the enhanced wall treatment. Other available turbulence models with similar computational cost did not produce any results in better agreement with the experimental data. This is not new for leading edge cooling channel [36].

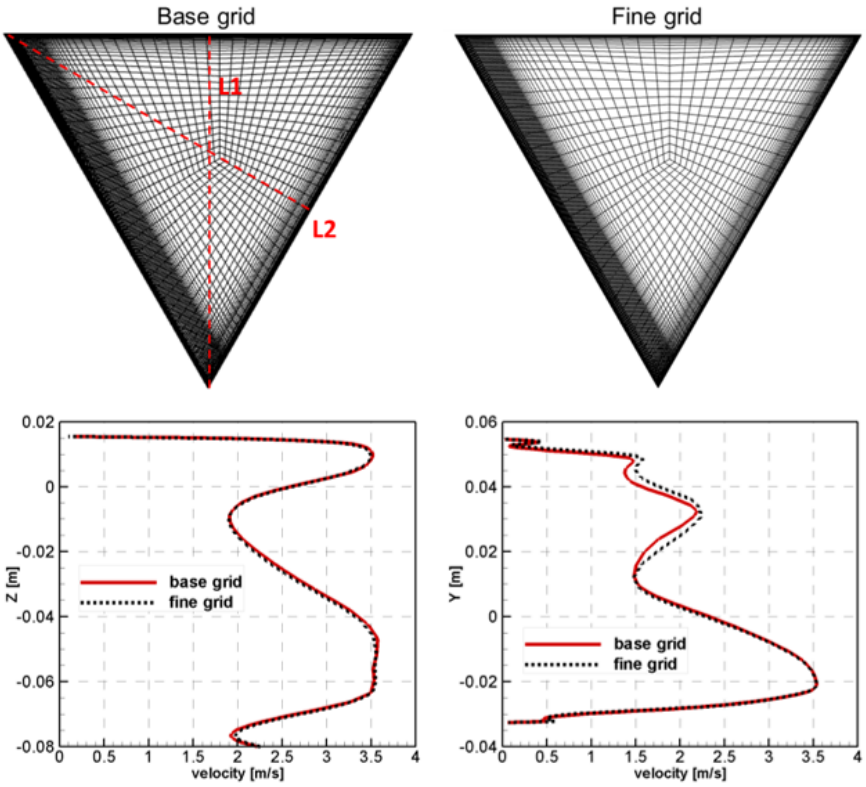


*Figure 7.2: Top row: grid section; bottom row: velocity profiles along L1 (left) and L2 ( right) for base and fine resolution, at Ro = 0.2 and Bo = 0*

Convergence was assessed by monitoring residual levels and local values of velocity. Moreover, the evolution of the simulated flow along the channel was kept in check. The $\kappa-\epsilon$ turbulence model was able to develop the correct periodicity of the separated region downstream of the rib. Validity of predictions was also proven by comparing measured and simulated velocity profiles within the channel, as shown in figure 7.3. Both U, V velocity profiles extracted perpendicularly to the leading side match the S-PIV experimental data quite satisfactorily, for the investigated condition of Ro = 0.2 and Bo = 0. Additional evidence on the good agreement between numerical and experimental data will be provided in the section below.

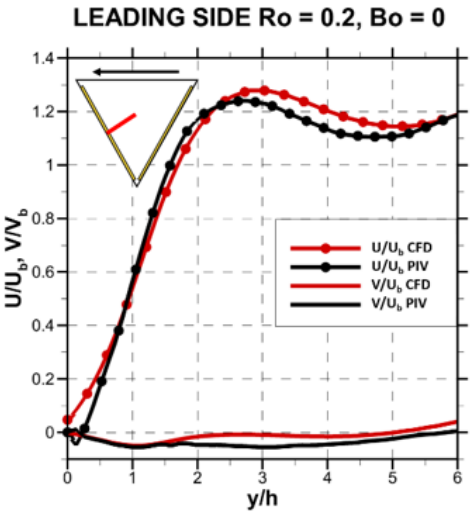


*Figure 7.3: Example of CFD validation at Ro = 0.2 and Bo = 0*

## 7.2 Results

### 7.2.1 Core flow

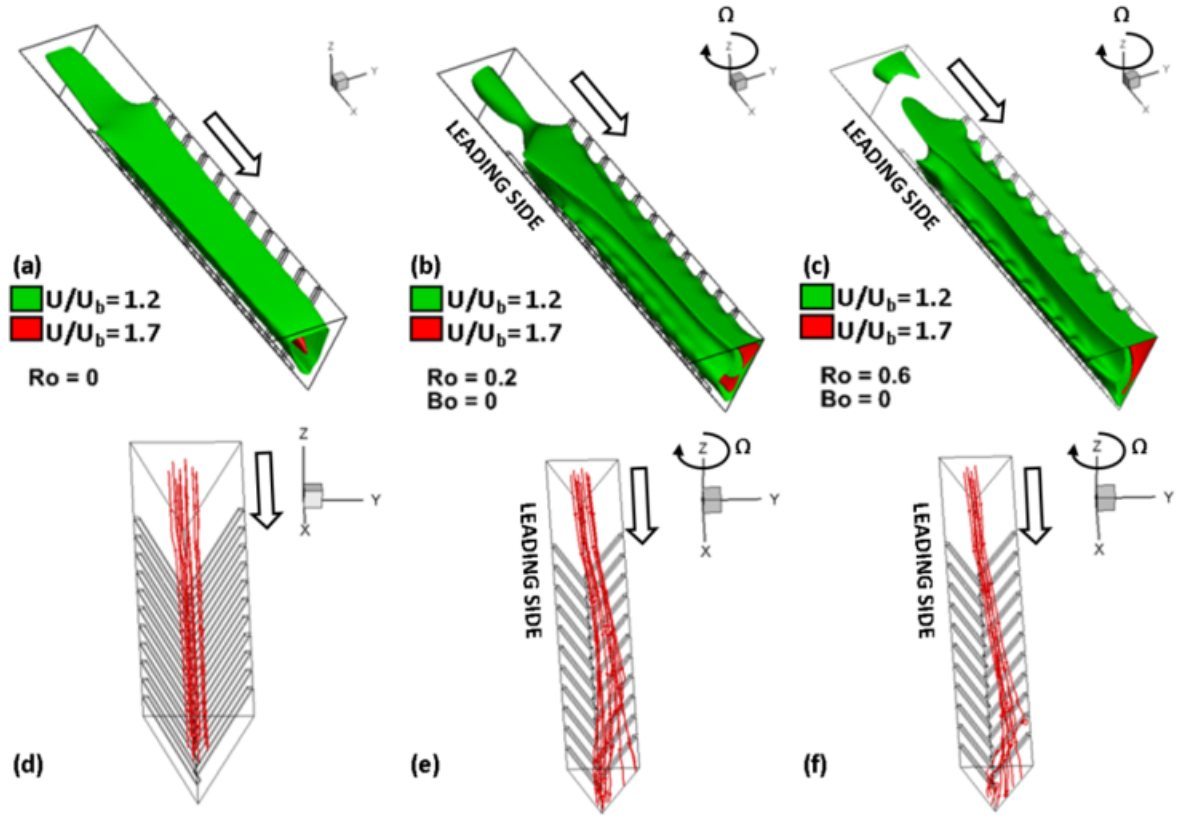


*Figure 7.4: Core flow iso-surfaces and stream tracers*

Plots in figure 7.4 provide a first look at the core flow behavior, by means of U velocity component iso-surfaces and stream tracers along the channel extension. For the static case (figures 7.4 (a) and (d)), after the initial smooth part of the channel and downstream of the first pair of ribs, the core flow expands immediately throughout the cross section. Moving further downstream along the channel, no substantial modification to the core flow extension can be appreciated. When rotation occurs, a profound change in the core flow evolution is manifested. For both rotating conditions (figures 7.4 (b) and (c)), a displacement of the higher velocity zone (colored red) towards the trailing side can be seen, associated to the formation of a velocity deficit near the leading side top apex. This feature is well highlighted by the 3D stream tracers plots of figure 7.4 (e) and (f), where the core flow displacement can be clearly seen, combined with a following expansion that spreads the high momentum flow through the whole trailing side. This behavior entails the local increase in the Reynolds number in both lower and trailing edge top apices.

It is also worth noting that the core flow settles in a definitive configuration after a limited

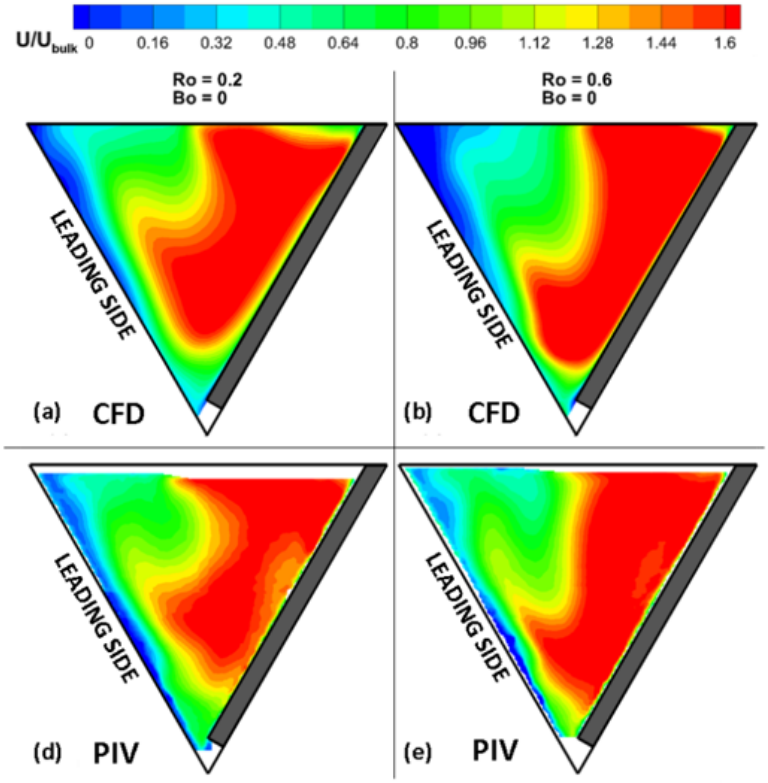


*Figure 7.5: Numerical (a) and (b) and experimental (c) and (c) bulk velocity contours.*

number of rib pitches. The definitive velocity distribution, between the 5th and the 6th rib of the leading side, can be seen in figure 7.5. A good agreement between the numerical predictions and the 3D velocity data from S-PIV was found for both rotation parameters, thus confirming the reliability of the present CFD modelling.

### 7.2.2 Near wall flow

Turbulent promoters perpendicular to the main flow velocity, besides disrupting the boundary layer development, do not introduce significant near wall mass transportation. Indeed, at Ro = 0, positive (colored red) and negative (colored blu) iso-surfaces of W-velocity component provided in figure 7.6 (a) show that the inter-rib region is interested by low velocity, mostly pushing the coolant towards the upper wall (positive W velocity). This weak transportation motion is probably due to the blockage effect of the ribs in the lower apex region.
When rotation occurs, the flow is characterized by negative W near the trailing side whereas positive W velocities are found near the leading side, as it can be seen in figures 7.6 (b) and (c). Moreover, this transverse motion is characterized by much higher velocity than in the static

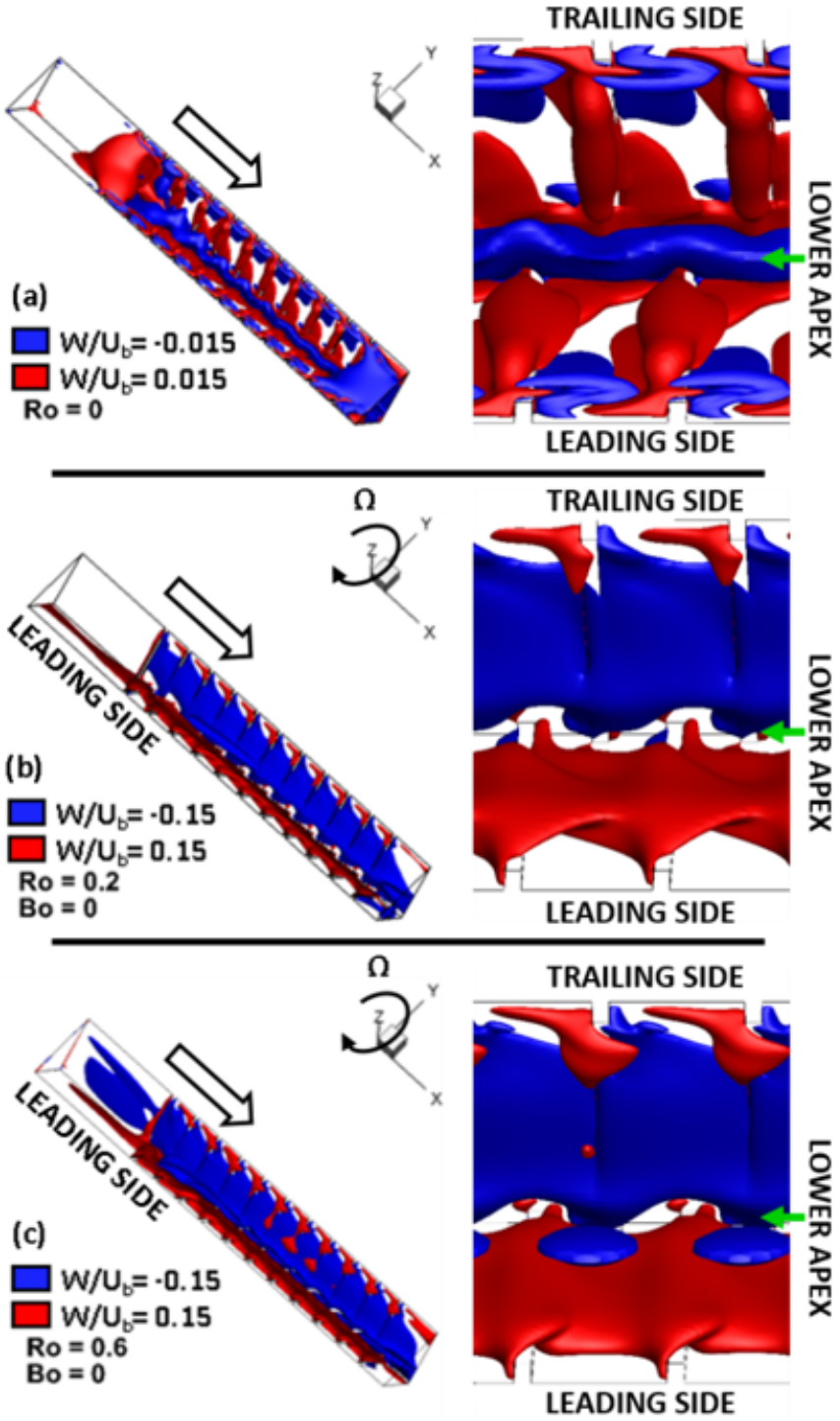


*Figure 7.6: Near wall flow iso-surfaces (Bo = 0): (a) stationary, (b) Ro = 0.2 and (c) Ro = 0*

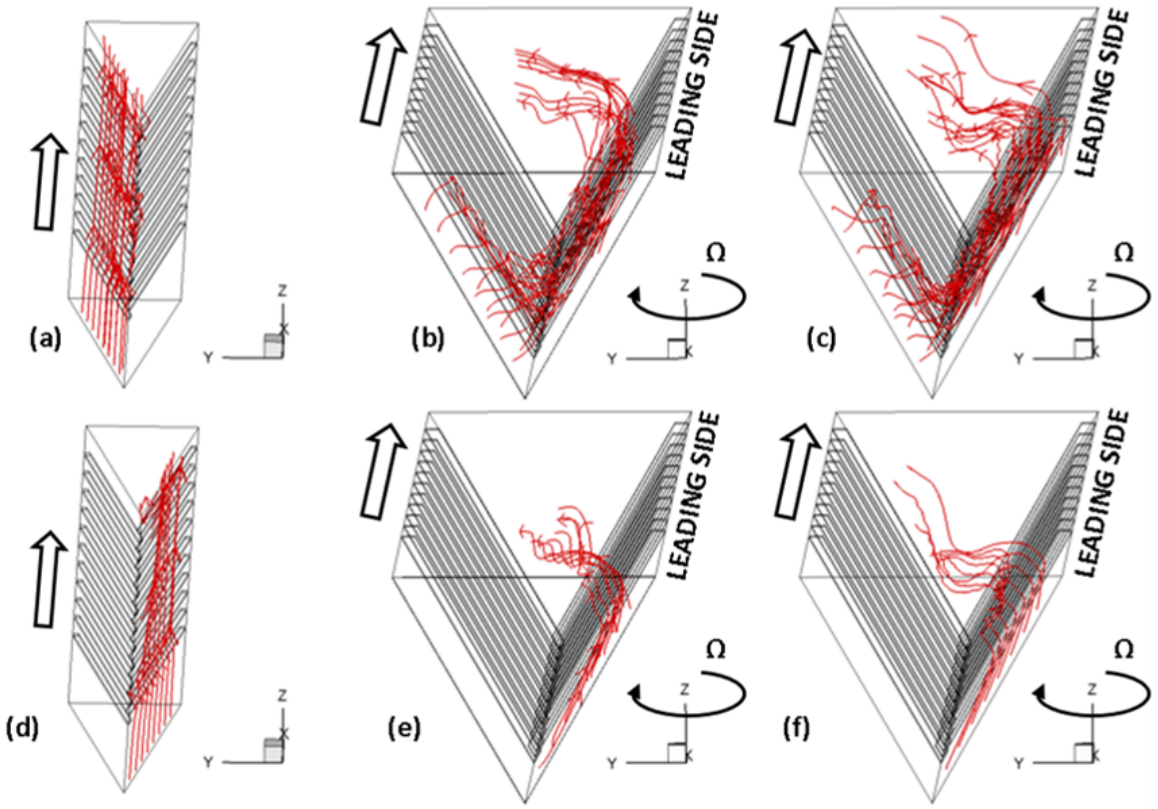


*Figure 7.7: Trailing (a-c) and leading (d-f) side boundary layer stream tracers (Bo = 0): (a), (d) stationary, (b), (e) Ro = 0.2 and (c), (f)) Ro = 0.6*

case. In fact, the iso-surfaces in figures 7.6 (b) and (c) are representative of velocities an order of magnitude higher than those plotted in figure 7.6 (a).

Additional information about the near flow behavior may be drawn from the analysis of the stream tracer path. In particular, figure 7.7 shows the trajectory of the fluid particles along the channel starting from either the trailing side boundary layer (figures 7.7 (a, b, c)) or the leading side one (figures 7.7 (d, e, f)). In static condition (figures 7.7 (a) and (d)), the near wall flow remains confined in proximity of the pertaining wall. Conversely, rotation sets a 3D motion of the boundary layer flow. As it can be appreciated in figures 7.7 (b) and (c), the near wall flow developing along the trailing side is eventually pushed towards the lower apex and afterwards climbs the leading side. Here the near wall flow travels towards the channel center immediately after passing few rib pitches (figures 7.7 (e) and (f)). These observations, being entirely consistent with the above analysis based on the iso-surfaces of W velocity, explain the genesis of the velocity deficit in the core flow highlighted in figures 7.4 (b) and (c).

The described near wall flow behavior has rather important influence on the recirculating structures between the turbulent promoters. In figure 7.8, stream tracers colored by W-velocity

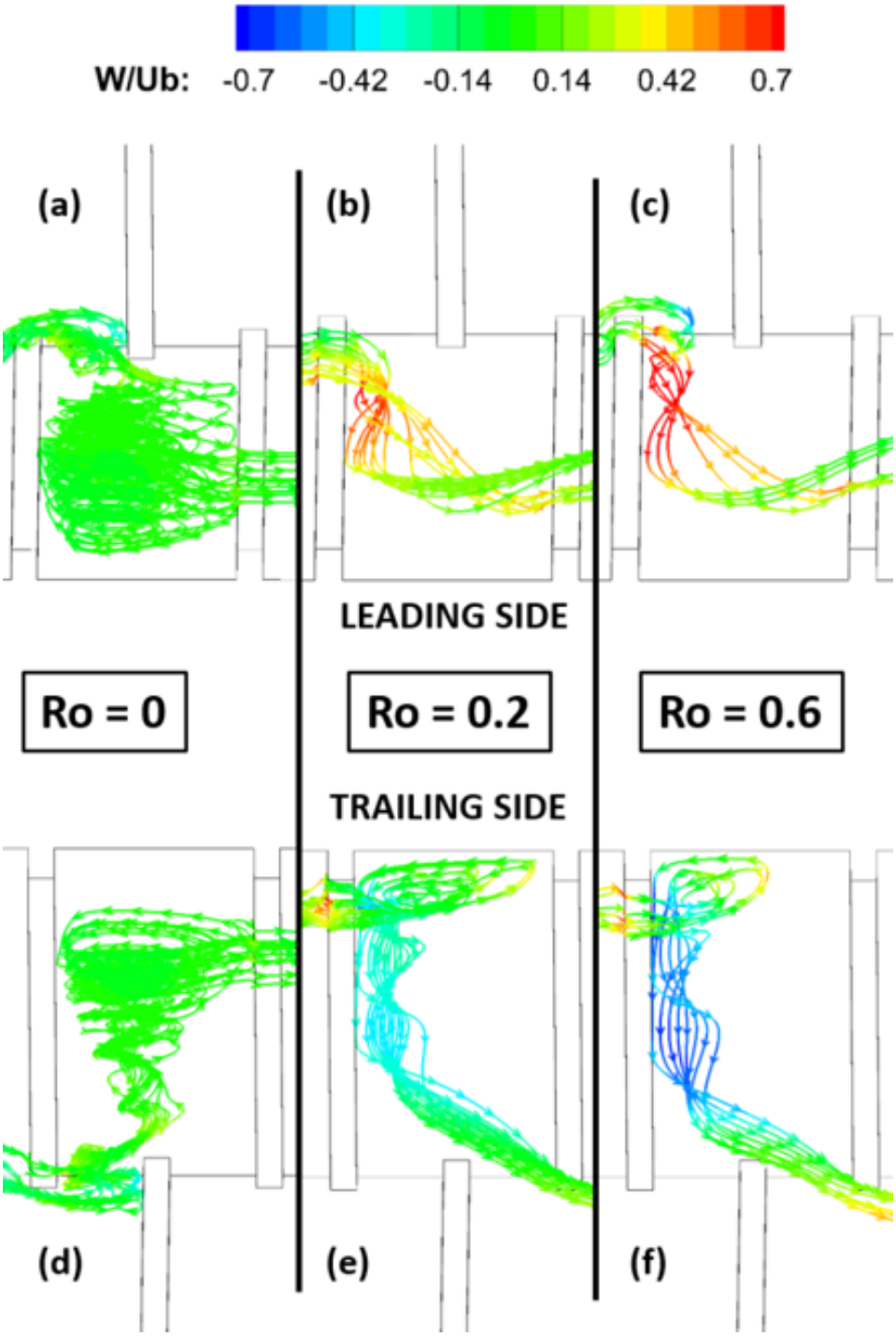


*Figure 7.8: Recirculating structures between turbulence promoters.*

component help point out the complex helicoidal structure of the recirculating bubble inside an inter-rib space (between 5th and 6th rib of the leading side), as well as its development along the rib.
In static condition (figures 7.8(a) and (d)), the separation structure shows uniform W velocity along the whole rib width. A slight motion of the flow is observed from the lower apex towards the upper one on both trailing and leading side, accordingly with the already mentioned blockage effect of the ribs on the lower apex. In this region, the local increase of blockage has also a clear influence on the separation dimension: the rib pitch is virtually halved.
Under rotation, an intense flow migration is detected and the separation structures become strongly 3D. Flow moves from the top of the channel towards the lower apex on the trailing side and vice versa on the leading side (as already noticed in figure 7.6(b) and (c)). Moreover, these complex structures suggest that the distance of the reattachment point from the rib wall is not constant along the rib width. These results confirm the speculations made in chapter 6.3.2 where measurements have been performed on a plane perpendicular to both the channel wall and the ribs width. In addition, the flow separation extension was found to vary significantly with rotation and channel side (i.e. leading or trailing side). This finding confirms what could be only hypothesized with the experimental data, since PIV measure did not provide a definitive proof of the three dimensional behavior of the flow field between the ribs. Actually, the reported results show that the separation structure surrounding the ribs, inside the triangular rotating channel, is intrinsically three dimensional and too complex to be simplified by means of a 2D scheme, as attempted in [1].

### 7.2.3 Flow evolution

The CFD simulations allow to investigate the flow field in the whole channel, hence to characterize the evolution of Coriolis' induced secondary vortices along the channel radial extension. Since the rotation effects are extremely complex, it is worth starting the discussion with the description of flow field evolution along the smooth channel.
Figure 7.9 reports the predicted stream tracers and stream-wise velocity distributions in five yz planes, at Re=20000 and Ro=0.4, without internal ribs [13].
An unexpected flow behavior with the appearance of a third vortex cell near the top-right corner (C2 in figure 7.9 (a)) came out of the simulations. In order to understand the physics behind the development of this vortex structure, the evolution of U and V velocity components along the blue line in figure 7.9 (a), which refers to a point on the channel cross section at y = 38 mm, z = 24 mm, was reported in figure 7.9 (b). Coriolis induced structures determine the formation of a low velocity zone near the leading side top apex due to the transportation of low momentum flow from the boundary layers. The counter rotating cell named C2 forms when the velocity in the leading side top apex reaches values comparable with those in the boundary layer (it happens more or less at section S2). The formation of the C2 cell is accompanied by the insurgence of a

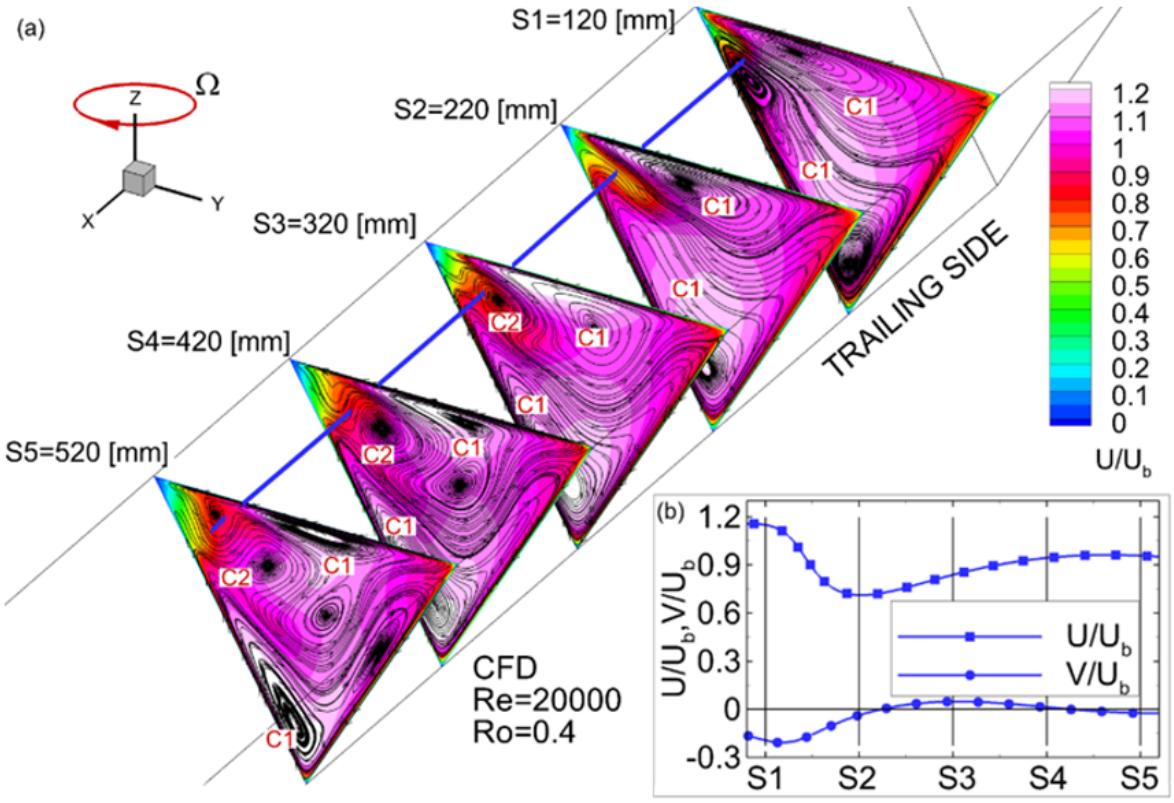


*Figure 7.9: Contour maps of stream-wise velocity and stream tracers at different channel locations: (a) evolution along the smooth channel of the stream-wise and span-wise velocities at point y=38 mm, z=24 mm (b) CFD data at Re=20000, Ro=0.4, extracted along the blue line [13]*

component of the Coriolis force aligned with the radial direction (due to the positive V velocity component of the flow in the cell) that causes the increase in the U component and therefore the dissipation of C2. The flow field evolving along the channel never reaches a stable configuration because of generation and successive dissipation of C2. Note also that the flow evolution along the channel is faster for higher rotation numbers [13].

The same analysis has been conducted for the ribbed channel (figure 7.10). Stream-tracers are superimposed to U velocity contours in seven cross sections, for both rotation parameters. The selected cross sections were located in correspondence to the ribs. In figure 7.10 (a), the flow pattern in section S1, which is located at the end of the inlet (smooth) region, is significantly different from that in other sections. This is due to secondary flow structures developing into two counter rotating vortices, as extensively described in [13]. Comparing cross sections S1 for the cases at Ro = 0.2 (figure 7.10 (a)) and Ro = 0.6 (figure 7.10 (c)), it is possible to appreciate how the increase in Ro affects the development of the aforementioned secondary structures, thus leading to a more complex configuration with more than two vortex cells, as reported in [13] for

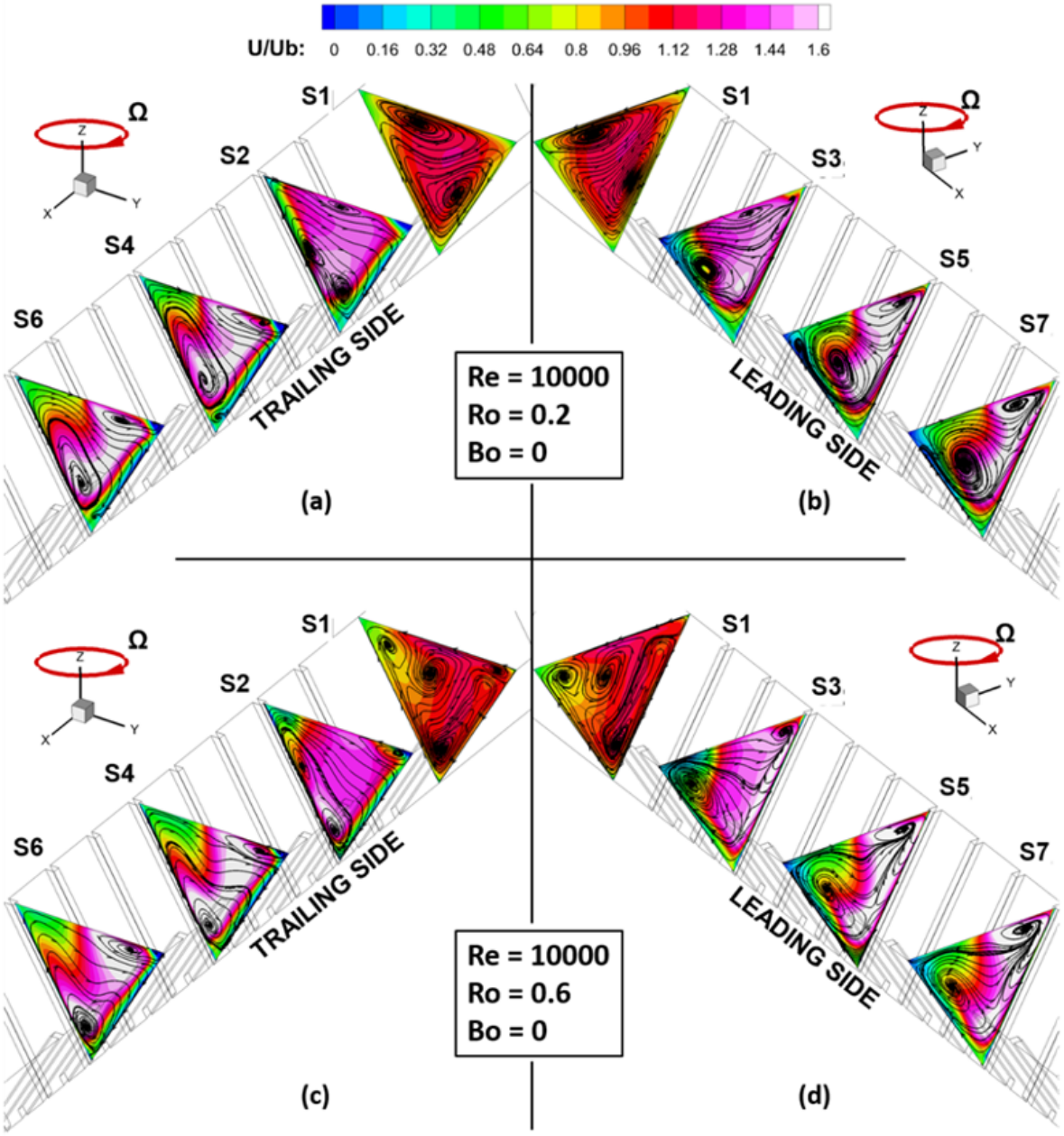


*Figure 7.10: Flow evolution along channel radial extension*

the smooth channel case.
Drawing attention to cross-sections downstream of S1 for the case at Ro = 0.2 (figures 7.10 (a) and (b)), it can be noticed that the topology of secondary flow structures is mostly affected by the presence of the ribs, with no significant variations along the channel length. This is also true at Ro = 0.6 (figures 7.10 (c) and (d)), even though the flow pattern at the end of the inlet region differs from that of lower Ro.
The most interesting difference between the flow behavior on trailing and leading sides deals with the impact of the turbulence promoters on secondary flow structures. The presence of a rib on the trailing side yields to a noteworthy acceleration of the flow and results in the formation of a separation line, parallel to the trailing side, lying between the accelerated flow and the secondary flow structures (figures 7.10 (a) and (c)). Conversely, on the leading side, neither separation line nor vortex distortion can be detected due to the lower velocity levels that characterize the LS under rotation (figures 7.10 (b) and (d))).

### 7.2.4 Buoyancy effect

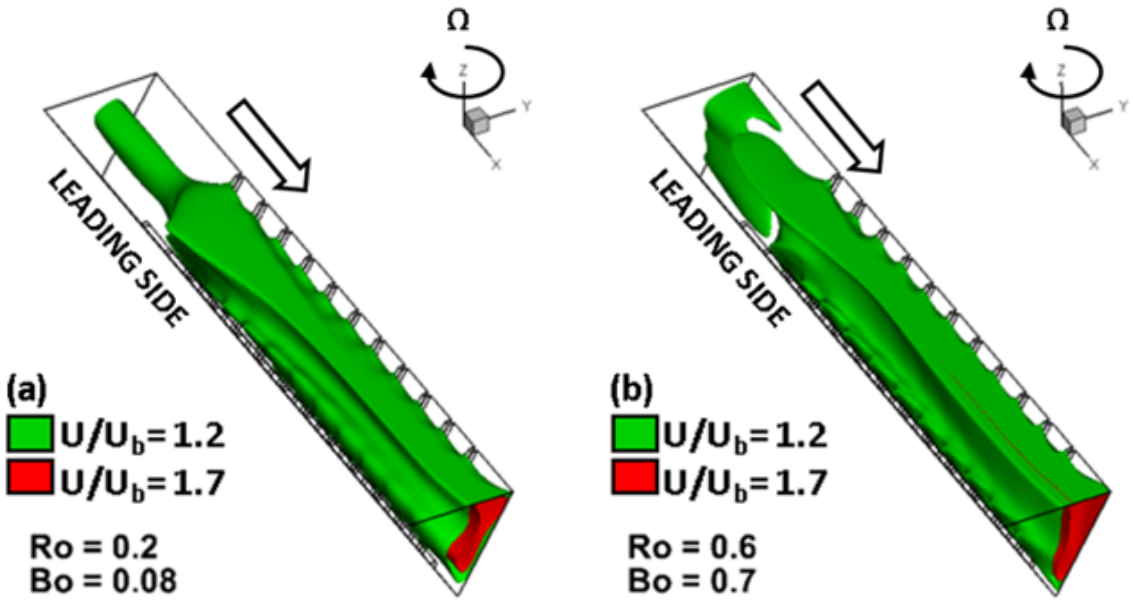


*Figure 7.11: Core flow iso-surfaces and stream tracers, with buoyancy effect*

Concerning the effect of buoyancy forces, simulations have been performed with Bo = 0.08 (Ro = 0.2) and Bo = 0.7 (Ro = 0.6). The core flow evolution along the channel, depicted by iso-surface of $U/U_b$, has roughly the same features as the isothermal cases (see figures 7.11 (a) (b) vs. figures 7.11 (b) and (c)). Nevertheless, a wider extension of the core flow seems to be

the only relevant feature of buoyancy (in this geometry), according with the numerical results. Experimental data shown in figure 6.15 of section 6.3.2.3 document turbulence augmentation inside the near wall zones due to buoyancy forces. This effect was confirmed by the present simulations but the limitation imposed by the isotropy assumption of the turbulence model suggested avoiding further speculation about this aspect.

CHAPTER 8

# COMPARISON WITH AVAILABLE THERMAL DATA

One of the main reasons for the choice of this simplified geometry (i.e. triangular equilateral cross section, striaght channel without bleeding holes) had been the availability in the open literature of thermal data on the same geometry [1]. As already stated in the introduction, the characterization of a geometry in terms of thermal behavior only is limited to the investigation of the effect (distribution of heat transfer coefficient), without the understanding of the cause (flow field). In the following discussion, it will be highlighted the connection between flow field features and heat transfer distribution.
Some differences can be found in the entry channel section but this does not affect the validity of the considerations hereafter proposed. Indeed, the aim is to provide a possible explanation about the observed behaviour of the thermal field under rotation based on the present aerodynamic data. Therefore, one should not look at the exact values of the Nu or enhancement factor data, but try to find the link between the flow and thermal field evolution while going into rotation.
Available data from [1], among the many rib configurations and test conditions, include the heat transfer enhancement factor throughout the channel length at rotational speed n = 400 rpm (Ro=0.58), for two different Reynolds numbers (i.e. 10000 (a) and 30000 (b)) for the configuration with 90° rib, as reported in figures 8.1 (a) and (b). The Nu is the result of wall temperature measurements performed in the experiments while $Nu_0$ is the one obtained from the Dittus-Boelter correlation and $Nu_s$ refers to the static channel case. The following analysis will be based only on the CFD and 3D data on plane yz from the PIV measurements, since plane xy' is located just in between of the L1/L2 or T1/T2 zones defined in [1]. L1/T1 refer to the half portion of the leading/trailing sides close to the lower apex while L2/T2 pertain to the upper half of leading /trailing sides close to the upper apices.
In static conditions, the channel withstands uniform heat transfer (both through the cross section

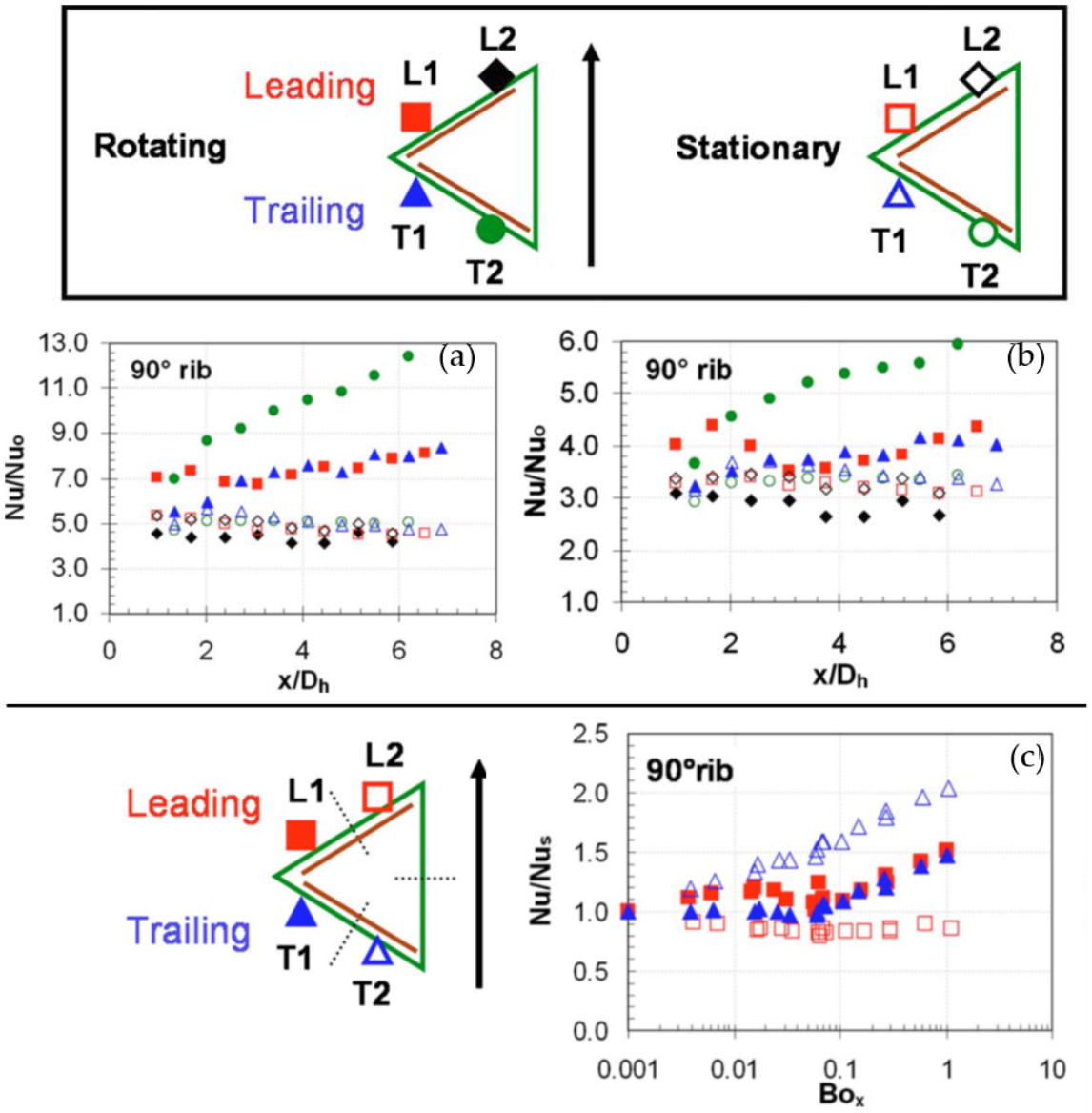


*Figure 8.1: Nusselt number ratio distribution in the rotating channel: (a) Re = 10000, 400 rpm (Ro=0.5), (b) Re = 30000, 400 rpm (Ro=0.2) and effect of buoyancy parameter on Nusselt number ratios at $x/D_h$ =4.11 (c) from Liu et al.[1]*

and along the radial extension). However, when rotation occurs, the four highlighted zones are characterized by different levels of $Nu/Nu_0$, proof of the importance of the secondary flow structures discussed in chapter 6.3 and 7.2.
As far as the trailing side top apex (i.e. T2) is concerned, the heat transfer enhancement is always higher with respect to the static case due to the displacement of the core flow and consequent local acceleration of the flow. Moreover, it increases along the channel due the progressive increase in the velocity peak. The lower apex zones (i.e. L1, T1) show much lower Nusselt number ratios than T2. The reason has to be ascribed to the near wall flow that drives coolant from the trailing side top apex T2 downward, thus T1 and L1 experience hotter fluid than T2. Furthermore, L1 and T1 exhibit different trends at the beginning of the channel. In fact, the L1 heat transfer enhancement is higher than that in T1 within x/Dh < 3 whereas, at about x/Dh = 3, it reaches levels comparable to those of T1. The reason for this may be related to the strengthen of the aforementioned near wall flows, with respect to the initial part of the channel. At x/Dh > 3 no difference in the overall trend of $Nu/Nu_0$ between L1 and T1 can be detected, because no major modification in the secondary flow structures occurs at increasing x/Dh.
At the leading side top apex L2, values of heat transfer enhancement in rotating conditions are lower than for the static case, whatever x/Dh is considered. This is due to the near wall flow, which drives fluid coming from the boundary layer of the trailing side to L2 region. Such fluid transport has a detrimental effect on heat transfer: on the one hand, it causes a velocity deficit, hence a local Re decrease; on the other hand, hotter fluid is available for cooling, as compared to other regions.
This flow behaviour, as previously commented in section6.3.1.1, becomes even stronger if the Ro increases, and consistently does the enhancement factor from [1] (compare data in figure 8.1 (a)-higher Ro, with those in figure 8.1 (b)-lower Ro).
Concerning the Bo effects, [1] shows an overall positive effect, with the highest increment of heat transfer again located in region T2, as indicated in figure 8.1 (c). Indeed, as demonstrated by the experimental data, the effect of buoyancy is an overall augmentation of the turbulent agitation of the flow (figure 6.9), in particular on the TS. On the contrary, in region L2 this effect is much less pronounced and the turbulent quantities remains practically unchanged at varying the Bo, consistently with the existence of the low momentum Coriolis vortex cell above commented. ++

# Part IV

# ADVANCED LEADING EDGE COOLING SYSTEM

CHAPTER 9

# TEST ARTICLE DEVELOPMENT

The activity pertinent to the investigation of the flow field features in the advanced leading edge cooling system required two major phases: the design of a test section that allowed to control many variables (e.g. the mass flow rate split between jets and bleeding holes) and the actual experimental activity.
The geometry subject of the investigation is presented in figure 9.1, where it can be appreciated as a 3D CAD model. The relevant features that characterize this geometry are:

- Jet impingement
- Film cooling holes: four rows, one for pressure and suction side and two for the shower-head
- Realistic geometry features: rounded apex, fillet on the jet holes upstream face, racetrack holes
- Mass flow extraction at the tip of the test section

The test section is characterized by a trapezoidal channel, called feeding channel, which is open at the hub (inlet) and at the tip (outlet). Above it lies a triangular isosceles channel, called impingement channel, with a rounded apex. On this channel lateral walls the film cooling holes are realized, while on the wall, that divides these two channels, called web wall, the jet holes are realized.
The jet holes are three racetrack-shaped holes with hydraulic diameter of $D_h = 34.6\ mm$, while the film cooling holes are circular with diameter d = 15 mm, giving a jet to film cooling hole diameter ratio $d/D_h = 0.42$, which is typical for these geometries. Film cooling holes are 24, divided as follows: six on both suction and pressure sides (figure 9.1) and twelve on the shower head.

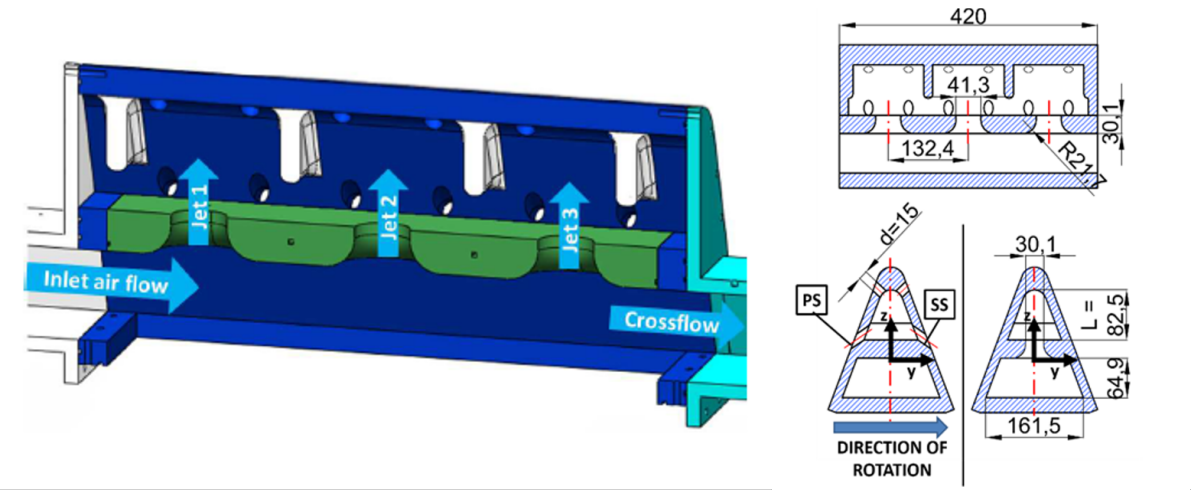


*Figure 9.1: Test section model ad cross section of an advanced leading edge cooling system*

In the triangular channel (figure 9.1) two high blockage ribs are realized, they prevent jets from interacting with each other. This solution is typical for a geometry where the impinging channel does not have a radial discharge for the jets (i.e. all the jets mass flow rate feeds the film cooling holes). In addition to the geometrical peculiarities, the testing parameters are chosen in order to represent engine-like conditions:

- Variable cross flow over the jets, in order to simulate different blade zones
- Different mass flow rate competing to each row of film cooling holes
- Rotating conditions.

The schemes in figure 9.2 depict the multiple air paths and the many mass flow rates splits. As it can be seen, air enters from the feeding channel trapezoidal section at the lower radius, and then it can follow two different paths: it can go either straight out from the tip of the feeding channel or it can, indeed, feed the jets. Once the air has been exhausted through the jet holes, it feeds the three groups of film cooling holes, namely suction side, pressure side and showered. The repartition between the film cooling holes is not equal as previously mentioned and is highlighted more in detail in figure 9.2.

The average cross flow is defined as the ratio between the jets average mass flow rate and the mass flow entering the test section. If the jets mass flow rate is kept constant, the cross flow condition can be modified by changing the ratio between the total inlet mass flow rate and the mass flow rate exhausted at the feeding channel tip. The reason why is so important to test different cross flow conditions is depicted in figure 9.3. The present model with three jets is adequate to represent a limited portion of the whole leading edge cooling system. Thus, by changing the cross flow the test section can be representative of all the blade height portions, as

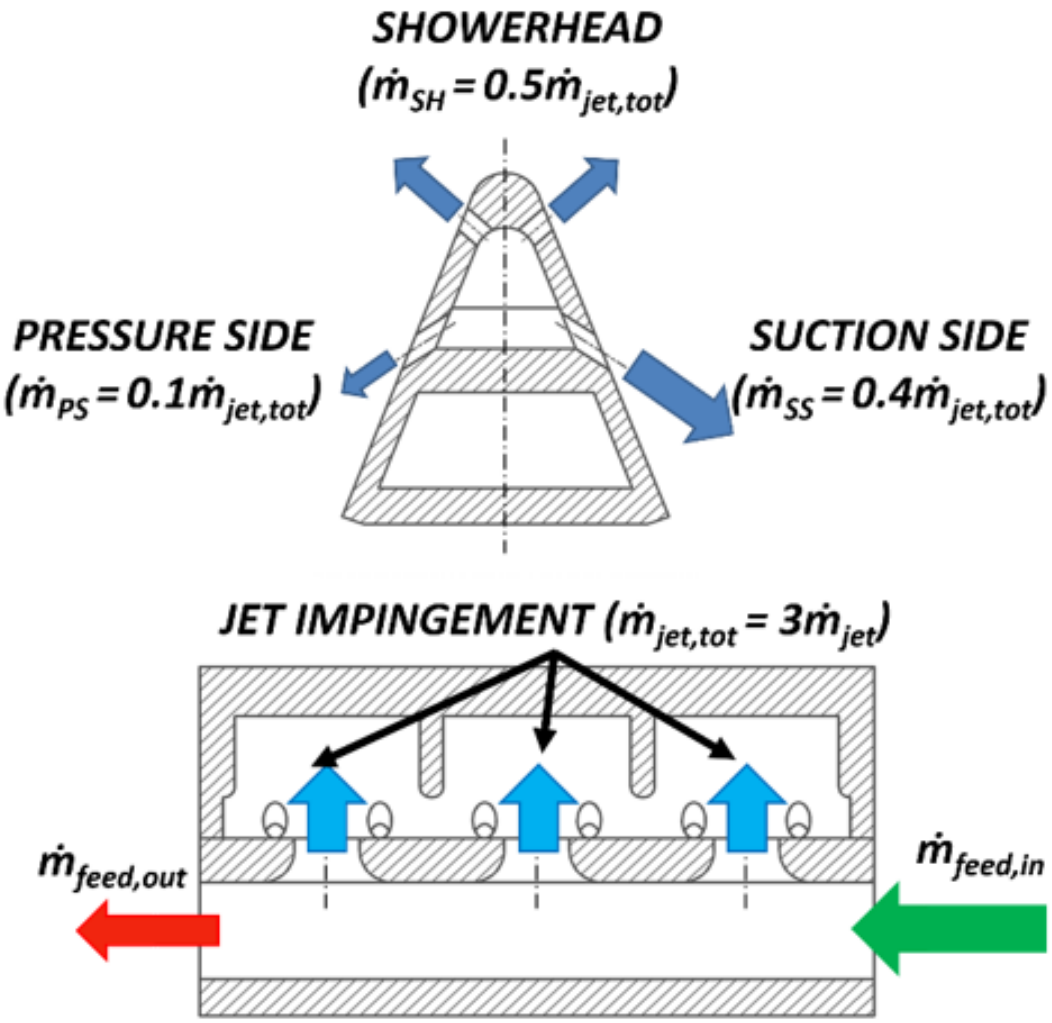


*Figure 9.2: Mass flow rates split among film cooling extraction holes*

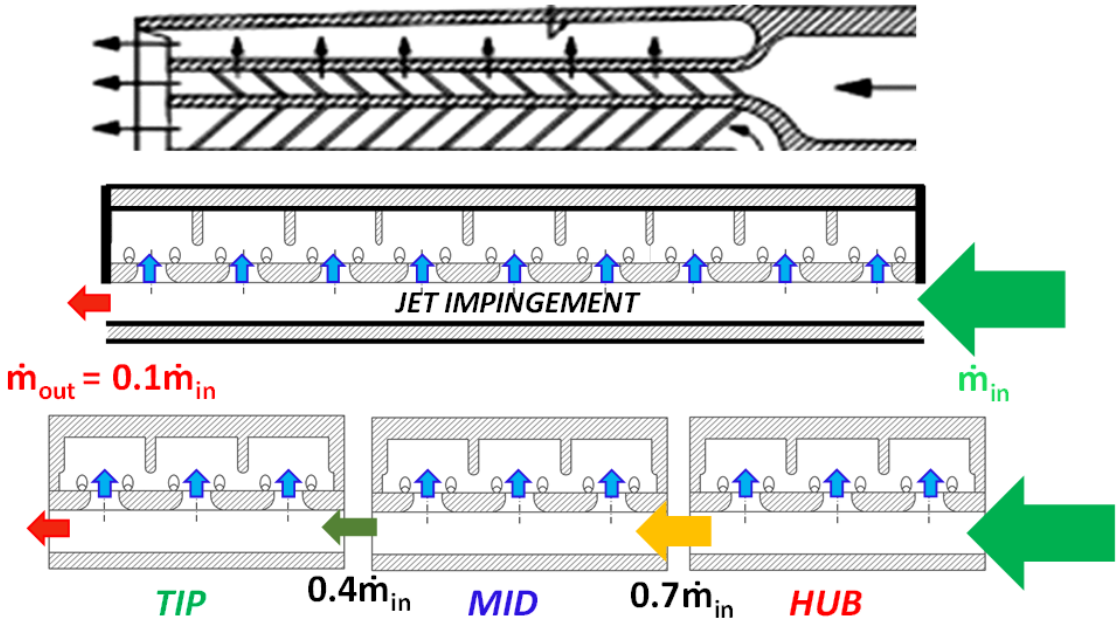


| ZONE | CF =Σṁj/ṁIN |
|---|---|
| HUB | 0.3 |
| MID | 0.42 |
| TIP | 0.75 |

*Figure 9.3: Blade zone definition: modular boundary conditions*

highlighted in figure 9.3.

From this brief analysis, several critical aspects have arisen, in particular regarding the mass flow rate control in the several test section branches. This could not be a problem if the test section would not have to be tested under rotation. In fact, the same test section had already been investigated in static conditions by [18]. The solution adopted in that case was to utilize an open loop air circuit with multiple vacuum pumps. In particular, as depicted in figure 9.4, each line with a different mass flow rate had its own pump and mass flow rate orifice. In that way, the required mass flow rates could be set and controlled independently. Unfortunately, since the test section had to be installed on the rotating rig described in chapter 5, it was not possible to consider the realization of multiple feeding lines.

Another issue that had to be taken into consideration in view of the rotating tests was the uniformity of the mass flow rate discharged by the film cooling holes along the test section radial extension.

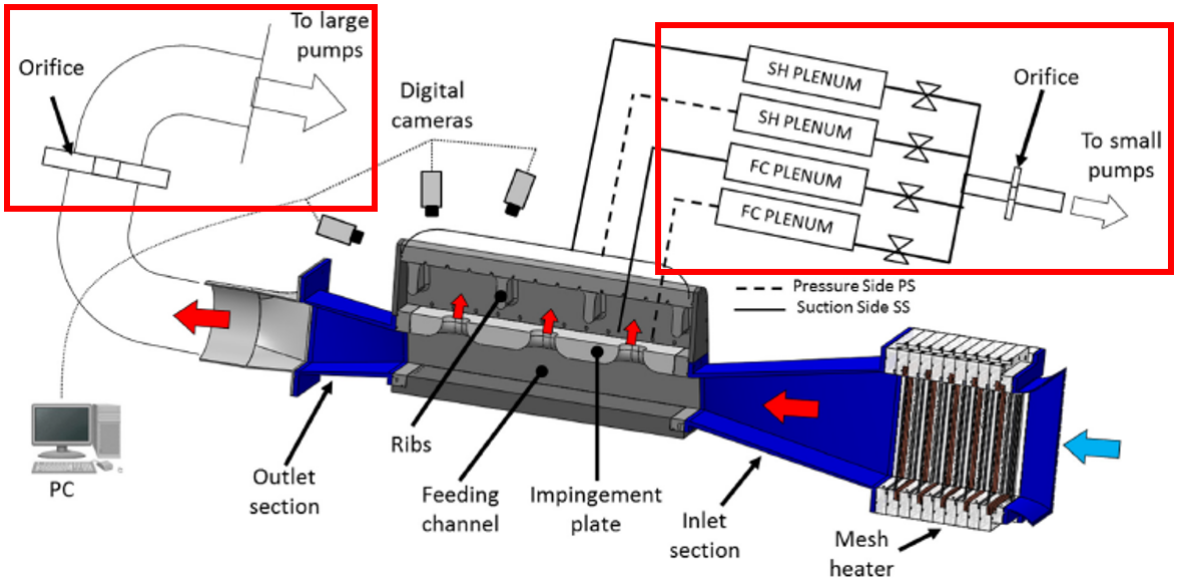


*Figure 9.4: Solution adopted by Andrei et al. [18] to control independently cross-flow and film cooling holes mass flow rates*

The more trivial threat is of course the fact that if the holes are left free to discharge in ambient while the test section is rotating, trailing and leading sides experience opposite conditions. While on the leading side the outlet section of the film cooling hole experiences the dynamic pressure, on the trailing side there could be unknown recirculation that will alter the mass flow rate distribution.

Ascertained that film cooling holes cannot be left free of discharging air directly in ambient, another problem has to be considered. As it can be seen from figure 9.5 (a), due to the centrifugal force, a static pressure gradient arises inside the channel, with pressure increasing toward higher radii. The pressure gradient determines variable inlet condition on every single film cooling hole. In order to overcome this major concern, two different solution have been considered based on a similar idea: the pressure gradient on one side of the hole (i.e. inside the test section) has to be compensated on the other side (i.e. outside the test section), since not much can be done to avoid the one inside the test section.

The straightforward solution is to realize a volume outside the test section where the extraction holes discharge the air. In this way, the same pressure gradient arose in the test section will have arisen in the volume, restoring the same conditions for every hole. The concept is proposed in figure 9.5 (b).

Another solution, schematized in figure 9.5 (c), is to collect the mass flow exhausted by each film cooling hole and discharge it in a plenum in a diametrically opposite position. In this way, the same pressure gradient arose in the test section would be found in the plenum, hence restoring the same conditions for every hole.

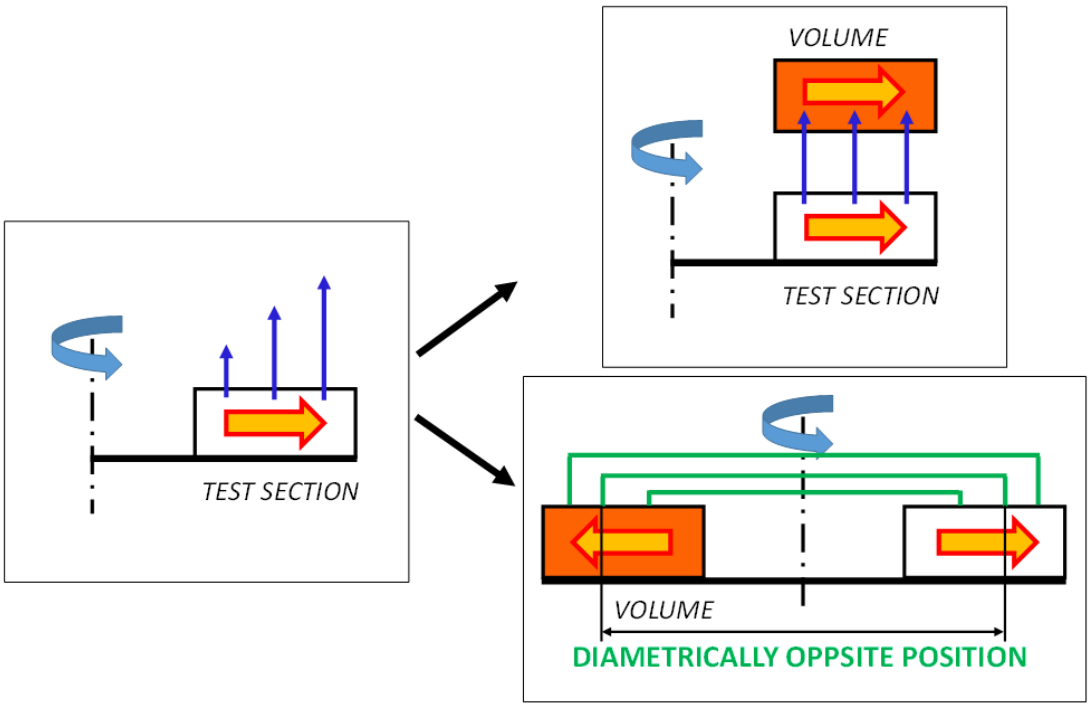


*Figure 9.5: Mass flow rate repartition between the film cooling holes and jets: centrifugal pressure gradient (a) and solutions to overcome it: (b) return channels, and (c) opposite volumes*

The choice between these two solutions is completely arbitrary, given the fact that both of them do not guarantee an engine-like pressure distribution at the outlet of the film cooling holes. In fact, in a real engine, the pressure of the main flow varies along the blade height (i.e. the radial extension), hence it would be extremely complex to set a realistic boundary condition in the test section. Since a choice has to be made, the imposition of the same mass flow rate for every film cooling hole is the safest to verify and most general possible

The final choice fell on the second solution for the easier realization regarding structural reliability. Moreover, this solution allowed to ease the mass flow rate control task. In fact, three plenum have been realized, one for each film cooling line. At the end of each of them, an orifice mass flow meter had been installed in order to directly measure the integral mass flow rate competing to each line, ad by sum to compute the total mass flow rate discharged by the jets. In figure 9.6 is schematized the actual realization of the test article, that allows to describe the overall mass flow rate control and the multiple air paths. As it can be seen, and already commented in chapter 5, air is drawn from the ambient through a pipe that bifurcates and discharge the air inside the bottom settling chamber (figure 9.6, ref-1). The design of the inlet pipes has been made with the purpose of better ensuring a uniform air admission into the test section, for this reason they are also turned in the opposite direction with respect to the channel inlet. Then, air enters the test

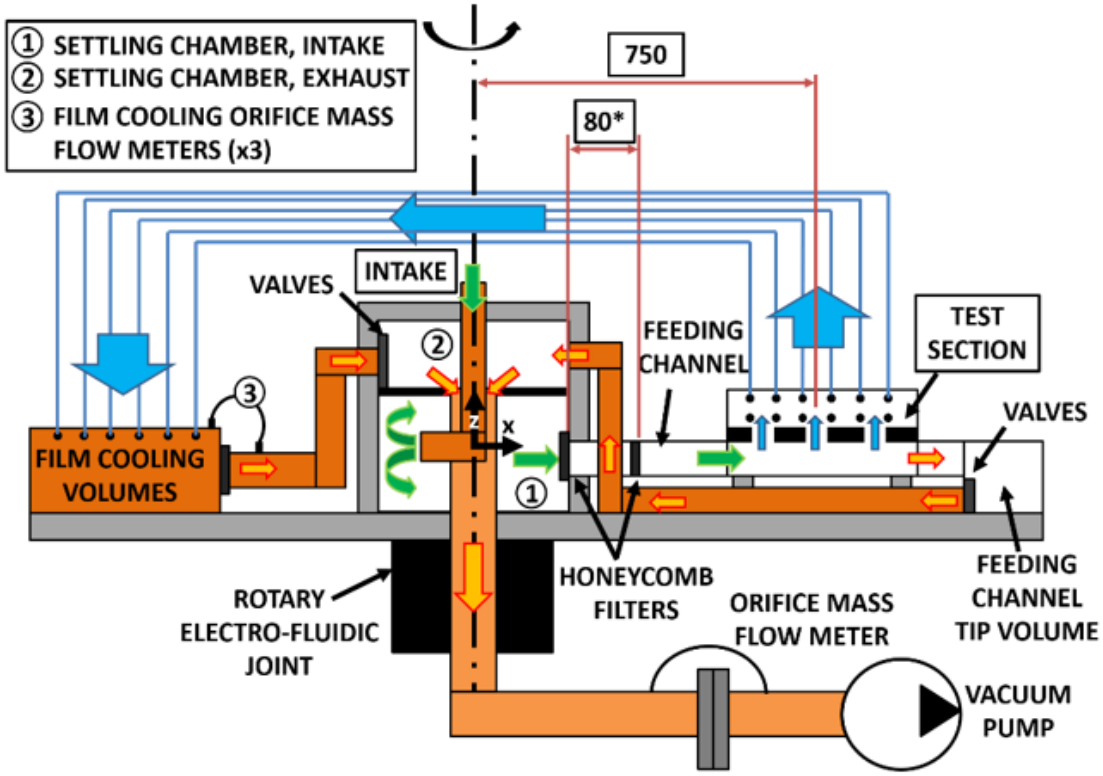


*Figure 9.6: Rotating facility with the test article (a) with emphasis on multiple flow paths and geometrical details of the test section (b)*

section through a honeycomb filter and inlet of 350 mm length. The trapezoidal inlet conduct has the purpose of allowing flow development before the actual test section and the motivation underlying this choice will be depicted in the following paragraphs.

In the test section, air, as already mentioned, is split between two paths. The air that is discharged at the test section tip is collected into a volume and redirected to the top settling chamber (figure 9.6, ref-2) by two pipes. The position of the pipes is such that it determines the less disturbance to the flow field inside the test section allowing a symmetrical discharge. Where the pipes are connected to the tip volume, two guillotine valves are installed (figure 9.7 (c). The valves are manually regulated in order to set the correct mass flow rate split between the jets and the tip discharge.

The air that feeds the jets is then exhausted by the three lines of film cooling holes. As it can be seen from the detailed view of the test section in figure 9.7 (a), each individual hole is connected to a pipe that connects the test section to the volumes in the opposite side of the test article. The lateral view shows how each hole discharges the air at a diametrically opposite position. The three volumes are connected to the upper settling chamber through pipes. In figure 9.7 (d) is

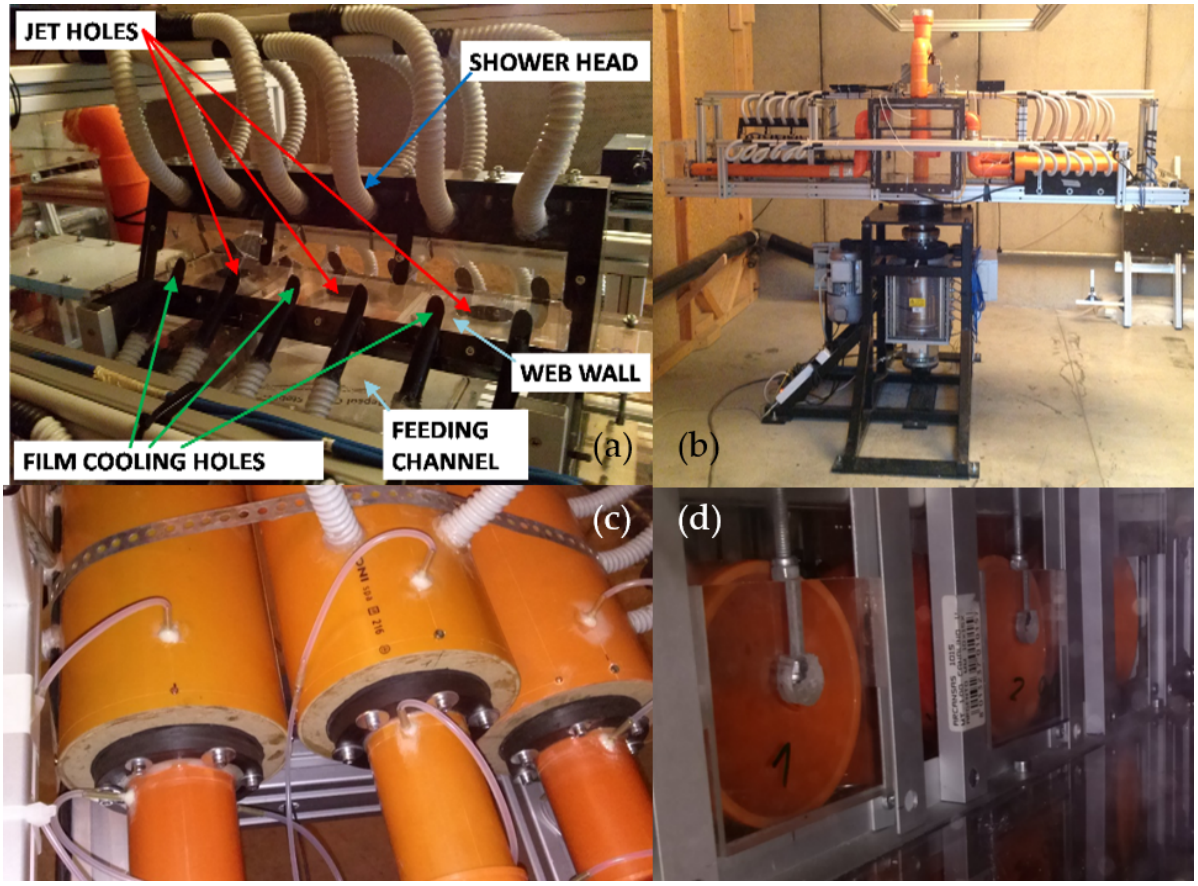


*Figure 9.7: Test section (a), rotating facility (b), guillotine valves (c) and custom orifice mass flow meters*

reported a detailed view of the orifice mass flow meters installed on the volumes. This devices are not conventional due to the different diameter between the volume upstream and the pipe downstream, and the proximity of the pipe turn. For these reasons they have been calibrated in order to correctly measure the mass flow rate of each film cooling line. The sum of these three flow rates provides the total air discharged by the jets.

In the zone where the three pipes are connected to the upper settling chamber three guillotine valves are realized. Their regulation allows to impose a different mass flow rate to each film cooling line.

The air in the upper settling chamber is finally sucked through a pipe connected to the rotating electro-fluidic joint and driven to the ambient air by the vacuum pump. Between the electro-fluidic joint and the vacuum pump an orifice mass flow meter has been installed in order to measure the total mass flow rate that enters the test section. In this way, by subtracting from the total the mass flow rate competing to the jets it is possible to calculate the mass flow rate exhausted through the tip of the test section. All these measurements and computation allow to determine the cross flow condition.

CHAPTER 10

# EXPERIMENTAL INVESTIGATION

## 10.1 Investigated planes and reference conditions

**Table 10.1:** *Measurements planes definitions*

| Plane tag | Type measure | M [px/mm] | Res [vectors/mm] | Ref [mm] |
|---|---|---|---|---|
| xy | 2D | 8.4 | 0.53 | z = 32.9 |
| yz1 | S-PIV | 15 | 0.94 | x = 750 |
| yz2 | S-PIV | 14 | 0.87 | x = 685 |
| xz | 2D | 12.5 | 0.75 | y = 0 |
| yz | 2D | 10 | 0.625 | x = 765 |

Since the campaign is mainly focused on the jets behavior, both Reynold and rotation number have been referred to the jets characteristics. Tests have been performed at two different Reynolds numbers, namely 10000 and 30000, while only one rotational number of 0.05 has been tested. These values are typical for these kind of cooling channels and their common operative conditions. Despite being the reference conditions referred to the jets, the adimensionalization of velocity results depends on the channel zone. In fact, in order to obtain meaningful velocity levels in the plots, the data measured in the jets channel are non-dimensionalized with respect to the jets bulk velocity, while the data in the feeding channel is non-dimensionalized with respect to the feeding channel bulk velocity.
Another important parameter is the crossflow condition, which allows to emulate different zones along the blade radial extension (i.e. blade height), and it is defined as the ratio between the total

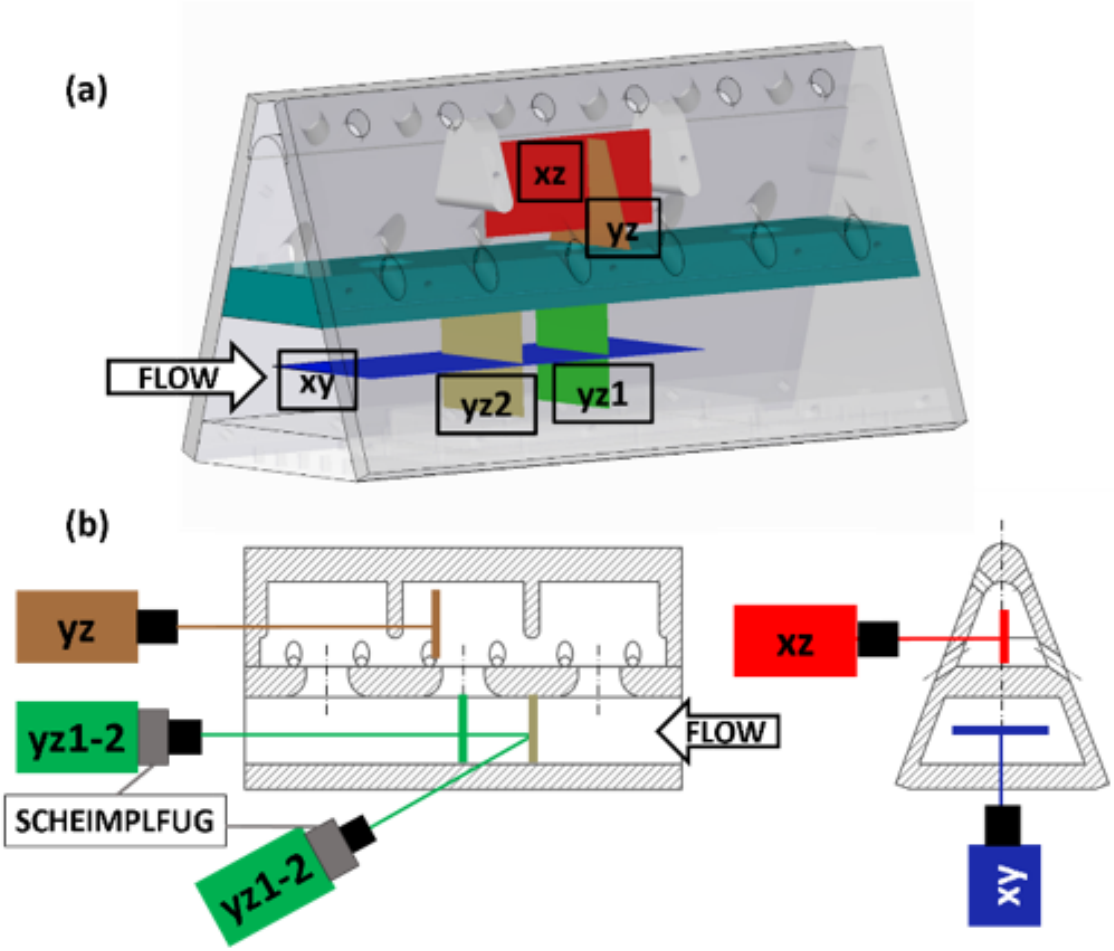


*Figure 10.1: Investigated planes*

mass pertaining to the jets and the total inlet mass flow rate. (i.e. $CF = \Sigma \dot{m}_j / \dot{m}_{IN}$). In particular three main zones have been identified, namely HUB, MID and TIP.

The rotation number defined at the inlet of the test section, used to characterize the feeding channel flow condition, is very important. In fact, since the crossflow conditions has been tested at fixed jets Reynolds number, hence constant jets mass flow rate, the mass flow rate the inlet decreases while changing conditions from HUB to TIP. Considering also that $Ro_j$ remains constant, hence constant rotational speed, the result is a higher rotational number for the TIP condition with respect to the HUB condition. In particular, for the three crossflow conditions, the Ro defined on the inlet of the feeding channel were equal to 0.1, 0.15 and 0.25, for HUB, MID and TIP respectively. The overall test matrix, as well as important information regarding the tests, are reported in table 10.1.

The planes chosen for the PIV measurement are sketched in figure 10.1. As it can be seen two

S-PIV measurements have been performed in two cross sectional planes at different radii, in order to characterize the secondary flow structures induced by rotation between the jets (plane yz1) and in correspondence of the center of the central jet (yz2). Moreover a two-window 2D measurement has been performed on the xy plane at feeding channel mid height to have a complete characterization of the flow field inside the feeding channel.
As far as regards the jets investigation only the central one has been taken into consideration and three planes have been investigated. Plane xz has been used to characterize the cross flow effect, while the analysis has been completed with measurements on plane yz. Additional measurements have been carried out inside the inlet duct in order to characterize the inlet conditions.

**Table 10.2:** *Test matrix*

| $Re_j$ | $Ro_j$ | **Blade zone** |
|---|---|---|
| 10000 | 0 | HUB |
| | | MID |
| | | TIP |
| | 0.05 | HUB |
| | | MID |
| | | TIP |
| 30000 | 0 | HUB |
| | | MID |
| | | TIP |
| | 0.05 | HUB |
| | | MID |
| | | TIP |

## 10.2 Inlet conditions

Since an important part of this work is aimed to the characterization of the different flow field behavior at various blade zones, namely HUB, MID and TIP, it is important to assess the inlet conditions for said configurations. In particular, the inlet trapezoidal duct had been designed to allow proper flow development when the channel was subjected to rotation. In this way, it has been possible to obtain different inlet conditions, according to the rotational numbers at the inlet of the feeding channel for the tested cross flow conditions. If the test section would have been directly fed by the settling chamber, it would have not been possible to allow the Coriolis induced vortices to develop and alter the velocity distribution at the test section inlet, hence a

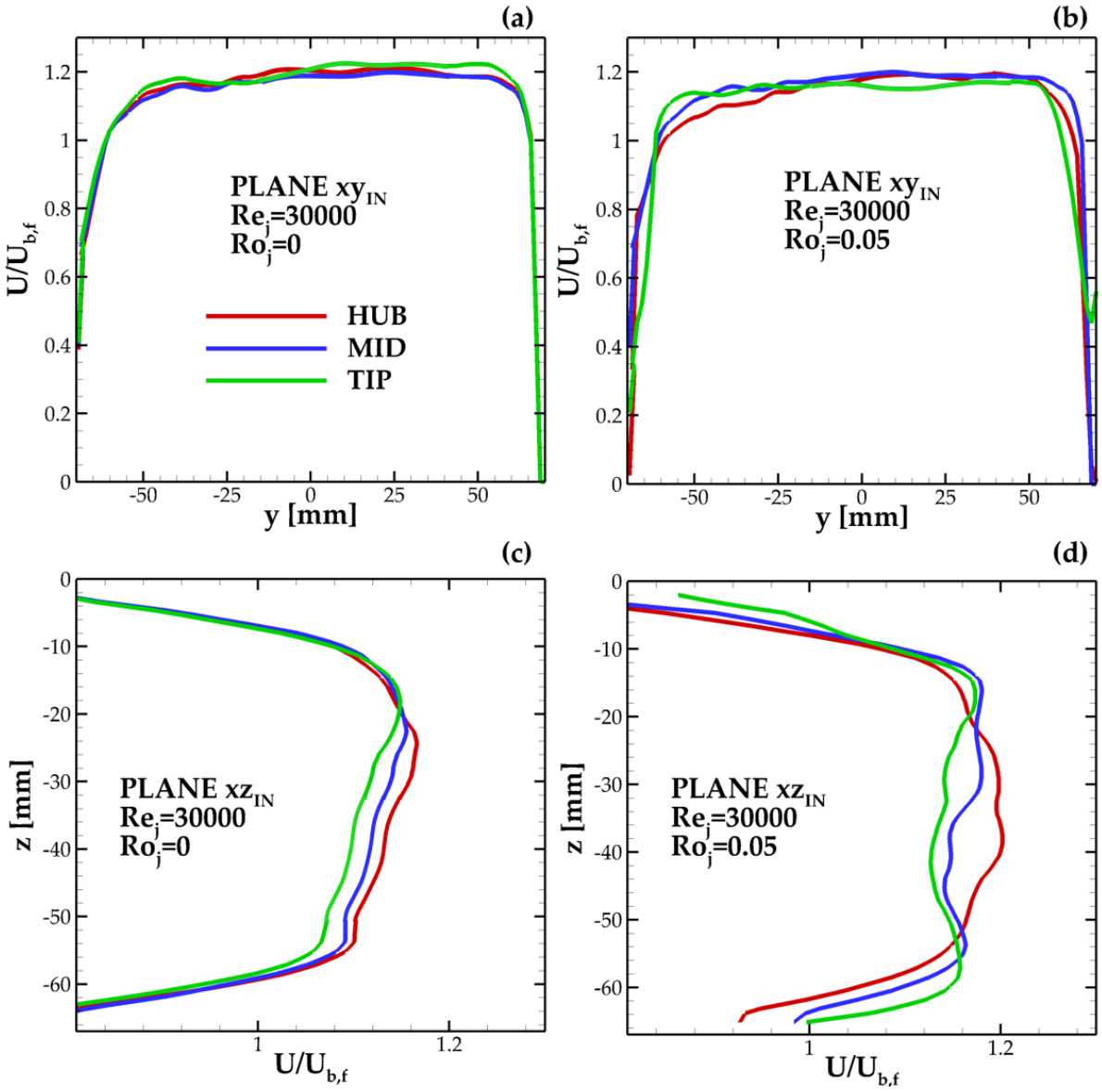


*Figure 10.2: Inlet conditions*

less realistic boundary condition would have been imposed.

In figure 10.2 are reported the velocity profiles extracted at x=440mm and channel mid-height from plane xy and x=440mm and channel mid-width from plane xz in both static and rotating conditions. As it can be seen from figure 10.2 (a), the flow on plane xy is slightly unbalanced towards the leading side, probably due to the not perfect alignment of the honeycomb filter. Moreover, it has to be pointed out that the unbalance is the same for each crossflow condition tested (i.e. HUB, MID and TIP), since the three profiles are basically superimposed. On the perpendicular plane, i.e. xz, figure 10.2 (c) shows a flow unbalance towards the upper wall, which

is plausible since the cross section is trapezoidal with the minor base on the top. As fas as the rotating condition is concerned, on plane xy (figure 10.2 (b)) the flow is evened along the channel width due to the mass transport, caused by the Coriolis' force, towards the trailing side at channel mid-height. On plane xz (figure 10.2 (d)) it can be seen even a more evident effect of rotation. In fact, due to the increase of Ro while moving from HUB to TIP condition, occurs a more evident acceleration of the top and bottom boundary layers, hence a different velocity distribution for the three crossflow conditions tested that was not detected on plane xy. âĂČ

## 10.3 Results

### 10.3.1 Feeding channel

#### 10.3.1.1 Static conditions

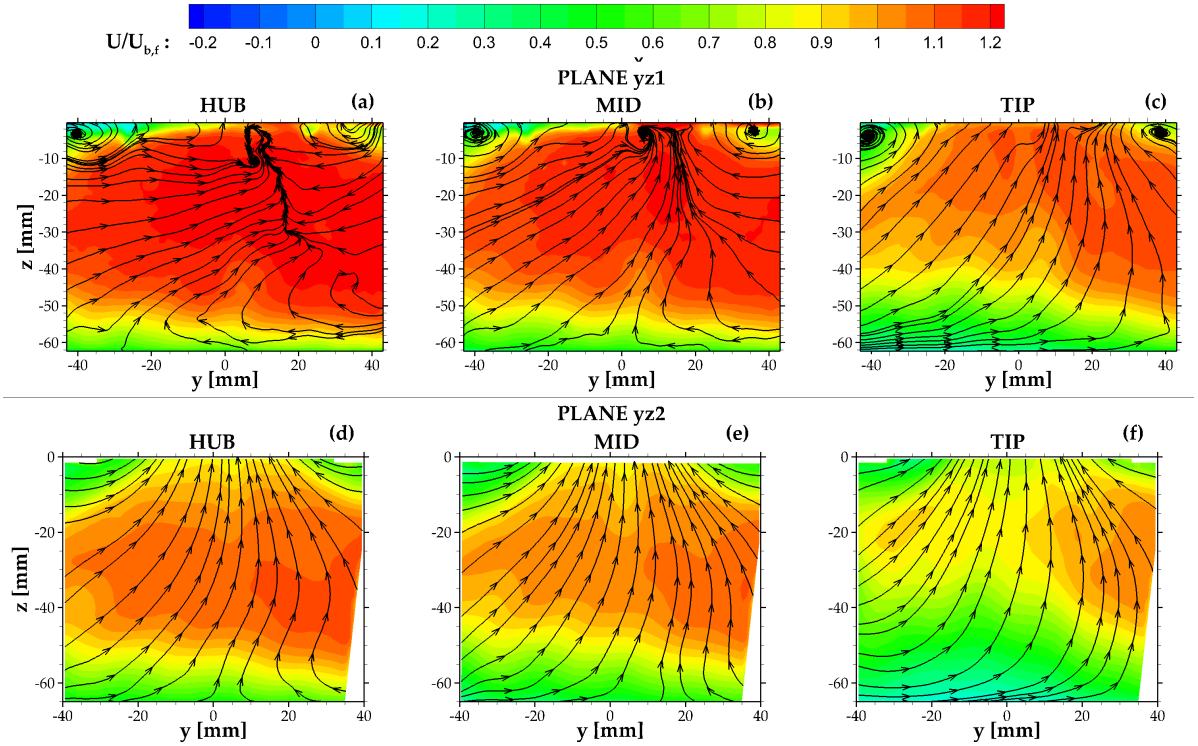


*Figure 10.3: Feeding channel, $Re_j = 30000, Ro_j = 0$ - velocity contours on planes yz1 (a-c) and yz2 (d-f) for HUB (left column), MID (central column) and TIP (right column) cross flow cases*

The result discussion begins with the analysis of velocity maps on cross sections yz1 and yz2. As it can be seen in figure figures 10.3, where the tests at Ro = 0 are reported for all the cross flow conditions, the distribution of velocity components lying on the planes is rather trivial. In fact, it can be seen how the streamtracers are directed towards the upper wall, due to the

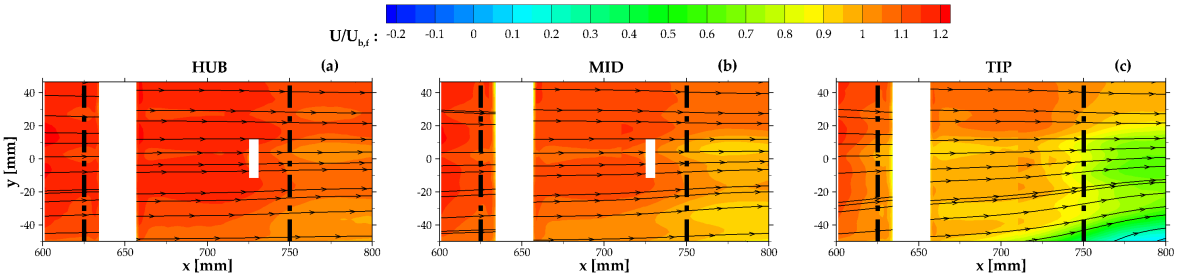


*Figure 10.4: Feeding channel, $Re_j = 30000, Ro_j = 0$ - velocity contours on plane xy at variable cross flow conditions (HUB, MID, TIP respectively in the first, second, and third column*

presence of jet holes, hence flow discharge through the jets. This effect can be seen on both plane yz1 (figures 10.3 (d)-(f)), located at the center of the central jet and plane yz2 (figures 10.3 (a)-(c)) located between the first and second jet. In figures 10.3 (a)-(c) (i.e. yz2 plane) it is also possible to detect the existence of two counter rotating vortex cells, found close to the web wall. The genesis of these structures is not easy to understand with the currently available data but they have all the characteristics to be recognized as the footprints of a horse shoe vortex system that has been generated upstream of the measurement plane and in correspondence of the first jet of the web wall. Indeed, the accelerated stream of flow entering the jet hole, may act a blockage effect on the near web wall flow, so causing its deviation towards the channel lateral walls and the growth of secondary vorticity responsible for the onset of the commented vortex cells. These latter, are then convected downstream by the mean flow.

However, the most interesting feature that rises from the analysis of these contour plots is the distribution of the out of plane velocity U, which can be appreciated by observing the color levels. The color maps depict an unexpected flow unbalance towards the channel suction side (positive y) that is enhanced when moving from HUB to TIP conditions, i.e. when the crossflow ratio is reduced. The comparison between plane yz1 and yz2 at same blade zone suggests that the flow unbalance increases along the channel radial direction.

The velocity data on plane xy (feeding channel mid height), as it can be seen in figures 10.4, shows the same increase of flow unbalance along the channel radial direction (x) that can be seen from the velocity contours on planes yz1 and yz2 (figure 10.3). Moreover, these velocity data allow to identify the source of U unbalance in correspondence of the jets holes centers (black dashed lines are plotted at the position of the first and middle jet-holes), hence showing a strong influence of the jets on the feeding channel flow field. A possible explanation for this flow non symmetry can be found in the different mass flow bleeding that is realized on SS and PS film cooling lines inside the impingement channel. The analysis on plane xy also confirms the fact that the flow unbalance becomes stronger for decreasing crossflow conditions.

#### 10.3.1.2 Rotating conditions

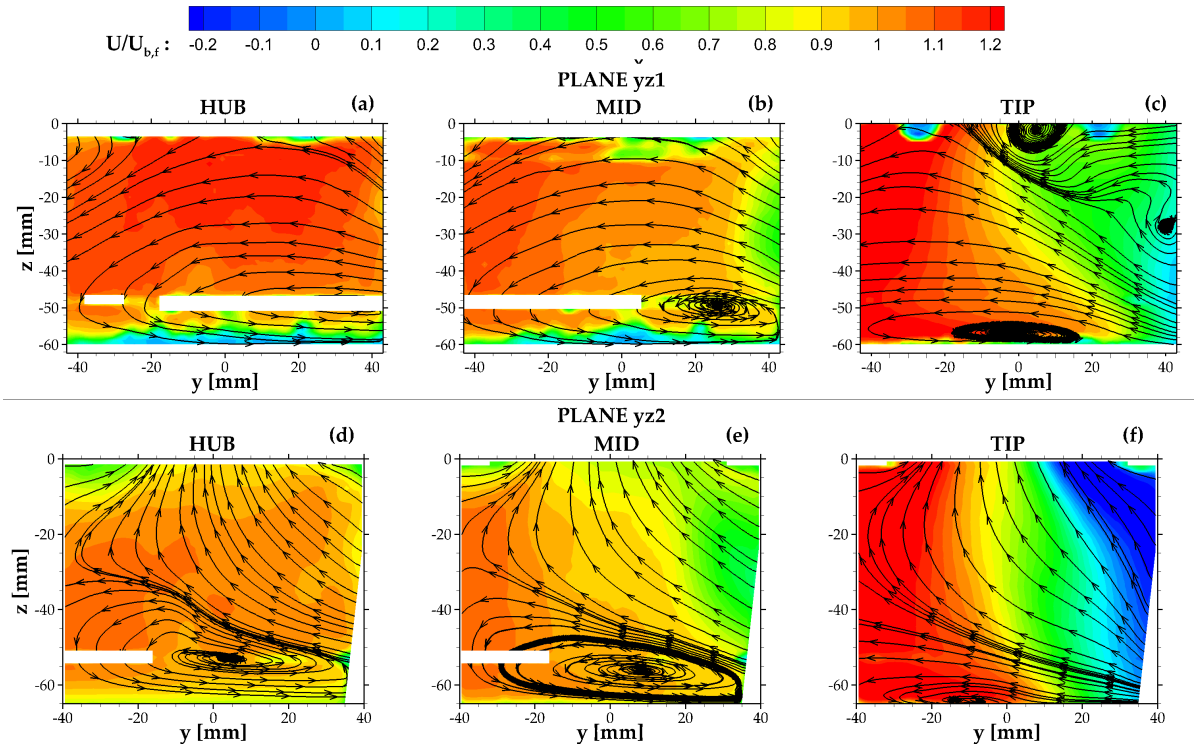


*Figure 10.5: Feeding channel, $Re_j = 30000, Ro_j = 0.05$ - velocity contours on planes yz1 (a-c) and yz2 (d-f) for HUB (left column), MID (central column) and TIP (right column) cross flow cases*

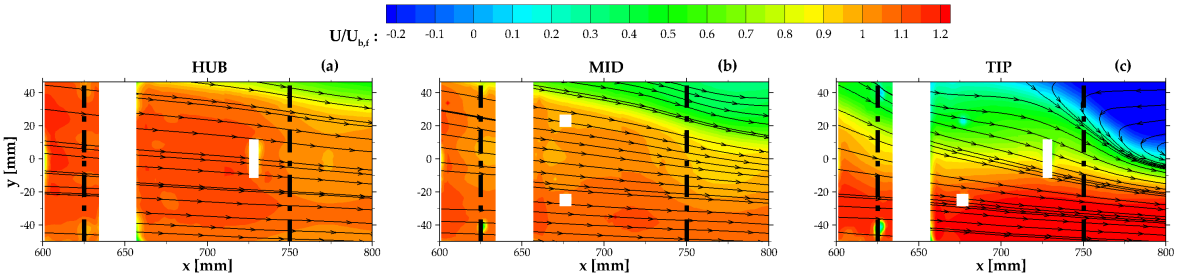


*Figure 10.6: Feeding channel, $Re_j = 30000, Ro_j = 0.05$ - velocity contours on plane xy for static (top row) and rotating conditions (bottom row), and at variable cross flow conditions (HUB, MID, TIP respectively in the first, second, and third column*

When $Ro_j = 0.05$ cases are analysed (figure 10.5 and 10.6), an even more evident flow unbalance is observed, but this time the velocity peak is found on the duct trailing side (y<0, PS). Indeed, rotational effects prevail over every possible source of flow non symmetry found for

$Ro_j = 0$. Again, the cross-wise velocity gradient is much stronger at the TIP where its amplitude is so high to cause velocity reversal at the duct leading side (see the blue/negative areas at y>0 in figures 10.5 (c) and (f) and figures 10.6 (c) for x>750mm). The origin of this behavior is strictly linked to the rotational effects that are commonly expected inside a radial flow duct in orthogonal rotation and that, as previously explained, are made stronger at the TIP since the local Ro is much higher than for the HUB case. Coriolis forces are also responsible for the secondary vortical structures found in the yz planes (both 1 and 2) for $Ro_j = 0.05$ (figures10.5). In particular a wide counter clockwise vortex is always found close to the bottom wall, while the opposite clockwise structure is observed close to the web-wall (z=0) only for the TIP case and in between the jet holes (figures 10.5(d)). With specific reference to this position, it is also found that rotation causes the disappearance of horseshoes vortices produced on the sides of the jet-hole for $Ro_j = 0$ (see z>-20 for figures 10.5 (d-e)). Evidently, the appearing of the secondary vorticity associated to the Coriolis vortical structures determines a different behaviour of the near web wall flow with respect to the static case. Again, the available data does not allow to draw a definitive explanation of this behaviour. However, it has to be pointed out that this local flow features does not affect the jet behaviour (as it will be seen in the next section) which is the main focus of this contribution and the more important aspect for the cooling effectiveness of the device.
In order to better visualize the 3-D flow structures that develop inside the feeding channel, a schematization is proposed in figures 10.7, representing the TIP crossflow condition in both static (a) and rotating (b) conditions.

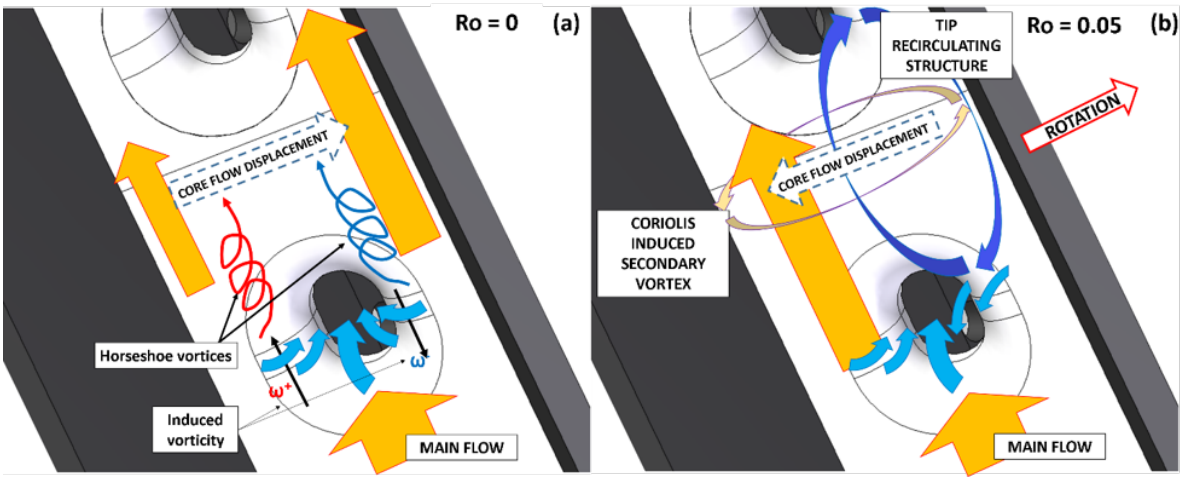


*Figure 10.7: Feeding channel: schematization of the 3-dimensional flow structures development for the cross-flow condition TIP*

### 10.3.2 Impingement channel

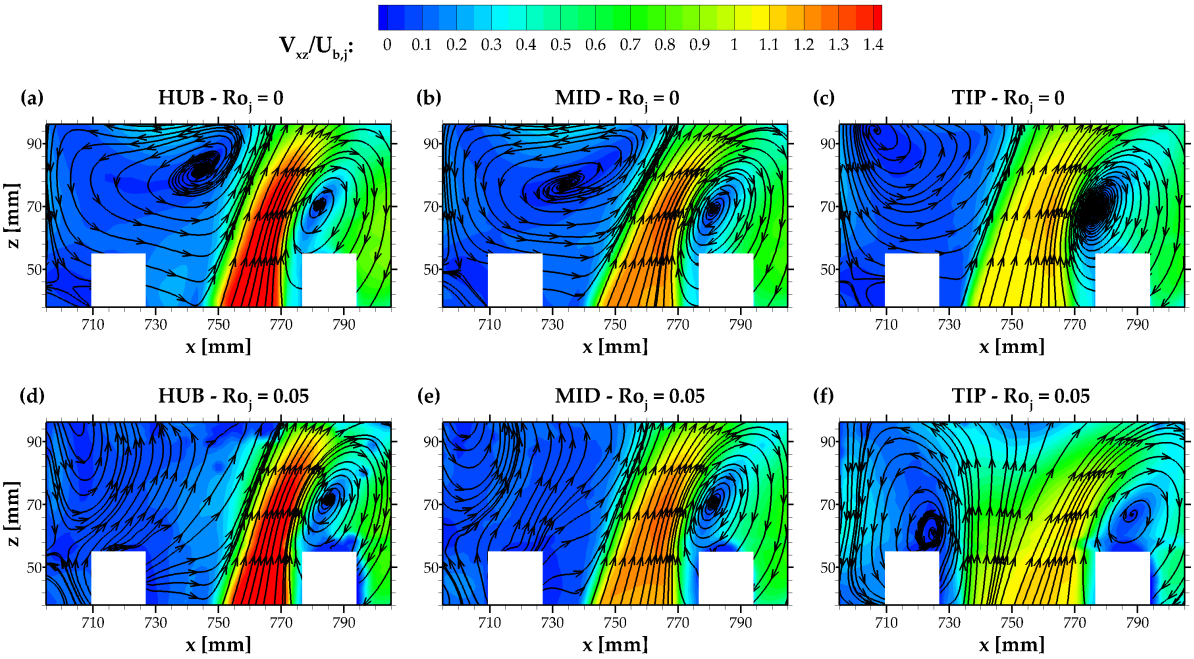


*Figure 10.8: Impingement channel - velocity contours on planes xz, for static (a-c) and rotating (d-f) conditions and for HUB, MID and TIP cross flow cases*

Figure 10.8 and 10.9 reports in plane streamtracers path and contour levels of the W velocity component for the measurements conducted inside the jet core respectively on planes xz and yz. The results at $Ro_j = 0$ for HUB, MID and TIP crossflow conditions are presented in both figures top row. The first main feature of the jet core flow is the remarkable bending towards the tip that can be appreciated by the data in the xz plane (figure 10.8). As the crossflow condition is changed from HUB to TIP, the bending is reduced and the jet core widens, hence lowering its velocity peak. The velocity profiles extracted at z=40.1mm, namely 10mm from the web wall, (solid lines in figure 10.10 (a)) allow a more quantitative analysis that confirms this observation. As it can be seen, as the crossflow increases, the jet peak velocity increment is amplified. The maximum velocity in MID conditions is 10% higher than the velocity for the TIP case. A further increase in the jet velocity peak of about 20% is found if the cross flow is augmented from MID to HUB condition. Consistently with a constant flow rate through the jets imposed for every cross flow condition, the jet core reduced accordingly. These features could result in different heat transfer on the jet target surface (i.e. the blade leading edge) as the cross flow increases, generating smaller spots of higher heat transfer.

The data on the other perpendicular plane, yz in figures 10.9 and figure 10.10 (b), show a rather

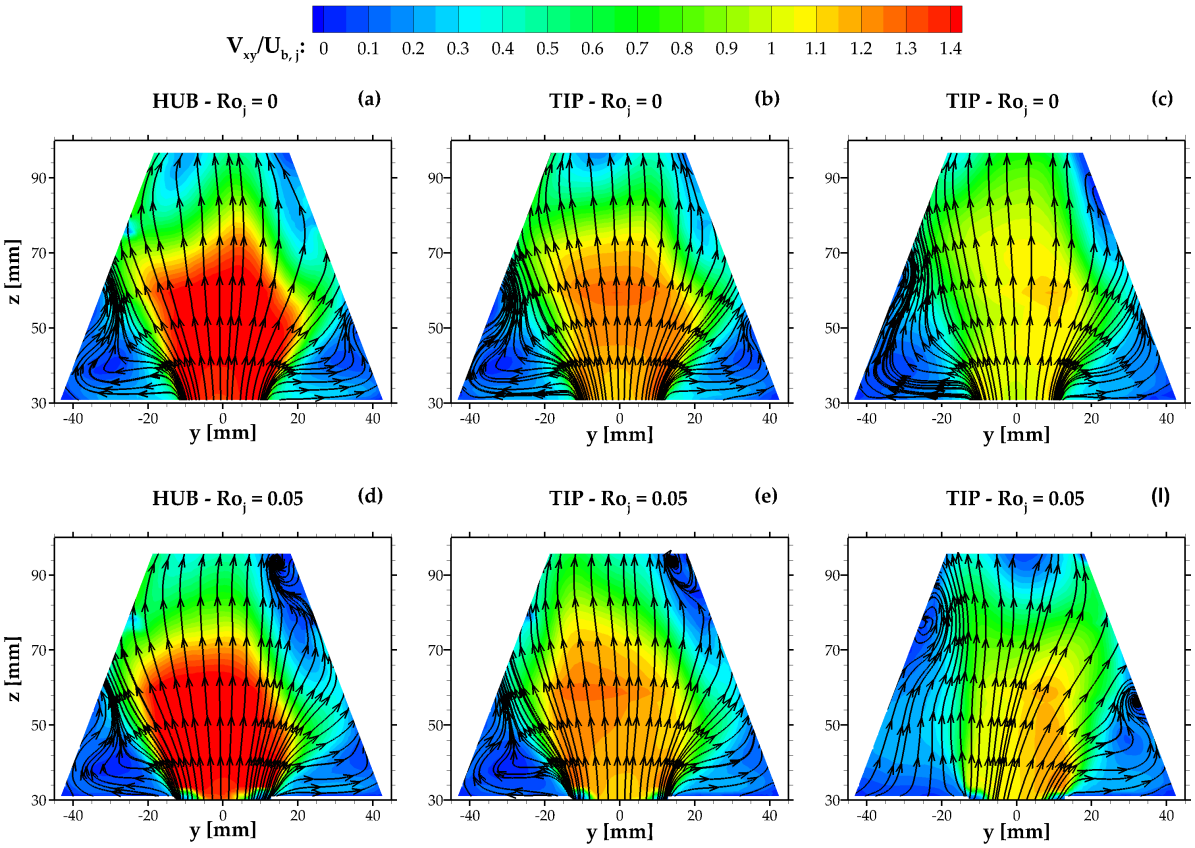


*Figure 10.9: Impingement channel - velocity contours on planes yz and yz, for static (a-c) and rotating (d-f) conditions and for HUB, MID and TIP cross flow cases*

good flow symmetry, with lower velocity peaks found in the jet core for the TIP case in agreement with the previous discussion. If the data at $Ro_j = 0.05$ are considered (figures 10.8 (d-f) and 10.9 (d-f)), only marginal differences can be appreciated with respect to the static case. Indeed both the velocity distribution and the time averaged flow path depicted by the streamtracers are rather similar.

The data for $Ro_j = 0.05$ are presented with dashed lines in figures 10.10 (a) and (b) . All the main features of the jet, i.e. bending toward radial (x) direction that deceases from HUB to TIP and symmetrical distribution along peripheral (y) direction, are almost identical to what is observed for $Ro_j = 0$. Therefore, it can be concluded that no significant rotation effects are able to alter the jet core velocity distribution. From a physical point of view, the main reason of this observation is that the jet is mainly aligned with the rotation axis, hence only a minor velocity component contributes to the generation of the Coriolis acceleration ($\mathbf{a_c} = -2\Omega \times \mathbf{C}$). Moreover, as well as discussed in the open literature [37], even if small Coriolis effects are produced, their main effect

is found in the low velocity areas, such as boundary layer flows or recirculating flow regions. Therefore, in the present case, if rotational effects occur, they might be found far from the jet core, i.e. inside the flow volume that has not yet been investigated.

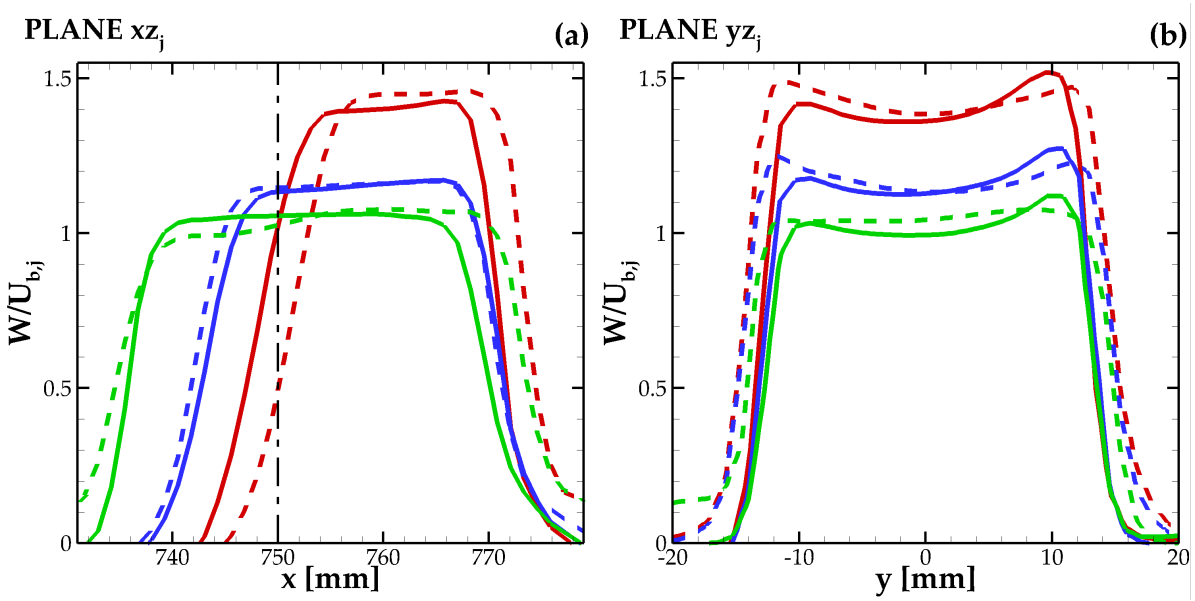


*Figure 10.10: Jet velocity profiles extracted from plane xz at z = 40.1 mm (a) and yz at z = 34.1 (b)*

### 10.3.3 Reynolds number dependence

Reynolds number dependence has been investigated repeating every measurement for the MID zone with $Re_j$=10k (i.e. on every plane and both for static and rotating conditions).
In this particular geometry, the most important feature to be characterized is the jet, indeed the thermal performances mainly depend on its aerodynamics. In order to quantitatively evaluate the jet's Reynolds number dependence, in figure 10.11 the comparison between the velocity profiles from tests at Re = 30k and Re = 10k are shown. The reported data clearly show the Reynolds number variation has almost no effect on the jet flow structure, both in static and rotating conditions, at least in the investigated range.

In order to extend these conclusions (i.e. jet Re-independency in both static and rotating conditions) to the overall channel aerodynamics, the flow field in the feeding channel can be analysed with this perspective. Velocity components profiles extracted from plane yz1 are shown in figure 10.12. For both static and rotating conditions, the three velocity components (i.e. V, W in plane while U out of plane) perfectly match, showing that also in the feeding channel the flow field is Reynolds independent.

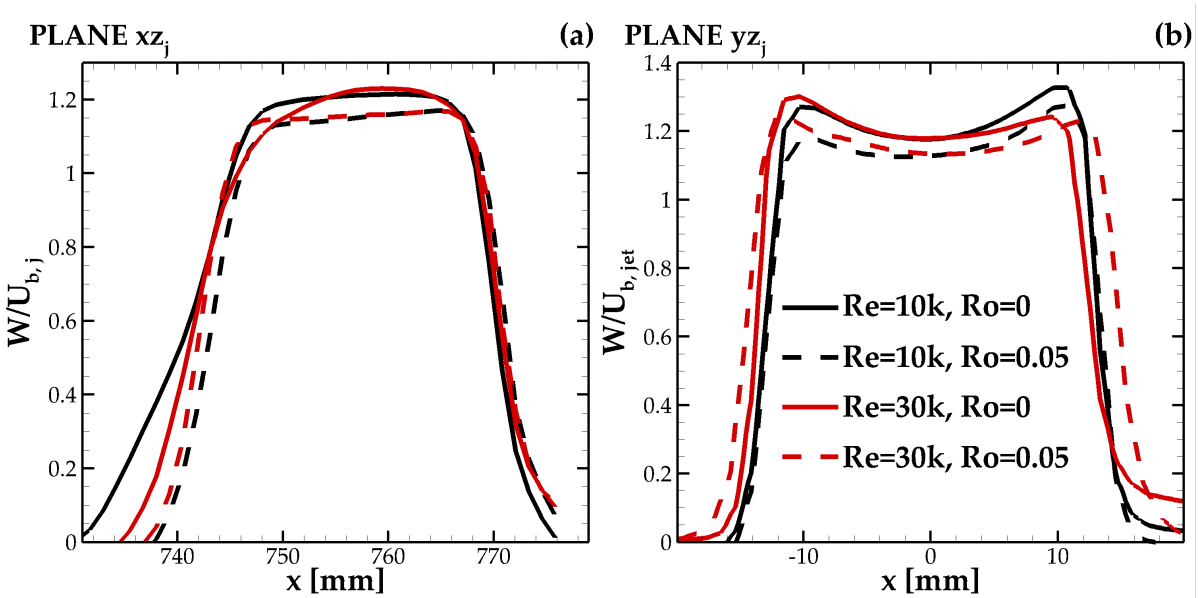


*Figure 10.11: Jet velocity profiles extracted from plane xz at z = 40.1 mm (a) and yz at z = 34.1 (b) for Reynolds numbers of 30000 and 10000*

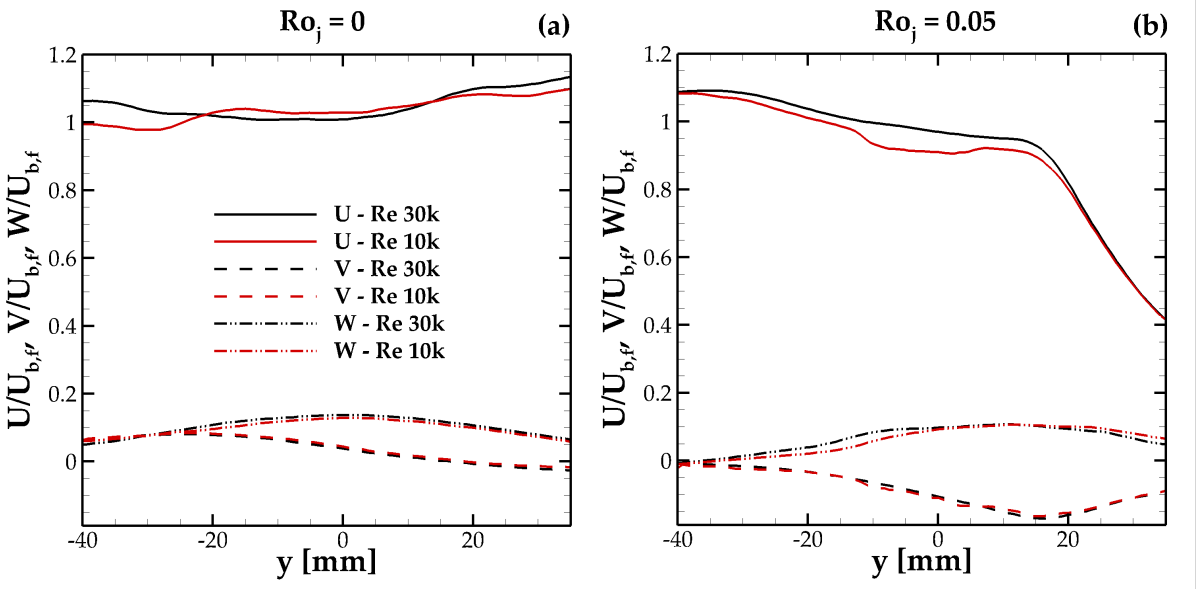


*Figure 10.12: Feeding channel velocity profiles extracted from plane yz1 at z =-32.9 mm for Reynolds numbers of 30000 and 10000: (a) static, (b) rotating condition*

# CONCLUSIONS

The aim of the research performed during this Ph.D. program was to characterize the flow field inside leading edge cooling systems, particularly under rotating conditions. Two separate campaigns had been conducted, one involving the study of a triangular equilateral channel and the other on an advanced leading edge cooling system. The first one allowed to have a better insight on the Coriolis' and buoyancy effects. The results obtained for the second one, allowed to characterize the flow field inside a complex geometry.
In order to be able to perform these experimental campaigns, the rotating facility as well as the processing procedures already consolidated in the research group, had to be improved, thus increasing the expertise of the research group on PIV on rotating channels. Indeed, the development of a new image de-rotating procedure, complementary to the one developed by [32], allows to extend the investigation on planes with arbitrary orientations with respect the rotating axis. Moreover, the additional development of a post processing procedure for parallax correction helped to obtain a higher accuracy for the 2D-PIV measurements on randomly oriented planes. This was possible thanks to the definition of a robust calibration methodology.
One of the most important achievements of this Ph.D. program had also been the upgrade of the rotating facility, which widened the reachable tests condition ranges. This is a crucial aspect in order to perform experiments in engine representative conditions, thus providing both significative results, and a useful database for numerical tools validation.

The investigation on the rib roughened triangular channel concluded a wider research project started with the characterization of the smooth channel. All the information showed the complexity of Coriolis' effects on the flow field even in a simple geometry. Thus, the impossibility to rely on simple flow models to explain the thermal data.
In the ribbed channel, a very three dimensional flow field was detected, in particular involving the recirculating structures between the turbulence promoters. As far as the secondary flow structures detected on the channel cross section are concerned, the presence of the ribs determines an almost Ro-independence. The buoyancy effect was associated with an increment of the flow turbulence, both on TS and LS with respect the static case. This behavior was detected both in the cross section and between the turbulence promoters. On the other hand, the flow field between the ribs was more difficult to characterize. On the trailing side, the length of the recirculating

structure decreased with the increase of Ro, and for equal Ro, in non-isothermal cases. On the leading side the difference in behavior between isothermal and non isothermal cases depended on the rotational number considered. In fact, at the lower Ro investigated, the case at Bo=0.08 showed an increase in the recirculating structure length, and vice versa for the case at Ro=0.6, where at Bo=0.7 the recirculating bubble detected was shorter. The difficulty in analyzing these results is due to the fact that the near wall flow between the ribs, under rotating conditions, is extremely thee-dimensional, and, as showed with the numerical results, the recirculating structure does not have a constant shape along the wall height. This fact, does not allow to identify a noteworthy plane to characterize the inter-rib flow, unlike in the rectangular channel, where it is possible to find a plane of symmetry for both the cross-section and the flow field.
Concerning the comparison with the squared channel, it has to be underlined that despite the substantial differences highlighted about the flow field between the turbulence promoters, in both geometries the buoyancy main effect is to enhance flow turbulence. In fact, the former is the consequence of the interaction between cross-section geometry and Coriolis' induced pressure gradient, while the latter is not influenced by the cross-section shape.

The experimental measurements performed on the advanced leading edge cooling system allowed to characterize the flow field in both the feeding channel and downstream the web wall in both static and rotating conditions, for three different CF conditions. The static measurements revealed a flow unbalance towards the leading side, while the measures performed under rotating conditions showed an opposite behavior, consistently with the literature. In the TIP case, the flow unbalance under rotating conditions was so intense that a broad recirculating structure involved most part of the feeding channel, affecting the jets alimentation.
As far as the jets are concerned, the CF conditions strongly affected the jet core topology, determining jet lower velocities while moving from HUB to TIP conditions. This is not necessarily a negative effect, in fact, since the jet mass flow rate was kept constant for every CF condition, a lower velocity meant a wider jet core flow, thus a larger target surface, hence promotion of cooling uniformity. However, the velocity cannot decrease too much, in order to guarantee sufficient jet penetration towards the target surface. Measurements also confirmed that rotation does not have any effect on the jet core flow, as well as substantial Reynolds independence of the overall flow field.
Finally, the presence of the film cooling holes did not appear to have a significant effect on the jet core flow topology and symmetry.

APPENDIX A

# UNCERTAINTY ANALYSIS

In the following, the uncertainties related to 2D-PIV and S-PIV measurements are provided. Firstly, the 2D-PIV under static conditions is analyzed and an estimation of the maximum uncertainty is discussed. On the basis of the uncertainty for the 2D-PIV, a validation of the S-PIV is provided. Finally, a proof of the reliability of the complex two-step procedure with parallax correction for measurements under rotating conditions is discussed.
The results presented in part 1.6 and IV, refer only to statistical quantities, such as the time averaged velocity flow fields. Due to the limited number of samples (1000) used to compute the flow statistics, the sampling error tends to be larger than other error sources and therefore it was chosen as the overall upper bound estimate for the PIV data uncertainty.

## A.1 2D-PIV Static measurements

For the 2D measurement acquired under static conditions, the normalised r.m.s. errors in the statistical quantities are computed as in [38]:

$$\epsilon_u = \frac{\sigma[U]}{U} = \frac{1}{\sqrt{N}} \frac{u'}{U} \tag{A.1}$$

$$\epsilon_{u'} = \frac{\sigma[u']}{u'} = \frac{1}{\sqrt{2N}} \tag{A.2}$$

where $\sigma$ is the standard deviation, U is the mean velocity, $u'$ is the r.m.s. velocity fluctuation and N is the number of independent samples. The uncertainties in the measured values of U

and $u'$ are simply obtained by multiplying the errors in equations A.1 and A.2 by a confidence coefficient, $Z_c$. Assuming values $Z_c$ = 1.96 (corresponding to a 95% confidence level) and N = 1000, the overall upper bound estimate of the uncertainty in the mean velocities turns out to be less than 2%. This value applies to the largest part of the velocity fields, with the exception of those limited regions affected by very low velocities and high fluctuations, namely inside zones of separated flow. Under the same assumptions, the maximum uncertainty in the estimate of the r.m.s.velocities is less than 5%.

## A.2 Streoscopic PIV

As previously described in section 3.3, perspective view its both S-PIV point of strength and weakness. The former is because it allows to exploit parallax in order to obtain 3D information on a 2D plane, while the latter is determined by the impossibility to ensure that during the calibration procedure described in section 3.3.2 the target lies exactly on the focus plane, determining the so-called misalignment error.
In the present campaign the disparity correction was used as an attempt to minimise the misalignment error, as suggested by Willert [19]. The disparity map was obtained from the ensemble correlation of 100 images from the two views.
As far as measurements performed under rotating conditions are concerned, the relative velocity field has been retrieved by means of the two-step procedure described in chapter 4.1 (obviously without the parallax correction). Since accurate 2D-PIV measurements are available in both static and rotating conditions, the accuracy of the S-PIV ones can be assessed with a cross comparison of velocity profiles extracted along a common line. In figures A.1 (a) and (b) are reported the adimensionalized U and V velocity profiles extracted from planes xy and yz1 for the HUB condition. As it can be seen, in both static and rotating conditions, the differences between the profiles are less than 5% of $U_b$. The uncertainty on r.m.s. velocities can be estimated to be between 5 and 10%.

## A.3 Rotating measurements

In chapter 4.1 the main sources of error concerning the phased-lock measurements have been discussed, and can be resumed in the following list:

- image position stability;
- peripheral to relative velocity component magnitude ratio;
- peripheral component computation.

About the first one, the adoption of a variable time delay (see figure 4.3) allowed to compensate for the variations of rotational speed among the acquisition of the image samples. Image shifts

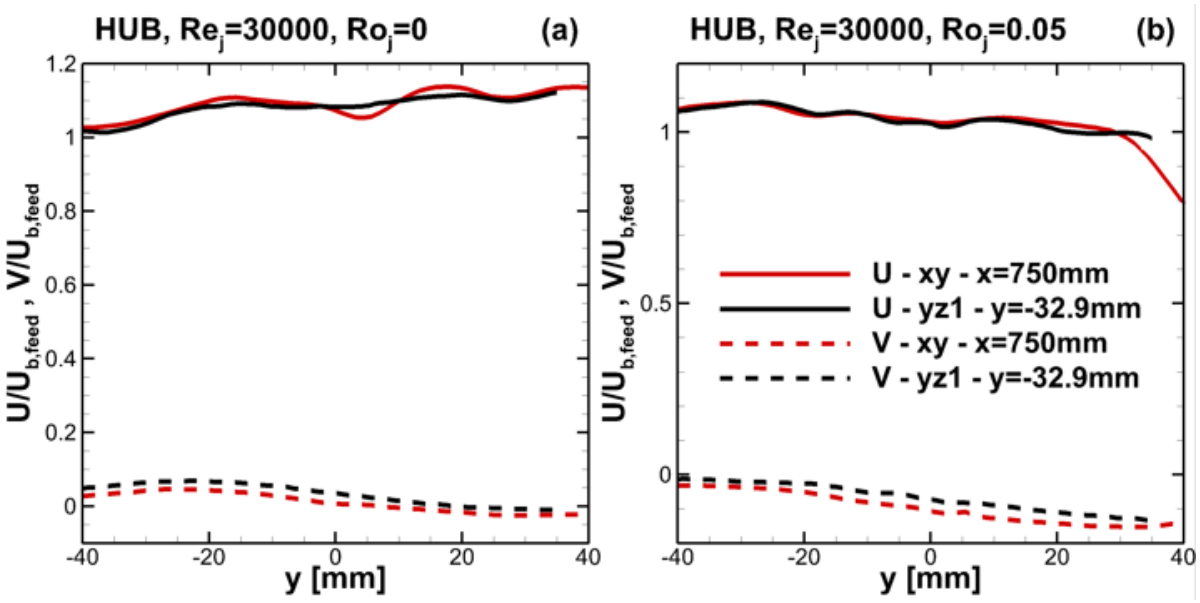


*Figure A.1: Comparison of velocity data at the intersection of planes xy (2D-PIV) and yz1 (S-PIV) under static (a) and rotating conditions (b) (Data from part IV)*

reached maximum values of $\pm 2\ px$, allowing each interrogation window to pertain to the same measurement area, hence guaranteeing that only vectors belonging to the same fluid portion were averaged together.

The second issue was avoided employing the two step processing procedure, therefore allowing to set the PIV parameters as in a static measurement, obtaining displacements in the interval of 6-10px.

Finally, the calibration described in chapter 4.1 allowed to determine the rotation center with an accuracy of $\pm 0.1\ mm$, while the photodiode signal sampling with a 20 MHz counter reduced the error on the rotational speed to $\delta\omega/\omega = 1 \times 10^{-3}\%$. All these factors combined has to be accounted for an increase in the overall upper bound estimate of the uncertainty in the mean velocities up to 5% with respect to $U_b$.

Finally, it has to be observed that for the measurement along the yz (for both experimental campaigns in parts 6 and IV) and $xy'$ (from part 6) planes,the channel rotation determines a misalignment between the laser sheet (image plane) and the actual geometrical plane of the channel. This inconvenience could lead to a significant spatial averaging error. In the case of planes yz, the very small separation time required to avoid tracer particles loss, limits the image/geometrical planes misalignment within the laser sheet thickness. Concerning plane $xy'$, however, the PIV separation time was substantially higher (of the order of $100\mu s$), hence the test section displacement was up to 0.5 mm for the tests at Ro=0.6 in the measurement region (i.e.

average r = 0.709 m). In order to compensate this misalignment, the laser lamp $n.°2$ had been translated from the standard position accordingly to the rotation verse of the test section.
An overall proof of the reliability of the experimental and processing procedure is reported in figure A.1, which reports velocity data from part 6 under the higher rotational speed tested (i.e. Ro=0.6). The comparison between velocity profiles extracted on planes yz and xy', allows to evaluate the overall uncertainty determined by many factors. In fact, it has to be take into account that beside the processing procedures (two-step relative velocity field computation, parallax correction, stereo reconstruction), the difference displayed in figure A.1, is also determined by the misalignment of the measurements planes with the actual geometrical plane. Nevertheless, it can be seen that the difference between the velocity profiles is less than 5 % of the bulk velocity, which is an excellent result.

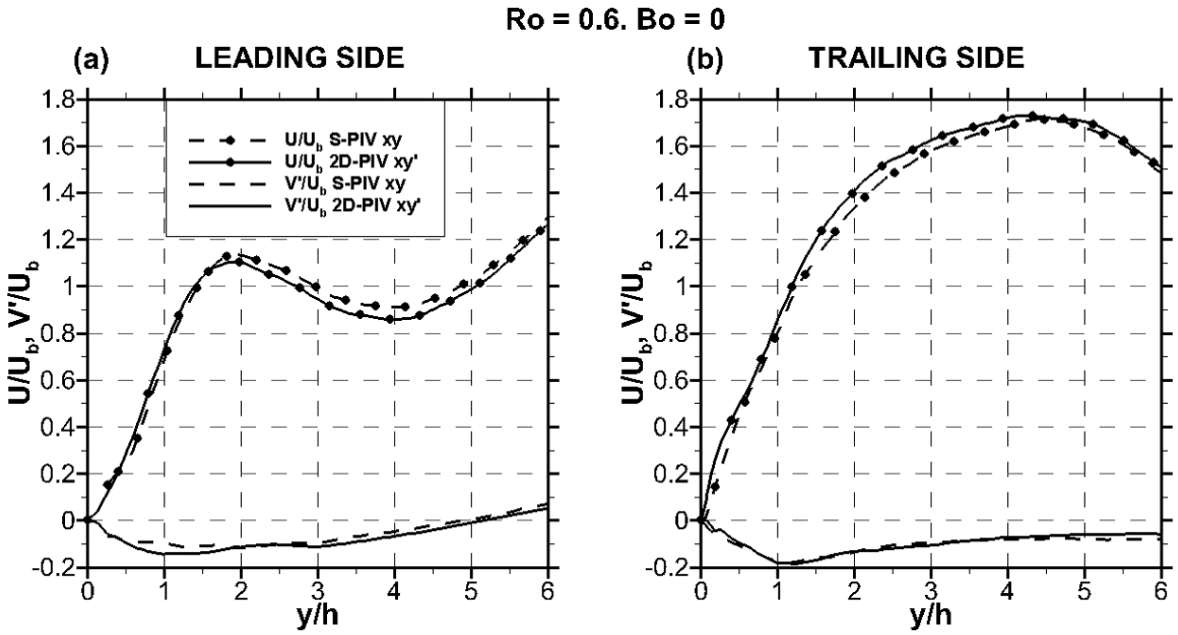


*Figure A.2: Comparison of 2D and Stereo-PIV data extracted on the intersection line of xy' and yz planes of U and V' profiles from 2D-PIV data on xy' and Stereo-PIV data on yz (Data from part 6)*

APPENDIX B

# LIST OF PUBLICATIONS

Conference proceedings:

1 Furlani L., Armellini A., Casarsa L., Buoyancy effects at high rotation number on the flow field inside a triangular shaped rib roughened channel, 11th European Conference, ETC11, March 23-27 2015, Madrid, Spain,url

2 Furlani L., Armellini A., Casarsa L., Aerodynamic behavior under rotation of an advanced leading edge impingement cooling channel, 12th International Symposium on Experimental Computational Aerothermodynamics of Internal Flows , ISAIF12th, 13-16 July 2015, Lerici, Italy

3 Facchini B., Burberi E., Carcasci C., Cocchi L., Massini D., Furlani L., Armellini A., Casarsa L., Effect of rotation on a gas turbine blade internal cooling system: experimental investigation, Proceedings of ASME Turbo Expo 2016: Turbine Technical Conference and Exposition, GT2016, June 13-17 2016, Seul, South Corea, GT2016-57594

Journal publications:

4 Furlani L., Armellini A., Casarsa L., Rotational effects on the flow field inside a leading edge impingement cooling passage, Experimental Thermal and Fluid Science, Vol. 76, 2016, pp 57-66, ISSN 0894-1777, url.

5 Furlani L., Armellini A., Casarsa L., Effects of Rotation and Buoyancy Forces on the Flow Field Behavior Inside a Triangular Rib Roughened Channel, Journal of Turbomachinery

Under review:

6 Furlani L., Armellini A., Casarsa L., Ravelli S., Barigozzi G., Flow field inside a leading edge cooling channel with turbulence promoters in rotating conditions

# List of Symbols

| | |
|---|---|
| $Tu_{xy'}$ | Turbulence intensity computed on plane xy'. |
| $r_p$ | Brayton-Joule cycle pressure ratio. |
| **Bo** | $\frac{(T-T_\infty)}{T} Ro^2 \frac{R}{d}$ - Buoyancy number. |
| **M** | $[\frac{px}{mm}]$ - magnification factor. |
| **Re** | $\frac{U_b D_h \rho}{\mu}$ - Reynolds number. |
| **Ro** | $\frac{\Omega D_h}{U_b}$ - Rotation number. |
| **Tu** | Turbulence intensity. |
| **U** | radial velocity component. |
| **u** | fluctuation of the radial velocity component. |
| **uv** | uv fluctuation. |
| **V** | tangential velocity component. |
| **v** | fluctuation of the tangential velocity component. |
| **V'** | wall normal velocity component. |
| **W** | vertical velocity component. |
| **x** | radial axis. |
| **y** | tangential axis. |
| **y'** | wall normal direction. |
| **z** | vertical axis. |

# List of Abbreviations

**2D-PIV** Two velocity components Particle Image Velocimetry.

**CCD** Charge-Couple Device.

**i.w.** Interrogation window.

**LDV** Laser Doppler Velocimetry.

**LS** Leading Side.

**PIV** Particle Image Velocimetry.

**PS** Pressure Side.

**S-PIV** Stereoscopic Particle Image Velocimetry.

**SS** Suction Side.

**TS** Trailing Side.

# BIBLIOGRAPHY


[1] Y.-H. Liu, M. Huh, J.-C. Han, and H.-K. Moon.
High rotation number effect on heat transfer in a triangular channel with 45 deg, inverted 45 deg, and 90 deg ribs.
*Journal of Heat Transfer*, 132(7):1–10, 2010.

[2] David M. Driver, H.Lee Seegmiller, and Joe G. Marvin.
Time-dependent behavior of a reattaching shear layer.
*AIAA journal*, 25(7):914–919, 1987.

[3] P. M. Ligrani, J. L. Harrison, G. I. Mahmmod, and M. L. Hill.
Flow structure due to dimple depressions on a channel surface.
*Physics of Fluids*, 13(11):3442–3451, 2001.

[4] T. Wang, M. Lin, and R.S. Bunker.
Flow and heat transfer of confined impingement jets cooling using a 3-d transient liquid crystal scheme.
*International Journal of Heat and Mass Transfer*, 48(23-24):4887–4903, 2005.

[5] J. C. Han and S. Ekkad.
Recent development in turbine blade film cooling.
*International Journal of Rotating Machinery*, 7(1):21–40, 2001.

[6] C.G. Speziale.
Numerical study of viscous flow in rotating rectangular ducts.
*Journal of Fluid Mechanics*, 122:251–271, 1982.

[7] K.C. Cheng, Ran-Chau Lin, and Jenn-Wuu Ou.
Fully developed laminar flow in curved rectangular channels.
*Journal of Fluids Engineering, Transactions of the ASME*, 98 Ser 1(1):41–48, 1976.

[8] J.P. Johnston.
Effects of system rotation on turbulence structure: A review relevant to turbomachinery flows.
*International Journal of Rotating Machinery*, 4(2):97–112, 1998.

cited By 29.

[9] F. Coletti, T. Maurer, T. Arts, and A. Di Sante.
Flow field investigation in rotating rib-roughened channel by means of particle image velocimetry.
*Experiments in Fluids*, 52(4):1043–1061, 2012.

[10] F. Coletti, D.L. Jacono, I. Cresci, and T. Arts.
Turbulent flow in rib-roughened channel under the effect of coriolis and rotational buoyancy forces.
*Physics of Fluids*, 26(4), 2014.

[11] S.-C. Huang and Y.-H. Liu.
High rotation number effect on heat transfer in a leading edge cooling channel of gas turbine blades with three channel orientations.
*Journal of Thermal Science and Engineering Applications*, 5(4), 2013.

[12] Y.-H. Liu, M. Huh, D.-H. Rhee, J.-C. Han, and H.-K. Moon.
Heat transfer in leading edge, triangular shaped cooling channels with angled ribs under high rotation numbers.
*Journal of Turbomachinery*, 131(4):1–12, 2009.

[13] M. Pascotto, A. Armellini, C. Mucignat, and L. Casarsa.
Coriolis effects on the flow field inside a rotating triangular channel for leading edge cooling.
*Journal of Turbomachinery*, 136(3), 2014.

[14] A. Armellini, L. Casarsa, and C. Mucignat.
Flow field analysis inside a gas turbine trailing edge cooling channel under static and rotating conditions.
*International Journal of Heat and Fluid Flow*, 32(6):1147–1159, 2011.

[15] H. Iacovides, D. Kounadis, B.E. Launder, J. Li, and Z. Xu.
Experimental study of the flow and thermal development of a row cooling jets impinging on a rotating concave surface.
*Journal of Turbomachinery*, 127(1):222–229, 2005.

[16] L. Yang, R. Kan, J. Ren, and H. Jiang.
Effect of film cooling arrangement on impingement heat transfer on turbine blade leading edge.
In *Proceedings of the ASME Turbo Expo*, volume 3, 2013.

[17] K. Elebiary and M.E. Taslim.

Experimental/numerical crossover jet impingement in an airfoil leading-edge cooling channel.
*Journal of Turbomachinery*, 135(1), 2013.

[18] L. Andrei, C. Carcasci, R. Da Soghe, B. Facchini, F. Maiuolo, L. Tarchi, and S. Zecchi.
Heat transfer measurements in a leading edge geometry with racetrack holes and film cooling extraction.
*Journal of Turbomachinery*, 135(3), 2013.

[19] C.E. Willert and M. Gharib.
Digital particle image velocimetry.
*Experiments in Fluids*, 10(4):181–193, 1991.

[20] R.D. Keane and R.J. Adrian.
Optimization of particle image velocimeters. i. double pulsed systems.
*Measurement Science and Technology*, 1(11):1202–1215, 1990.

[21] S.T. Wereley and C.D. Meinhart.
Second-order accurate particle image velocimetry.
*Experiments in Fluids*, 31(3):258–268, 2001.

[22] J. Westerweel, D. Dabiri, and M. Gharib.
The effect of a discrete window offset on the accuracy of cross-correlation analysis of digital piv recordings.
*Experiments in Fluids*, 23(1):20–28, 1997.

[23] D.P. Hart.
Super-resolution piv by recursive local-correlation.
*Journal of Visualization*, 3(2):187–194, 2000.

[24] C. Willert.
Stereoscopic digital particle image velocimetry for application in wind tunnel flows.
*Measurement Science and Technology*, 8(12):1465–1479, 1997.

[25] F. Scarano.
Interative image deformation methods in piv.
*Measurement Science and Technology*, 13(1):R1–R19, 2002.

[26] S.M. Soloff, R.J. Adrian, and Z.-C. Liu.
Distortion compensation for generalized stereoscopic particle image velocimetry.
*Measurement Science and Technology*, 8(12):1441–1454, 1997.

[27] N.J. Lawson and J. Wu.

Three-dimensional particle image velocimetry: Error analysis of stereoscopic techniques.
*Measurement Science and Technology*, 8(8):894–900, 1997.

[28] S.M. Soloff, Adrian R.J., and Liu Z.C.
Distortion compensation for generalized stereoscopic particle image velocimetry.
*Measurement Science and Technology*, 8:1441–1454, 1997.

[29] T. Astarita and Giordano R.
Spatial resolution of the stereo piv technique.
*Experiments in Fluids*, 2008.

[30] Scarano F., David L., Bsibsi M., and Calluaud D.
S-piv comparative assessment: image dewarping+misalignment correction and pinhole+geometric back projection.
*Experiments in Fluids*, 2(39):257–266, 2005.

[31] Wieneke B.
Stereo-piv using self-calibration on particle images.
*Experiments in Fluids*, 2(39):267–280, 2005.

[32] Claudio Mucignat.
*Performance evaluation of turbine trailing edge cooling channels under static and rotating conditions*.
PhD thesis, Università degli Studi di Udine, 2012.

[33] A. Armellini, C. Mucignat, L. Casarsa, and P. Giannattasio.
Flow field investigations in rotating facilities by means of stationary piv systems.
*Measurement Science and Technology*, 23(2), 2012.

[34] J. Westerweel.
Theoretical analysis of the measurement precision in particle image velocimetry.
*Experiments in Fluids*, 29(SUPPL. 1):S3–S12, 2000.

[35] Rau G., Moeller D., Cakan M., and T Arts.
The effect of periodic ribs on the local aerodynamic and heat transfer performance of a straight cooling channel.
*Journal of Turbomachinery*, pages 368–375, 1998.

[36] K. Elebiary and M.E. Taslim.
Experimental/numerical crossover jet impingement in an airfoil leading-edge cooling channel.
*Journal of Turbomachinery*, 135(1), 2013.

[37] J.P. Johnston, R.M. Halleent, and D.K. Lezius.
Effects of spanwise rotation on the structure of two-dimensional fully developed turbulent channel flow.
*Journal of Fluid Mechanics*, 56(3):533–557, 1972.

[38] A. Armellini, L. Casarsa, and P. Giannattasio.
Separated flow structures around a cylindrical obstacle in a narrow channel.
*Experimental Thermal and Fluid Science*, 33(4):604–619, 2009.